ABSTRACT

CHAVAN, GOVIND SAHADEO. Dynamic Control of FACTS devices to enable large scale penetration of Renewable Energy Resources. (Under the direction of Dr. Subhashish Bhattacharya.)

This thesis focuses on some of the problems caused by large scale penetration of Renewable Energy Resources within EHV transmission networks, and investigates some approaches in resolving these problems. In chapter 4, a reduced-order model of the 500 kV WECC transmission system is developed by estimating its key parameters from phasor measurement unit (PMU) data. The model was then implemented in RTDS and was investigated for its accuracy with respect to the PMU data. Finally it was tested for observing the effects of various contingencies like transmission line loss, generation loss and large scale penetration of wind farms on EHV transmission systems.

Chapter 5 introduces Static Series Synchronous Compensators (SSSC) which are series-connected converters that can control real power flow along a transmission line. A new application of SSSCs in mitigating Ferranti effect on unloaded transmission lines was demonstrated on PSCAD. A new control scheme for SSSCs based on the Cascaded H-bridge (CHB) converter configuration was proposed and was demonstrated using PSCAD and RTDS. A new centralized controller was developed for the distributed SSSCs based on some of the concepts used in the CHB-based SSSC. The controller's efficacy was demonstrated using RTDS.

Finally chapter 6 introduces the problem of power oscillations induced by renewable sources in a transmission network. A power oscillation damping (POD) controller is designed using distributed SSSCs in NYPA's 345 kV three-bus AC system and its efficacy is demonstrated in PSCAD. A similar POD controller is then designed for the CHB-based SSSC in the IEEE 14 bus system in PSCAD. Both controllers were noted to have significantly damped power oscillations in the transmission networks.

Dynamic Control of FACTS devices to enable large scale penetration of Renewable Energy Resources

by
Govind Sahadeo Chavan

A dissertation submitted to the Graduate Faculty of
North Carolina State University
in partial fulfillment of the
requirements for the Degree of
Doctor of Philosophy

Electrical Engineering

Raleigh, North Carolina

2017

APPROVED BY:

Dr. Mesut Baran	Dr. Aranya Chakrabortty
Dr. Gregory Buckner	Dr. Subhashish Bhattacharya Chair of Advisory Committee

DEDICATION

To my parents

Sangita Chavan & Sahadeo Chavan

BIOGRAPHY

The author was born in Mumbai, India on December 5, 1986. He received his Bachelors degree in 2008 from V.J.T.I., an autonomous institute under the University of Mumbai, India. He received his Master of Science degree in 2013 from North Carolina State University at Raleigh, NC. He has also worked for nearly three years in a electric utility based in Mumbai, India.

The author has been pursuing his Ph.D. in Electrical Engineering at North Carolina State University since 2011. He is a researcher with the Future Renewable Electric Energy Delivery and Management (FREEDM) Systems Center sponsored by the National Science Foundation. During his PhD study, he worked for the Quanta Technology, LLC as a graduate intern. His research interests include FACTS, integration of Renewable Energy systems with the grid and utility application of power electronics towards creating a smart grid.

ACKNOWLEDGEMENTS

This work has been done at the Department of Electrical and Computer Engineering at North Carolina State University and the NSF-FREEDM Engineering Research Center.

I would like to express my sincere gratitude to my adviser, Professor Subhashish Bhattacharya for his guidance and support throughout the course of his work. His constant encouragement and advice have helped me develop as a researcher and an electrical engineer over the duration I have worked here. He has always striven to provide us with the best working environment and state-of-the-art equipment for research. I would also like to thank Dr. Aranya Chakrabortty for being a constant source of inspiration and new ideas. I quite enjoyed the technical discussions and the brainstorming sessions we had while we were working together on the SCE project. It has been a great pleasure to work at the National Science Foundation funded Future Renewable Electric Energy Delivery and Management (FREEDM) Systems Center. I would like to acknowledge the effort of all the FREEDM faculty members to create and maintain an excellent research and education environment. I would also like to thank Dr. Saman Babaei for his guidance and patience with me during his time here at NC State University and later while he has been working at New York Power Authority.

My sincere gratitude goes to all my colleagues at the FREEDM center for providing a nice and friendly atmosphere for research. I would also like to thank Sayan Acharya, Dr. Urvir Singh, Dr. Souvik Chandra, Dr. Sachin Madhusoodhanan, Dr. Samir Hazra, Dr. Arun Kadavelugu, Ritwik Chattopadhyay, Dr. Sumit Dutta, and Kasunaidu Vechalapu for their support and friendship during my Ph.D. years. A big thanks goes to Firaxis, Gaijin and Valve for the numerous sleepless nights over the course of my Ph.D.

My deepest gratitude goes to my mother, Sangita Chavan and my father, Sahadeo Chavan for their numerous sacrifices over the years. I would not have made it here without them.

TABLE OF CONTENTS

LIST OF TABLES

LIST OF FIGURES

Chapter 1

Introduction

1.1 Background

Modern electric power systems are widely interconnected, with different utilities interconnected with each other using high voltage transmission lines. A highly interconnected electrical network allows the pooling of generation resources and loads to achieve optimum power generation while reducing transmission losses [2]. Currently, the system load and generation capacity is projected to increase at a steady rate due to population growth and increased per capita consumption of electricity [3]. Further, the increased penetration of distributed renewable energy resources alters the local power flows in an unpredictable manner due to the non-deterministic power output of these energy resources. Faced with these changes, the utilities need to reinforce the power system infrastructure by increasing its capacity and making the transmission network smarter, fault tolerant and self-healing.

The transmission network has traditionally been augmented either through construction of new transmission lines, or reconductoring of existing networks. Both these techniques are quite expensive and resource intensive, and usually have a large turn-around time, with reconductoring requiring sustained outages while the maintenance work occurs. Further, both these techniques do not change the static nature of the transmission line, and any later changes

to load or generation centers could render these upgrades unnecessary, or in the worst case scenario, even inadequate.

Besides these traditional techniques, the transmission network can be augmented using the application of modern power electronic devices. Flexible AC Transmission Systems (FACTS) technology is an application of modern power electronics based devices to provide additional flexibility and control over power flow and voltage in an AC network. Broadly, the current FACTS devices can be divided into two families: Variable Impedance type devices and Switching Converter type devices.

The Variable Impedance type devices use thyristors to control the inductance value of an inductor in a continuous manner, which is called as a Thyristor Controlled Reactor (TCR). The TCR is then used in conjunction with a Thyristor Switched Capacitor (TSC) to obtain a continuously variable reactance which can be connected in series or parallel within a network [4]. Examples of this family of devices include

- Static VAR Compensator (SVC)

- Thyristor-Controlled Series Capacitor (TCSC)

- Thyristor-Controlled Phase Angle Regulator (TCPAR)

Design and control of the Variable Impedance type FACTS devices is a rich and complex topic, however, the focus of this thesis is on the design, analysis and application of Switching Converter type FACTS devices. The term "FACTS devices", wherever mentioned in this thesis, would imply Switching Converter type FACTS devices, unless explicitly stated. Examples of this family include

- Static Synchronous Compensator (STATCOM)

- Static Synchronous Series Compensator (SSSC)

- Unified Power Flow Controller (UPFC)

- Interline Power Flow Controller (IPFC)

A few examples of the long list of benefits that FACTS devices offer:

- Allow the full utilization of a power network upto its thermal limit by raising the stability limit of the system

- Allow continuous control over the system voltage profile

- Reactive power support functionality to achieve voltage regulation and power system stability improvement

- Allow power flow control on a transmission line

- Provide damping for power flow oscillations and sub-synchronous resonances

1.2 Relevance

This thesis is concerned with investigating the effect of penetration of large scale renewable energy resources like photo-voltaic plants and wind farms on the high voltage transmission system and the application of FACTS devices to mitigate the problems associated with such large scale renewable energy penetrations.

Conventional sources of generation have inertia, namely, synchronous generators with large turbines coupled with the rotor shaft. This rotating mass stores kinetic energy as it rotates at synchronous speed, and it influences power flow in the transmission system during system transients. The inertia of individual generators located within an electrically connected area contribute towards the equivalent inertia of that area due to slow coherency effects, with the entire area behaving like one large generator [5]. Having a large system inertia is essential for maintaining power system stability in transmission systems [6] - [7].

The generating capacity of renewable energy resources within the U.S. electric grid is projected to increase at an annual growth rate (AGR) of 1.9% between 2013-2040, with solar-based

generation rising at 6.0% AGR and wind-based generation rising at 2.2% AGR. Further, coal-based generation is expected to decrease at 0.6% over the same time period, with the net generating capacity increasing at 0.5% AGR till 2040 [3].

From the projections it is clear that the total generating capacity in the U.S. is expected to increase slowly, while the energy portfolio changes to include more renewable energy resources in place of conventional generation like coal. However, both solar and wind based renewable energy resources are non-deterministic in nature. Further, both solar and wind have very little inertia of their own and hence do not contribute to the equivalent inertia of the system. Since renewables are touted to replace some conventional generation, it is expected that the equivalent inertia of the system will decrease in the future. As discussed before, reduction in inertia can create instabilities within the system if they are not corrected for [7].

FACTS devices can be used to simulate the effects of inertia for non-inertial renewable energy resources and also provide damping for power oscillations triggered due to abrupt variations in their power output. However, the performance of FACTS devices based on newer converter topologies, like the modular multi-level converter (MMC) and the cascaded H-bridge converter (CHB), is not fully explored in relation with their application to renewables. For example, the performance of capacitor charge balancing algorithms under these control objectives need to be evaluated.

Distributed FACTS devices are also being considered as an alternative to conventional large scale FACTS installations and currently their control is localized to the individual devices. However, the distributed nature of these devices can be fully leveraged if they are controlled in a coordinated manner from a centralized controller sitting on top of the local controls at each FACTS device. The performance of these control algorithms also needs to be evaluated. This thesis will attempt to address these pertinent issues and will provide solutions to improve them.

1.3 Key Contributions

The key contributions of this thesis so far are listed as under:

- **Identification and Predictive Analysis of a Multi-Area WECC Power System Model Using Synchrophasors**

  Published in IEEE Transactions on Smart Grid *(Chapter 4)*.

- **Application of Static Synchronous Series Compensators in mitigating Ferranti Effect**

  Power and Energy Society - General Meeting, 2016 *(Chapter 5)*.

- **A Novel Control Algorithm for a Static Synchronous Series Compensators using a Cascaded H-Bridge converter**

  Industrial Applications Society - Annual Meeting, 2016 *(Chapter 5)*

- **Damping of Power Oscillations induced by photo-voltaic plants using distributed series-connected FACTS devices**

  Accepted in Industrial Applications Society - Annual Meeting, 2017 *(Chapter 6)*

1.4 Organization

Chapter 1 provides an introduction to the thesis topic and includes a brief motivation for research in this area. Chapter 2 describes the effect of large scale penetration of renewable energy resources on high voltage transmission systems. It begins with a brief description about conventional energy sources, and contrasts it with the non-deterministic nature of renewable energy resources. Detailed wind and PV system models are given, and the control structures required to interface them to the grid are described in detail.

Chapter 3 discusses the various FACTS devices along with their control strategies. A brief description of phase shifting transformers (PST) is given, which is a competing technology to FACTS devices. SSSC, STATCOM and the UPFC are discussed in detail along with their major control algorithms for achieving various control objectives. Two major types of control are discussed: Angle control, and Vector control.

Chapter 4 intends to develop a reduced-order equivalent model of the Western Electricity Coordinating Council's (WECC) 500 kV system. This model is used as a base-case onto which the effect of large-scale penetration of renewable energy resources can be evaluated and appropriate control actions can be performed. Tests involving loss of inertia and large scale wind penetration are performed and their effects on power system stability are observed.

Chapter 5 focuses on Static Series Synchronous Compensators (SSSC). The first section discusses the application of SSSCs in mitigating Ferranti effect. The next section describes a control algorithm for SSSC based on a Cascaded H-Bridge Converter. The final section describes a centralized control scheme for distributed series-connected FACTS devices which includes DC capacitor voltage balancing capabilities.

Chapter 6 focuses on damping of power system oscillations on transmission networks. The first section discusses the Matrix Pencil algorithm that is used for estimating the oscillatory modes within the raw data. The next section uses this method to develop a power oscillation damping (POD) controller for distributed SSSCs connected in NYPA's three-bus AC system. The final section discusses the design of another POD controller for a CHB-based SSSC connected in the IEEE-14 bus system.

Chapter 7 concludes the thesis and proposes some future work which can be based off of this thesis.

Chapter 2

Renewable Energy Resources

2.1 Introduction

Power generation is generally classified into two kinds: Non-renewable and Renewable sources of generation. However, this distinction is not useful from the point of view of an electrical engineer, since there are renewable sources of generation which are deterministic, such are hydroelectric and geothermal plants as well as non-deterministic sources like photo-voltaic and wind power plants. Deterministic renewable sources electrically function quite similarly to non-renewable sources of generation and are generally lumped together as 'conventional sources' of generation. The term 'renewable sources' wherever mentioned in this thesis, would mean non-deterministic renewable energy resources like photo-voltaic and wind power plants.

2.2 Conventional power generation

Conventional sources of generation are deterministic, because they rely on stored energy which is converted to electricity using synchronous generators. This stored energy can be chemical in nature like in the case of coal and natural gas, heat as in the case of geothermal or gravitational as in the case of hydro-electric plants. This energy is used to directly drive a set of turbines, or heat a fluid which drives the turbines. The turbines are mechanically coupled with the rotor

shaft of a three-phase synchronous generator which converts the mechanical power output of the rotating turbines into three-phase electrical power.

The rotor speed of the synchronous generator is controlled using the speed-governor, which keeps the rotor speed and hence the electrical frequency of the output within a tight band above and below the nominal frequency. The rotor speed dynamics can be obtained from Newton's laws of motion as applied to rotating objects,

$$\begin{aligned} \dot{\delta}_e &= \omega_e \\ J\dot{\omega}_e &= T_m - T_e \end{aligned} \tag{2.1}$$

In equation (2.1), δ_e and ω_e represent the rotor electrical angle and electrical angular speed respectively. J is the moment of inertia of the coupled rotor and turbine system along its major axis of rotation. T_m is the mechanical torque being exerted by the turbine on the shaft and T_e is the electrical torque exerted by the air-gap magnetic flux to counter the mechanical torque. Under steady state, both these torques are equal and the rotor speed remains constant. Equation (2.1) can be rewritten as

$$\begin{aligned} J\omega_e\dot{\omega}_e &= \omega_e \left(T_m - T_e\right) \\ &= P_m - P_e \end{aligned} \tag{2.2}$$

In equation (2.2), P_m and P_e represent the turbine input mechanical power and the generator output electrical power respectively, ignoring losses. It is apparent that any transients in P_m and P_e would perturb ω_e and hence the electrical frequency of the output. The speed-governor system essentially measures the perturbations in the electrical frequency and automatically adjusts P_m through the turbine control valve. This control loop helps the synchronous generator stay in synchronism with the grid.

The output voltage of the synchronous generator is kept constant by means of an automatic voltage regulator (AVR). The generator terminal voltage is sensed using voltage transformers

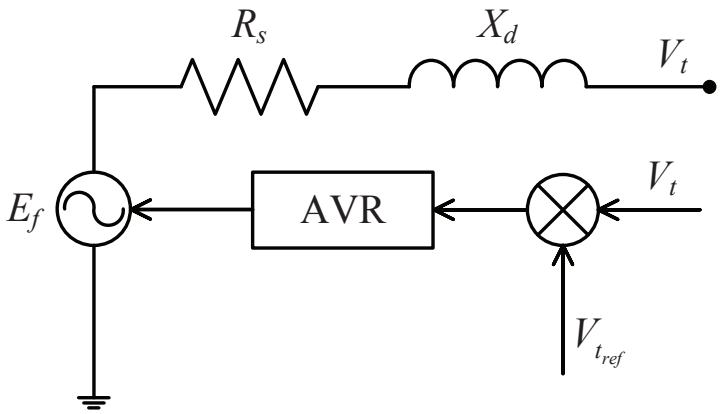

Figure 2.1: Simplified AVR control block diagram

and is compared with the terminal voltage set-point and the field voltage E_f of the synchronous generator is adjusted to control the terminal voltage. Figure 2.1 shows a simplified block diagram of the voltage regulator.

The speed-governor control and the AVR control help ensure that conventional generation is deterministic. The entire AC power system infrastructure is built on the condition that the frequency within the grid is constant and tightly controlled and all generators inside the grid rotate in synchronism with respect to each other.

2.3 Renewable resources

As opposed to conventional sources of generation, renewable energy resources are non-deterministic and cannot be controlled in the way conventional generation can be. This is because the 'prime-mover' for such resources is uncontrollable and additional control systems, namely voltage source converters (VSC) are required to properly interface these resources to the electric grid. Before moving on to describing the individual renewable resources, a detailed description of the VSC needs to be given.

2.3.1 Voltage Source Converter

The voltage source converter is an electrical device which can connect a DC system to an AC system by means of controlled switching of power electronic switches. Power electronic switches vary depending on the blocking voltage, current carrying capacity and switching frequency that the power electronic converter is designed for. The switches are classified based on their construction: Insulated Gate Bipolar Transistor (IGBT), Power Metal-Oxide-Semiconductor Field-Effect Transistor (MOSFET), Gate Turn-off Thyristor (GTO), etc. They are also classified based on the semiconductor material used: Silicon, Silicon Carbide, Gallium Nitride, etc. However for the purpose of this analysis, we assume that the appropriate switches have been selected for the converter.

The voltage source converter are available in various topologies:

- Two-level converter
- Neutral Point Clamped (NPC) converter
- Flying Capacitor (FC) Multi-level converter
- Cascaded H-Bridge (CHB) Multi-level converter
- Modular Multi-level Converter (MMC)

In this section however, the analysis will be performed on the averaged model of the converter, without paying attention to the converter topology. In subsequent chapters, certain converter topologies will be analyzed like the NPC, CHB and MMC type converters in detail.

Before the analysis is begun, a brief description of the reference frame theory is given along with the various reference frames used in this thesis.

Reference frame theory

In a balanced three-phase system, the critical variables, namely current and voltage obey the following rule:

$$f_a + f_b + f_c = 0 \tag{2.3}$$

In equation (2.3), the quantities f_a, f_b and f_c can represent either three-phase voltages and currents. From equation (2.3), it is clear that the three phase quantities can be expressed using two sinusoidal quantities alone. The third quantity can be expressed as a linear sum of the other two quantities, as seen in equation (2.4)

$$f_c = -f_a - f_b \tag{2.4}$$

The balanced three-phase quantities can thus be represented as a linear combination of two orthogonal reference quantities, thus converting the three-phase system into a two phase equivalent through a vectorial transformation of variables. This was first documented by Park [8] for analysis of AC synchronous machines and Lyon [9] in theory of instantaneous symmetrical components. In case the system contains unbalanced three-phase components so that equation (2.3) is not applicable, a third component is also added in the tranformation which represents the zero-sequence unbalance in those components.

The change of reference variables is linear in nature and can be represented by a linear transformation matrix as

$$\begin{bmatrix} f_\alpha \\ f_\beta \\ f_\gamma \end{bmatrix} = \frac{2}{3} \begin{bmatrix} 1 & -\frac{1}{2} & -\frac{1}{2} \\ 0 & \frac{\sqrt{3}}{2} & -\frac{\sqrt{3}}{2} \\ \frac{1}{2} & \frac{1}{2} & \frac{1}{2} \end{bmatrix} \begin{bmatrix} f_a \\ f_b \\ f_c \end{bmatrix} \tag{2.5}$$

The transformation in equation (2.5) is referred to as the Park's transformation or the $\alpha\beta\gamma$ transformation. It is represented graphically in figure 2.2. The phasor f_{abc} in figure 2.2 is rotating at an angular speed ω_e which is the line frequency in rad/s. The reference axes are

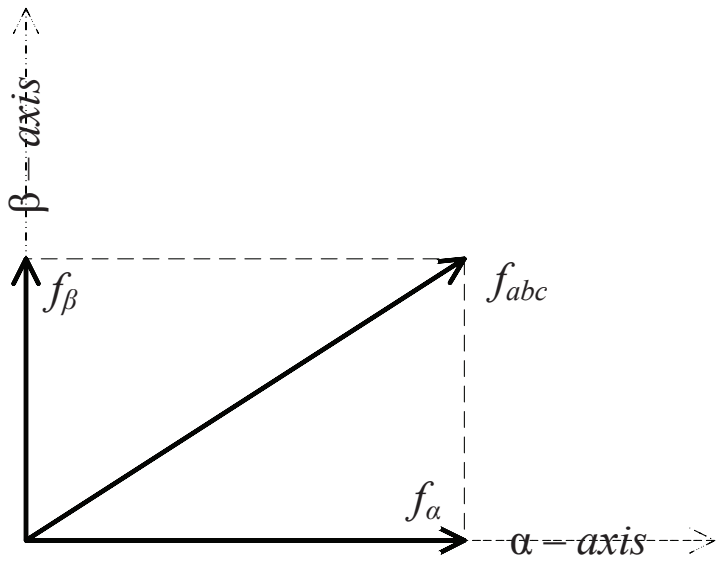

Figure 2.2: Phasor diagram showing the $\alpha\beta\gamma$ transformation

static and hence the quantities f_α and f_β are sinusoidally oscillating at ω_e rad/s. However, if the reference frame rotates at the same angular speed as f_{abc} and in the same direction, the resultant phasor projections will be at steady state as long as f_{abc} does not change its magnitude and angular speed. Such reference frames are referred to as 'synchronous rotating frames' of reference, and the linear transformation associated with them is called as the synchronous $dq0$ transformation. If $\theta = \omega_e t + \phi$, then the linear transformation can defined as

$$\begin{bmatrix} f_d \\ f_q \\ f_0 \end{bmatrix} = \frac{2}{3} \begin{bmatrix} \cos\theta & \cos\left(\theta - \frac{2\pi}{3}\right) & \cos\left(\theta + \frac{2\pi}{3}\right) \\ -\sin\theta & -\sin\left(\theta - \frac{2\pi}{3}\right) & -\sin\left(\theta + \frac{2\pi}{3}\right) \\ \frac{1}{2} & \frac{1}{2} & \frac{1}{2} \end{bmatrix} \begin{bmatrix} f_a \\ f_b \\ f_c \end{bmatrix} \tag{2.6}$$

The transformations derived in equations (2.5) and (2.6) are magnitude-conserving transformations, i.e. the peak magnitude of the variables in the transformed reference frame is identical to the peak magnitude of the same sinusoidal quantity in the *abc* reference frame. These transformations can easily be converted to the power conserving transformations by changing the proportionality constant in equations (2.5) and (2.6) from $\frac{2}{3}$ to $\sqrt{\frac{2}{3}}$.

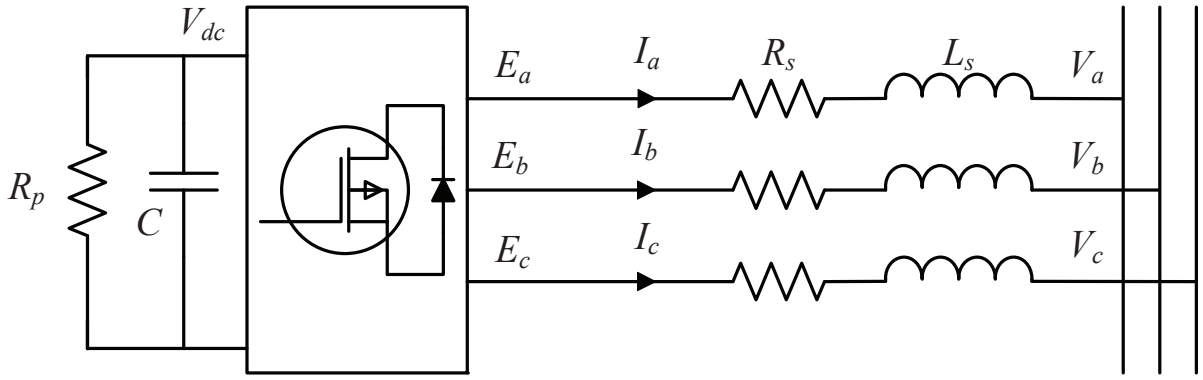

Figure 2.3: Equivalent circuit of VSC connected to the grid

VSC average model analysis

Figure 2.3 shows the equivalent model of the of a voltage source converter connected to the three-phase AC system through a series impedance [10]. In most converters, the series impedance is often designed to be the leakage reactance of a power transformer. In the *abc* reference frame, the AC-side circuit equations can be written by applying KVL:

$$L_s \frac{d}{dt} \begin{bmatrix} I_a \\ I_b \\ I_c \end{bmatrix} = \begin{bmatrix} -R_s & 0 & 0 \\ 0 & -R_s & 0 \\ 0 & 0 & -R_s \end{bmatrix} \begin{bmatrix} I_a \\ I_b \\ I_c \end{bmatrix} + \begin{bmatrix} E_a - V_a \\ E_b - V_b \\ E_c - V_c \end{bmatrix} \tag{2.7}$$

Transforming equation (2.7) into the synchronous $dq0$ frame of reference,

$$\frac{d}{dt} \begin{bmatrix} I_d \\ I_q \\ I_0 \end{bmatrix} = \begin{bmatrix} -\frac{R_s}{L_s} & \omega_e & 0 \\ -\omega_e & -\frac{R_s}{L_s} & 0 \\ 0 & 0 & -\frac{R_s}{L_s} \end{bmatrix} \begin{bmatrix} I_d \\ I_q \\ I_0 \end{bmatrix} + \frac{1}{L_s} \begin{bmatrix} E_d - V_d \\ E_q - V_q \\ E_0 - V_0 \end{bmatrix} \tag{2.8}$$

The real and reactive power equations under the rotating $dq0$ reference frame are given as

$$\begin{aligned} P &= \frac{3}{2} \left(V_d I_d + V_q I_q \right) \\ Q &= \frac{3}{2} \left(V_d I_q - V_q I_d \right) \end{aligned} \tag{2.9}$$

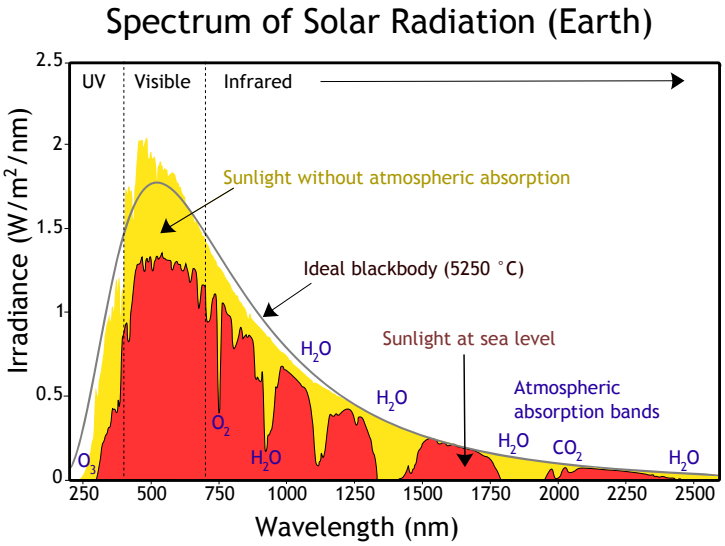

Figure 2.4: Solar radiation spectrum at top of Earth's atmosphere and at sea level. Image created by Robert A. Rohde / Global Warming Art [11].

Equation (2.8) describes the operation of the VSC in the $dq0$ frame of reference. Generally the equation for the zero-axis are omitted from analysis for the reasons discussed in section 2.3.1. Although it appears to be more complicated than equation (2.7), it must be noted that all quantities in equation (2.8) are non-sinusoidal. This provides a great advantage in controller design in terms of bandwidth and response time.

2.3.2 Photo-voltaic plants

The amount of incoming solar electromagnetic radiation per unit area that would be incident on a plane perpendicular to the rays, at a distance of one astronomical unit from the Sun is termed as the solar constant. The "solar constant" includes all types of solar radiation and its average value is measured to be 1.361 kW/m^2 using satellite observations [12]. However, this is the solar radiation arriving at the top of the Earth's atmosphere and the actual solar radiation that reaches the Earth's surface is dependent on several factors, namely the atmosphere itself, local atmospheric variations (clouds, pollution, etc.), latitude of the location, season of the year and the time of day. Further, certain bands of electromagnetic wavelengths are absorbed by oxygen,

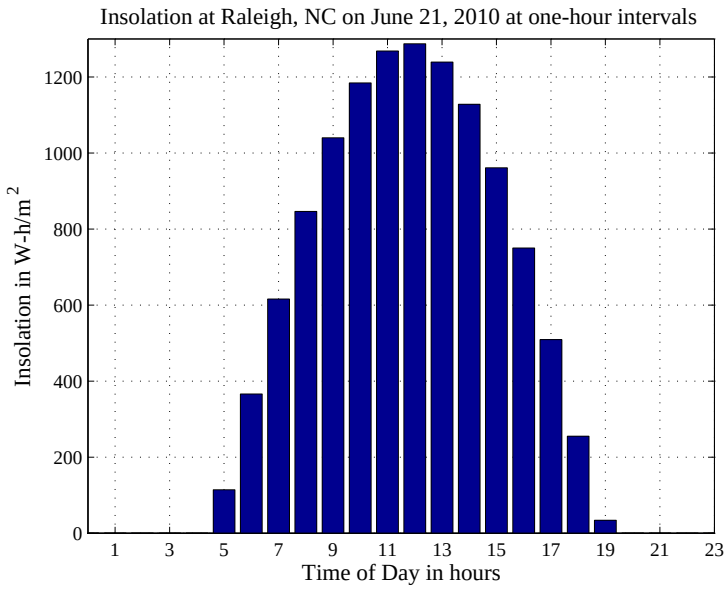

Figure 2.5: Insolation at Raleigh, NC on June 21, 2010 at one-hour intervals [13].

ozone, carbon dioxide and water vapor present in the atmosphere, and this creates troughs in the solar radiation spectrum as seen in figure 2.4. The maximum solar radiation reaching the Earth's surface on a cloudless summer day at zero zenith angle is reduced to approximately 1.0 kW/m^2. The total solar irradiance or insolation on a given day is the total energy incident on the Earth's surface at any given location on that day and is usually expressed in the units of $kWh/m^2/day$. An insolation value of 1.0 $kWh/m^2/day$ is also referred to as 'one Sun'. The solar radiation at any location varies throughout the day depending on the sun's position in the sky and the weather. Figure 2.5 shows the actual variation in insolation throughout the day on June 21, 2010 at Raleigh, NC. As can be seen clearly, the insolation rises throughout the morning with the peak occurring at noon.

Photovoltaic panels

Photovoltaic panels are composed of individual photovoltaic cells connected in series and parallel combinations. The cells generate current due to photovoltaic effect, depending on the wavelength of light that is incident upon them [14]. Figure 2.6 shows the I-V and P-V charac-

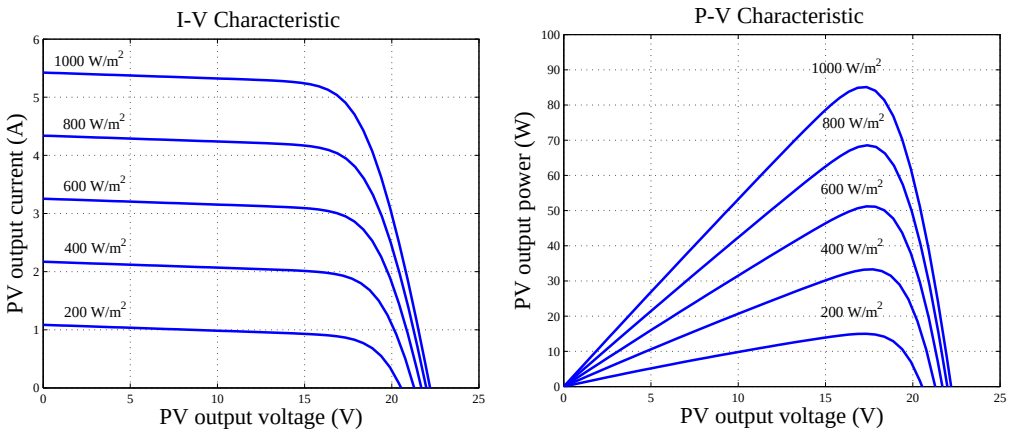

Figure 2.6: I-V and P-V characteristics of a photovoltaic panel

teristics of a photovoltaic panel with the various curves at different levels of insolation. From the P-V characteristic, it is apparent that there exist a maximum value of power for a particular value of insolation. It is economically beneficial to operate the PV panel close to this maximum value and this control objective is achieved using a Maximum Power Point Tracking (MPPT) algorithm. The following MPPT algorithms are commonly used:

- Perturb and Observe methods
- Incremental Conductance methods
- Constant Voltage method
- Short-Current Pulse method
- Open Voltage method
- Temperature methods

Two algorithms, namely 'Perturb and Observe' and 'Incremental Conductance' will be used in this thesis while performing PV related simulations. The MPPT algorithm generates a voltage command corresponding to the maximum power point at that insolation level. The voltage

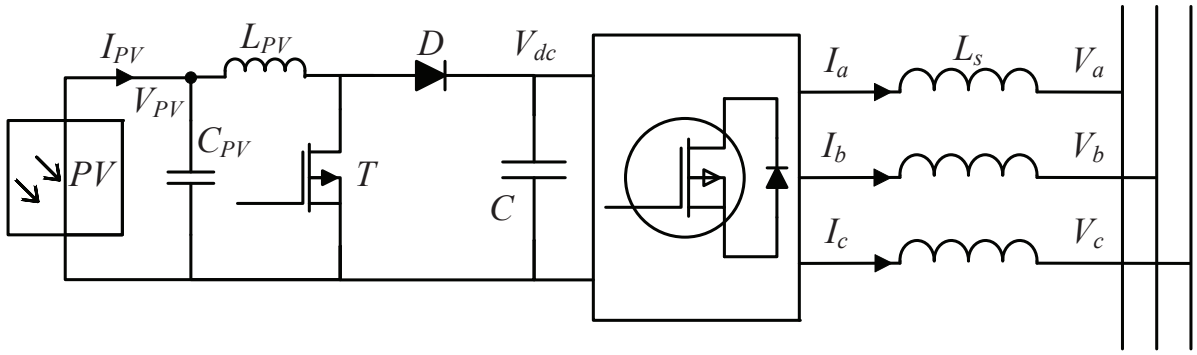

Figure 2.7: Diagram of a PV system showing the boost converter

command can be given to a DC-DC converter like a boost converter or a Dual-Active-Bridge (DAB) converter which is cascaded with a three-phase DC-AC voltage source converter. DABs are generally used in photovoltaic plants since they provide isolation between the PV side and the high voltage DC side in the form of a high frequency transformer. Boost converters are functionally identical to the DAB but they do not provide isolation. However, a boost converter has a lower device count as compared to a DAB. In this thesis, boost converters are considered for the MPPT DC-DC converter as they are functionally equivalent to a DAB.

Boost converter design

The boost converter circuit can be seen in figure 2.7. The high voltage DC side of the converter is regulated by the AC to DC converter, so the DC voltage on the three-phase converter side, V_{dc} can be considered to be constant. Thus the PV side DC voltage V_{PV} would be controlled depending on the output of the chosen MPPT algorithm. The boost converter controller is quite simplistic, where the measured value of V_{PV} is compared with V_{MPP} and the error is passed through a Proportional-Integral (PI) controller to generate the duty cycle for the transistor T. The PV system as seen in figure 2.7 was simulated in PSCAD and using switching models for the converters. The 'Incremental Conductance' algorithm was used for maximum power point operation of the photovoltaic panels. The specifications of the PV plant array are as under:

· Cells connected in series per cell string: 36

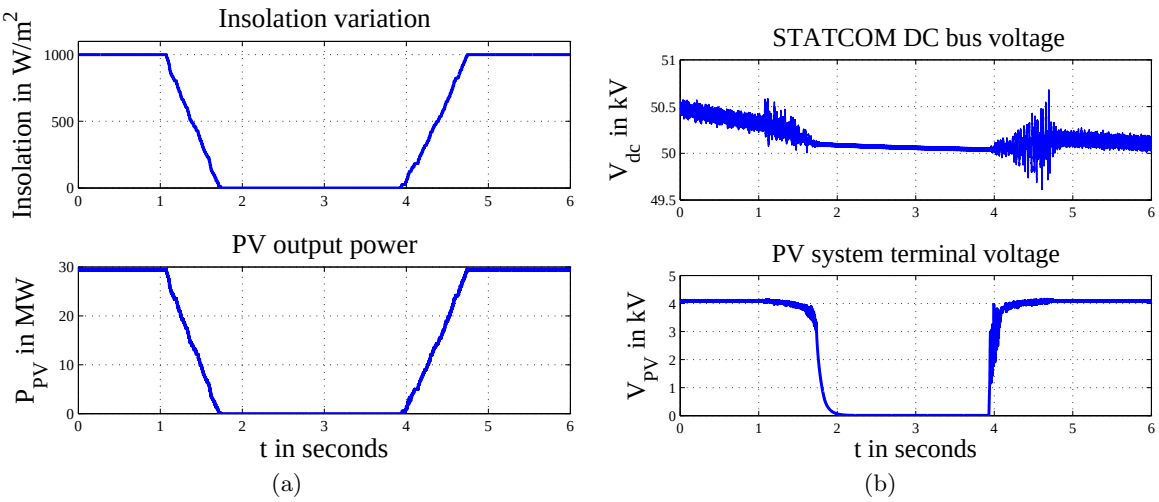

Figure 2.8: Variation of P_{PV}, V_{dc} and V_{PV} with insolation over time

- Cell strings connected in parallel per module: 3
- Modules connected in series per module string: 150
- Module strings connected in parallel per array: 1000

Figure (2.8) shows the PV output power, V_{dc} and V_{PV} as a function of insolation. The insolation variation simulates the shading of the PV panels due to large moving clouds. Although the time-scales are accelerated for the purpose of simulation, the insolation variation is analogous to what is expected from a cloud-related panel shading event. The output power P_{PV} drops almost proportionally with insolation, while the MPPT algorithm tries to find the optimum operating point which is tracked by the boost converter. It is clear from figure (2.8) that P_{PV} is highly non-deterministic and behaves more like a negative load than a conventional generator. Also, there are no inherent rotating masses or energy storage devices associated with a PV plant, and hence their increasing penetration of into the grid contributes to the reduction in stability of the grid, as discussed earlier.

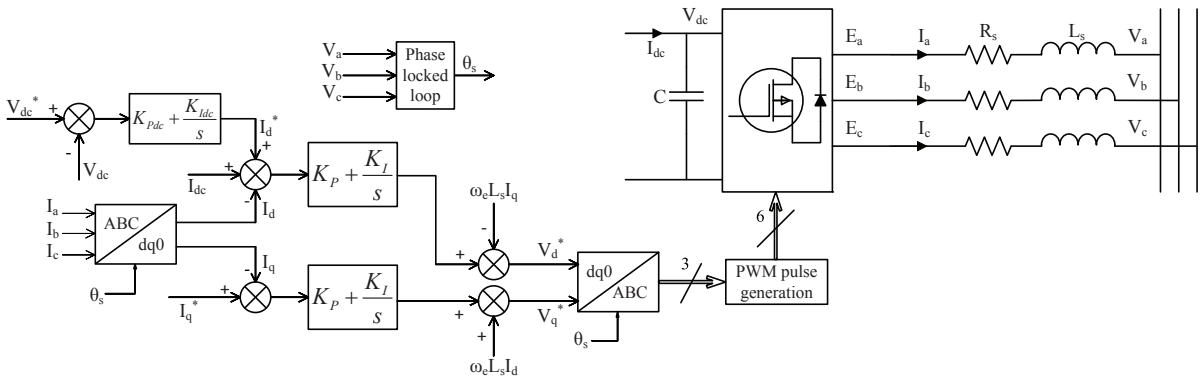

Figure 2.9: Grid side DC-to-AC converter control block diagram

Grid-side converter controls

The primary purpose of the grid side converter, as shown in figure 2.7, is to maintain the high voltage DC bus voltage constant, the secondary purpose of the controls is to utilize the remainder of the current rating of the converter to provide reactive power support. A rotating reference frame with the d-axis aligned with phase A line voltage V_a is considered which makes $V_q = 0$. This linearizes equation set (2.9) as under:

$$\begin{aligned} P &= \frac{3}{2} V_d I_d \\ Q &= \frac{3}{2} V_d I_q \end{aligned} \tag{2.10}$$

From equation set (2.10), it is apparent that real power output is directly proportional to I_d, while the reactive power output is directly proportional to I_q. This is because, in general, the magnitude of the AC side terminal voltage remains fairly constant and V_d equals the peak magnitude of the voltage sine wave in the chosen reference frame. The command I_d^* is obtained by comparing the reference DC bus voltage with the actual DC bus voltage. The DC current I_{dc} is fed-forward to improve the performance of the PI controller.

The command I_q^* is driven by the control objectives for the VSC, namely:

- Provide reactive power support

- Regulate the AC terminal voltage

- Unity power factor operation, i.e. $I_q^* = 0$.

Usually I_q^* is also limited by the current carrying capacity of the power electronic switches and is set to zero when the converter is operating at its maximum real power output rating. The VSC essentially can function like a STATCOM when the real power output is zero.

Figure 2.9 shows the control block diagram for the DC-AC converter. The current references are generated as explained in the previous paragraphs and are given to current controllers along the respective axes to generate the voltage references for the converter. The voltage references are transformed to the *abc* frame and then compared with a high frequency triangle wave to generate the pulse width modulated (PWM) pulses for the power electronic switches.

2.3.3 Wind farms

Historically, wind energy has been harnessed using windmills for pumping water and grounding grain. Wind energy was also used extensively during the 'Age of Sail' to propel ships across oceans. However, the modern wind turbine is quite different from windmills and is optimized to extract maximum energy from the blowing wind. Almost all large wind turbines have the same design with minor changes: a horizontal axis wind turbine (HAWT) having an upwind rotor with three blades. Wind farms can be located both on-shore and off-shore, each having their different advantages. Off-shore wind turbines encounter higher speed winds than on-shore turbines, as there are less obstructions off-shore. However maintenance and repair of on-shore turbines is much cheaper than off-shore turbines.

Figure 2.10 shows the schematic of a Newtonian fluid flow through a disk-shaped actuator, which represents the wind turbine. From the continuity equation, $A_1\nu_1 = A\nu = A_2\nu_2$. Since the air density ρ does not vary during this process, the mass flow rate can be written as $\dot{m} = \rho A_1\nu_1 = \rho A_2\nu_2$. Finally, the kinetic energy stored in the wind before it encounters the turbine is $\frac{1}{2}m\nu_1^2$. Thus the power stored in the wind P_w before it hits the wind turbine is given

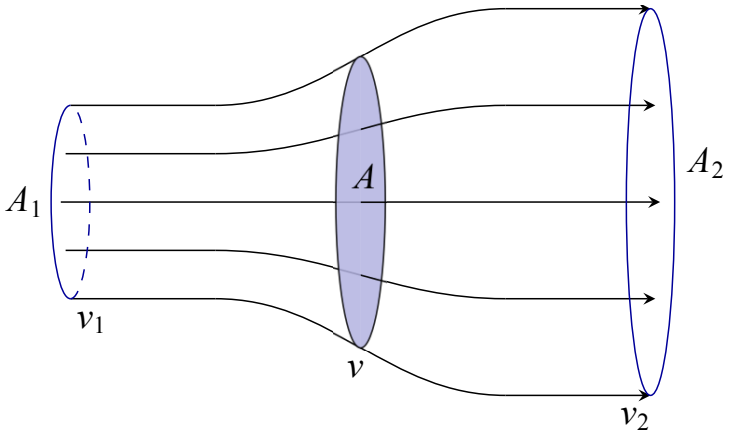

Figure 2.10: Schematic of fluid flow through a disk-shaped actuator

as [15],

$$P_w = \frac{1}{2}\rho A_1 \nu_1^3 \tag{2.11}$$

Equation (2.11) indicates that P_w is in direct proportion to the third power of the wind velocity ν_1. The wind turbine can extract only some of this power P_s, given by,

$$P_s = \frac{1}{2}C_p \rho \pi R^2 \nu_1^3 \tag{2.12}$$

In equation (2.12), R is the radius of the circle swept by the wind turbine, and C_p is the power coefficient that expresses the effectiveness of the wind turbine in transforming the wind's kinetic energy into mechanical energy. C_p is a function of the 'tip-speed' ratio $\lambda = \frac{\omega R}{\nu_1}$, where ω is the angular velocity of the turbine blades. The theoretical upper bound on C_p is given by Betz's law, $C_{p_{max}} = \frac{16}{27} \approx 0.593$. Most large wind turbines achieve a peak C_p in the range of 0.45 to 0.50.

From equation (2.12), it is clear that the shaft power available varies significantly depending on the wind speed, and at certain low speeds, the shaft power available is not enough to cover even the maintenance caused due to wear and tear of gears and bearings. Hence, wind turbines have a cut-off speed below which they are not operated. Also since P_s varies with the cube

of wind speed, the shaft power increases quite rapidly with increasing wind speeds. In such situations, it becomes difficult to keep λ and hence C_p constant without damaging the turbine itself. Thus, at high wind speeds, the turbine reduces C_p by rotating its blades in order to maintain an constant power output while protecting the turbine itself. At even higher wind speeds, the turbine is locked to prevent it from getting damaged.

Electrical generators

The previous section explained the mechanical aspects of the wind turbine and explains how the wind energy is transformed into the mechanical energy on the shaft. The shaft mechanical power is converted to electrical power by means of a electrical generator. Typically, two types of electrical machines are used,

- Doubly Fed Induction Generator (DFIG)

- Permanent Magnet Synchronous Generator (PMSG)

The DFIG is essentially a 3-φ induction machine with a wound rotor, and is similar to the wound rotor induction motor (WRIM) in construction. However, WRIMs have their rotor windings connected to an external resistor bank which are used for motor speed control. The rotor side connections on a DFIG are connected to a 3-φ VSC which is connected in a back-to-back configuration to another 3-φ VSC. The second VSC is connected to the grid on the AC side, and is often referred to as the 'grid-side converter'. The VSC connected on the rotor side is termed as the 'rotor-side converter'. The rotor-side converter is responsible for controlling the electrical torque of the machine while the grid-side converter holds the DC bus voltage and the grid side voltage at pre-determined constant values. This configuration is usually referred to as the 'Type - 3' configuration of wind turbines, as shown in figure 2.11. This configuration is quite popular because the converters do not carry the full power output of the wind turbine, and they can be designed with a lower rating which corresponds to a fraction of the actual rating of the turbine.

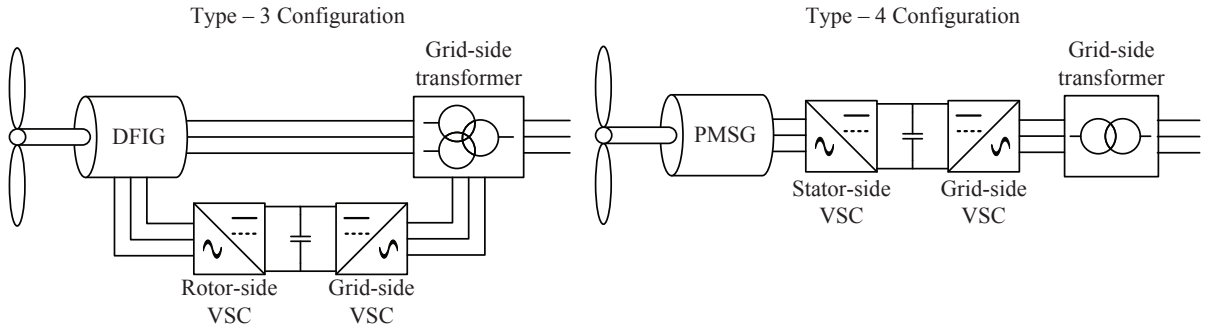

Figure 2.11: Schematic drawings of type - 3 and type - 4 wind turbine configurations

The PMSG is a 3-φ synchronous machine with a permanent magnet as a rotor. The rotor magnet is usually a rare earth magnet made from an alloy of neodymium, iron and boron, referred to as a 'NdFeB' or neodymium magnet. The rotor has no external connections and the stator side is directly connected to a 3-φ VSC which is again connected back-to-back to another 3-φ VSC directly connected to the grid. The first VSC, also referred to as the 'stator-side converter' controls the PMSG electrical torque for MPPT operation. The 'grid-side converter' holds the DC bus voltage and the grid side voltage at pre-determined constant values. This configuration is usually referred to as the 'Type - 4' configuration of wind turbines or the full converter design, as shown in figure 2.11. This is because the converters in this design are required to carry the full power output of the wind turbine and need to be rated appropriately. Although this increases the cost of the converter, it must be noted that this configuration does not have any rotor side connections which require brushes and slip-rings for an continuous electrical connection. This leads to reduced maintenance costs.

Type - 3 wind turbines

To understand the control and operation of a type - 3 wind turbine, a description of the electrical model of the DFIG is required [16, 17, 18]. The stator circuit equations for the DFIG can be

written in the arbitrary synchronously rotating frame of reference as

$$\begin{aligned}
\lambda_{ds} &= L_s I_{ds} + L_m I_{dr} \\
\lambda_{qs} &= L_s I_{qs} + L_m I_{qr} \\
V_{qs} &= R_s I_{qs} + \mathrm{p}\lambda_{qs} + \omega_e \lambda_{ds} \\
V_{ds} &= R_s I_{ds} + \mathrm{p}\lambda_{ds} - \omega_e \lambda_{qs}
\end{aligned} \tag{2.13}$$

where V_{qs} and V_{ds}, I_{qs} and I_{ds}, λ_{qs} and λ_{ds} are the d- and q-components of the stator voltage, stator current and stator flux, respectively. R_s and L_m are the stator resistance and magnetizing inductance, respectively. $L_s = L_{ls} + L_m$, where L_{ls} is the stator leakage inductance. ω_e is the stator electrical frequency in rad/s. The operator p symbolizes the time derivative $\frac{d}{dt}$. Similarly, the rotor circuit equations can be written as

$$\begin{aligned}
\lambda_{dr} &= L_r I_{dr} + L_m i_{ds} \\
\lambda_{qr} &= L_r I_{qr} + L_m i_{qs} \\
V_{qr} &= R_r I_{qr} + \mathrm{p}\lambda_{qr} + (\omega_e - \omega_r)\, \lambda_{dr} \\
V_{dr} &= R_r I_{dr} + \mathrm{p}\lambda_{dr} - (\omega_e - \omega_r)\, \lambda_{qr}
\end{aligned} \tag{2.14}$$

where V_{qr} and V_{dr}, I_{qr} and I_{dr}, λ_{qr} and λ_{dr} are the d- and q-components of the rotor voltage, rotor current and rotor flux, respectively. R_r is the stator resistance, while $L_r = L_{lr} + L_m$, where L_{lr} is the rotor leakage inductance. ω_r is the rotor angular velocity in rad/s.

The control can be simplified with the proper choice of the reference frame. For wind turbine control, the stator flux reference frame is often chosen since it makes the control simpler for the rotor side converter. Thus, we align the rotating reference frame with the d-axis stator flux,

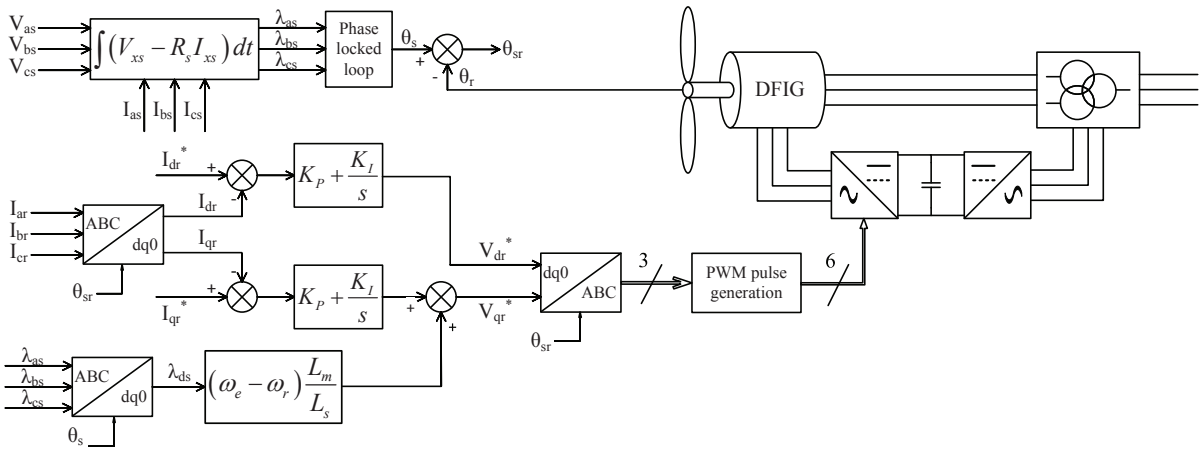

Figure 2.12: Control block diagram of type - 3 wind turbine

making $\lambda_{qs} = 0$. Equation (2.13) reduces to

$$\begin{aligned} \lambda_{ds} &= L_s I_{ds} + L_m I_{dr} \\ I_{qs} &= -\frac{L_m}{L_s} I_{qr} \\ V_{qs} &= R_s I_{qs} + \omega_e \lambda_{ds} \\ V_{ds} &= R_s I_{ds} + \mathrm{p}\lambda_{ds} \end{aligned} \tag{2.15}$$

Equation (2.15) can be combined with equation (2.14) as under,

$$\begin{aligned} \sigma &= 1 - \frac{L_m^2}{L_s L_r} \\ \lambda_{dr} &= \frac{L_m}{L_s}\lambda_{ds} + \sigma L_r I_{dr} \\ \lambda_{qr} &= \sigma L_r I_{qr} \\ V_{qr} &= R_r I_{qr} + \sigma L_r \mathrm{p} I_{qr} + (\omega_e - \omega_r)\left(\frac{L_m}{L_s}\lambda_{ds} + \sigma L_r I_{dr}\right) \\ V_{dr} &= R_r I_{dr} + \sigma L_r \mathrm{p} I_{dr} + \frac{L_m}{L_s}\mathrm{p}\lambda_{ds} - (\omega_e - \omega_r)\,\sigma L_r I_{qr} \end{aligned} \tag{2.16}$$

It must be noted that since the reference frame selected is aligned with λ_{ds}, under normal circumstances $\mathrm{p}\lambda_{ds} = 0$, except during transients. Thus that term can be ignored during

control design. From equation (2.15), it is clear that if the series resistive voltage drop is small, $V_{ds} \approx 0$. Hence, it is also common to use a stator voltage reference frame aligned with V_{qs}. However, for the purpose of this analysis, the stator flux reference frame will be used.

The cross-coupling terms in equation (2.16) are an order of magnitude smaller than the back EMF term, and their influence can be eliminated by a PI controller along each axis [17]. However, the term $(\omega_e - \omega_r)\left(\frac{L_m}{L_s}\lambda_{ds}\right)$ is large and needs to be compensated using a feed-forward term based on the estimates of d-axis stator flux. Current control can be used to generate the corresponding voltage reference values as shown in figure 2.12. The current references I_{qr}^* and I_{dr}^* can be obtained in different ways depending upon the control objective. Real and reactive power references P_c^* and Q_c^* are usually used to generate the current references as under,

$$\begin{aligned} I_{qr}^* &= -\frac{2L_s P_c^*}{3L_m V_{qs}} \\ I_{dr}^* &= \frac{\lambda_{ds}}{L_m} - \frac{2L_s Q_c^*}{3L_m V_{qs}} \end{aligned} \tag{2.17}$$

Typically, the DFIG is expected to generate real power based on the output of the MPPT algorithm. The reactive power output of the DFIG can also be controlled, however, setting a non-zero reactive power output will limit the real power output of the machine. Hence it is typical to set the reactive power output of the DFIG to zero. The grid-side VSC controls are identical to the DC-AC converter used in photovoltaic systems. The d-axis current loop helps maintain the DC bus voltage at a constant value, whereas the q-axis current loop can keep the stator side voltage fixed at a constant value, or provide reactive power compensation.

A 2MW wind turbine with a DFIG was simulated in PSCAD in a type - 3 wind turbine configuration. The DFIG model in PSCAD operates in two modes: 'Speed control' and 'Torque control' modes. PSCAD recommends that the DFIG model be started in the 'Speed control' mode and then changed to 'Torque control' mode, which is the normal mode of operation for a DFIG. The DFIG is operated in the 'Speed control' mode for the first second of the simulation and the rest of the simulation is performed in the 'Torque control' mode. For the purpose of

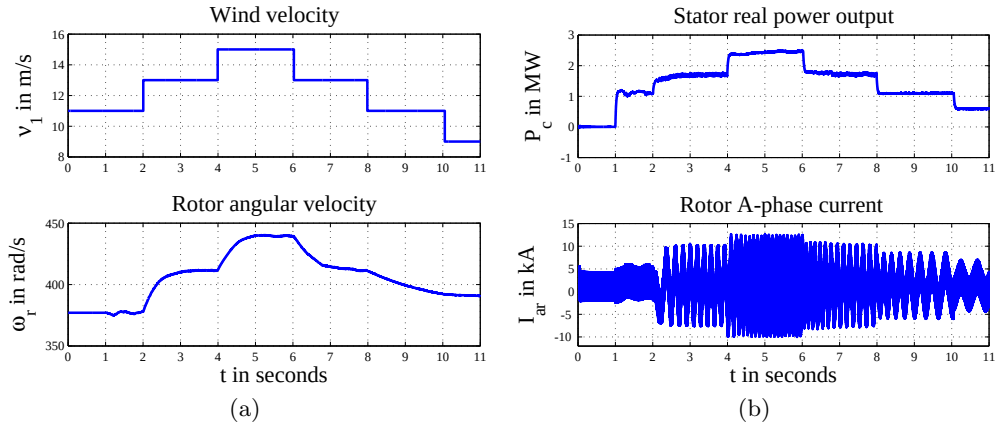

Figure 2.13: Variation of ω_r, P_c and I_{ar} with wind velocity ν_1 over time

simulation, the power coefficient C_p was set to 0.28 and the initial wind speed was considered to be 11 m/s. The wind speed was changed to 15 m/s in steps of 2 m/s every 2 seconds, and reduced back to 9 m/s in steps of 2 m/s every 2 seconds. The performance of the DFIG controller can be seen in figure 2.13 where wind velocity ν_1, rotor angular speed ω_r, stator real power P_c and rotor side A-phase current I_{ar} are plotted as a function of time.

Type - 4 wind turbines

The control and operation of type - 4 wind turbine can be understood better by giving a description of the electrical model of a PMSG. For simplicity, it is assumed that there are no damper windings on the PMSG rotor. The stator side flux and KVL equations in the synchronously rotating reference frame are written as [18, 19, 20]:

$$\begin{aligned} \lambda_{qs} &= L_q I_{qs} \\ \lambda_{ds} &= L_d I_{ds} + \lambda_f \\ V_{qs} &= R_s I_{qs} + \mathrm{p}\lambda_{qs} + \omega_e \lambda_{ds} \\ V_{ds} &= R_s I_{ds} + \mathrm{p}\lambda_{ds} - \omega_e \lambda_{qs} \end{aligned} \tag{2.18}$$

The torque equation for the PMSG is,

$$T_e = \frac{3}{2}\frac{P}{2}\left[\lambda_f + (L_d - L_q)\, I_{ds}\right] I_{qs} \tag{2.19}$$

where V_{qs} and V_{ds}, I_{qs} and I_{ds}, L_q and L_d, λ_{qs} and λ_{ds} are the d- and q-components of the stator voltage, stator current, stator inductance and stator flux, respectively. R_s and λ_f are the stator resistance and permanent magnet flux, respectively. ω_e is the stator electrical frequency in rad/s, while T_e is the electromagnetic torque. The dynamics shown in equation (2.19) can be further simplified by an appropriately chosen rotating reference frame, as in the case of the DFIG. Usually the choice of reference frame is determined by the various control strategies available [21], some of which are listed below:

- Zero d-axis Current (ZDC) control
- Maximum Torque per Ampere (MTPA) control
- Unity Power Factor (UPF) control

Each control strategy adopts a different control objective, which is indicated in the title of those strategies. For the purpose of this thesis, the ZDC control algorithm is discussed in detail. As the title states, the objective of ZDC control is to ensure that the d-axis stator current, $I_{ds} = 0$, which linearizes the torque expression from equation (2.19) to,

$$T_e = \frac{3}{2}\frac{P}{2}\lambda_f I_{qs} \tag{2.20}$$

Since λ_f remains constant, the electromagnetic torque command T_e^* is used to generate the stator q-axis current reference I_{qs}^* as

$$I_{qs}^* = \frac{4T_e^*}{3P\lambda_f} \tag{2.21}$$

The set-point $I_{ds}^* = 0$. The voltage references for the VSC can be generated using current controllers along the q- and d-axes respectively. The control block diagram for the ZDC strategy

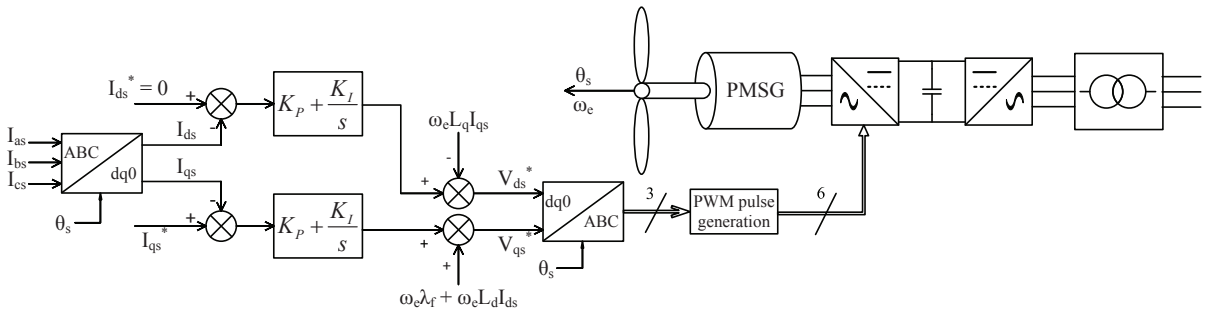

Figure 2.14: Control block diagram of type - 4 wind turbine

can be seen in figure 2.14. Usually the rotating reference frame aligned with the d-axis of the rotor, i.e. the magnetic axis of the permanent magnet, is chosen for simplifying the controls. As in the case of type - 3 wind system, the grid-side converter controls are identical to the ones used in photovoltaic systems.

2.4 Conclusion

This chapter provides an introduction to photovoltaic plants and wind farms, which are expected to penetrate the electric grid rapidly over the next 25 years. These renewable sources of energy are quite different from conventional sources of generation like coal and nuclear, in the way that their real power output cannot be changed as required by the system. These resources vary aperiodically, and are vastly dependent on the weather and the time of day. These attributes make them similar to loads, and are usually considered as negative loads in power flow calculations.

It is clear that these resources will affect the existing power networks in unique ways, some of which will be explored in the next chapter. Further, additional power electronic controllers will be required to mitigate some of the adverse effects caused by the large scale penetration of non-deterministic renewable energy resources.

Chapter 3

Review of FACTS devices

3.1 Introduction

Flexible AC Transmission Systems (FACTS) devices are AC power system controllers which utilize high speed power electronic switches controlled in a specific pattern to achieve different control objectives. FACTS devices are segregated into two types: 1. Thyristor based, and 2. Switching converter based. As discussed in chapter 1, switching converter based FACTS devices will be considered in this thesis. Voltage Source Converters (VSC) are the most common type of switching converters used in power systems and are the building blocks of FACTS devices. The most popular FACTS devices are listed under:

- Static Synchronous Compensator (STATCOM)
- Unified Power Flow Controller (UPFC)
- Static Series Synchronous Compensator (SSSC)
- Interline Power Flow Controller (IPFC)

The FACTS devices listed above have different control objectives based on their capabilities. The STATCOM and SSSC typically require one VSC, whereas UPFC and IPFC usually have two or more VSCs connected to a common DC bus. The averaged VSC model is derived

in chapter 2 which describes the averaged behavior of the VSC over several switching cycles. The averaged model of the VSC is a second-order model with cross-coupling terms as seen in equation (2.8), which is rewritten here for convenience:

$$\frac{d}{dt}\begin{bmatrix} I_d \\ I_q \\ I_0 \end{bmatrix} = \begin{bmatrix} -\frac{R_s}{L_s} & \omega_e & 0 \\ -\omega_e & -\frac{R_s}{L_s} & 0 \\ 0 & 0 & -\frac{R_s}{L_s} \end{bmatrix} \begin{bmatrix} I_d \\ I_q \\ I_0 \end{bmatrix} + \frac{1}{L_s}\begin{bmatrix} E_d - V_d \\ E_q - V_q \\ E_0 - V_0 \end{bmatrix} \tag{3.1}$$

Chapter 2 also demonstrates a generic current control strategy [10], and its control block diagram can be seen in figure 2.9. The grid-side VSC is functionally similar to a STATCOM or the shunt connected VSC in a UPFC. Current control is a basic control strategy suitable for two-level shunt connected VSCs, but multi-level VSCs have additional control loops which are responsible for their proper operation. The various multi-level VSC configurations and their controls will be discussed in subsequent sections. A brief discussion on phase-shifting transformers is also included in this chapter as it is a popular technology used in transmission systems, often as a substitute for FACTS devices.

3.2 Phase-Shifting Transformers

The sending end real and reactive power flow across a transmission line with impedance $Z_t = R_t + \mathrm{j}X_t$ is given by [22],

$$\begin{aligned} P_s &= \frac{1}{R_t^2 + X_t^2}\left(V_s^2 R_t - V_s V_r R_t \cos\delta_{sr} + V_s V_r X_t \sin\delta_{sr}\right) \\ Q_s &= \frac{1}{R_t^2 + X_t^2}\left(V_s^2 X_t - V_s V_r R_t \sin\delta_{sr} - V_s V_r X_t \cos\delta_{sr}\right) \end{aligned} \tag{3.2}$$

$V_s\angle\delta_s$ and $V_r\angle\delta_r$ are the line voltage phasors at the sending and receiving end of the transmission line, and $\delta_{sr} = \delta_s - \delta_r$. For most transmission lines, the series resistance R_t is quite small as

compared to the series inductive reactance X_t, and equation set (3.2) reduces to

$$\begin{aligned} P_s &= \frac{V_s V_r}{X_t} \sin \delta_{sr} \\ Q_s &= \frac{\left(V_s^2 - V_s V_r \cos \delta_{sr}\right)}{X_t} \end{aligned} \tag{3.3}$$

The power flow in transmission lines connected in parallel between two buses is determined by the series impedance of those lines. Specifically, with respect to equation set (3.3), $P_s \propto \frac{1}{X_t}$, i.e. the real power flow in a line is inversely proportional to the series reactance of that line. Typically, X_t is a function of transmission line length, which is not a controllable parameter. X_t also depends on the conductor dimensions and inter-conductor distances, which are also not controllable. Thus, control of power flow across transmission lines would require an external controller which would either alter X_t or $V_s \angle \delta_s$ to change the power flow.

Phase shifting transformer (PST) is a common power flow controller connected in series with the transmission line which needs regulation. The PST usually consists of one shunt connected unit and a second series connected unit. The shunt connected unit has a load tap changer (LTC) on the the secondary side which regulates the voltage to be injected in series with the transmission line. Power flow is regulated by controlling the phase angle difference δ_{sr}, which in turn is controlled by the series injected voltage. Two designs of PSTs are common in industry:

- Symmetrical PSTs
- Asymmetrical PSTs

The difference in the two designs stems from the point at which the shunt winding is connected with respect to the series winding. This difference can be seen in figure 3.1. For a symmetrical PST, the shunt winding is tapped from the center point of the series winding. As a result of this, the voltage magnitude is the same at both terminals of the series winding, and the two differ only in phase. The transformation ratio for this PST is given as $1e^{\pm \mathrm{j}\phi}$, where ϕ is the phase angle difference between the two ends of the series winding.

For an asymmetrical PST, the shunt winding is not tapped from a symmetric location on

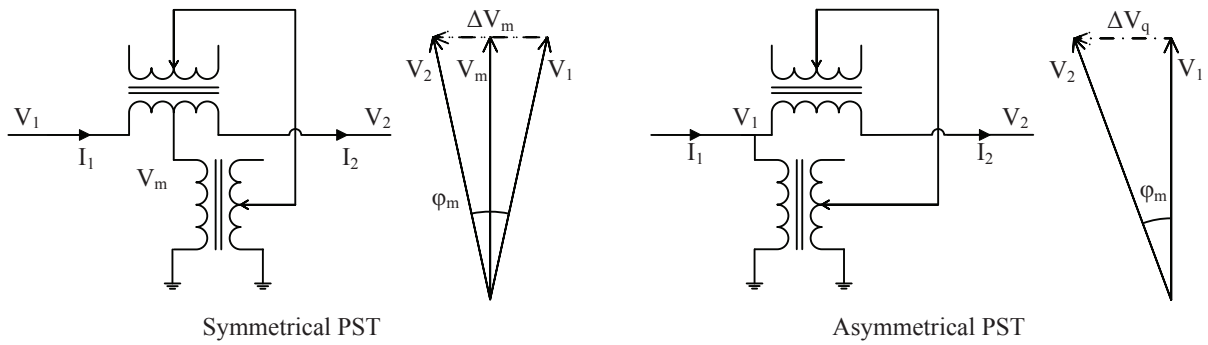

Figure 3.1: Symmetrical and asymmetrical PST circuits and phasor diagrams

the series winding, and thus the transformation ratio for this PST across the series winding terminals is given as $ae^{\pm j\phi}$, where a is a number other than 1. A special case of the asymmetrical PST is a quadrature booster, where the shunt winding is connected to the source side and the series injected voltage is at quadrature to the phase-to-neutral source side voltage. The quadrature booster mainly controls the real power flow, but since it also changes the voltage magnitude slightly, the reactive power flow is also affected slightly at the same time. Figure 3.2 shows the performance of a PST operated as a quadrature booster. The transformer tap is gradually changed from the maximum value to minimum and back, and the changes in ϕ, line real and reactive power flows P_s and Q_s, and transformer real and reactive losses P_t, Q_t are plotted.

The phase shifting transformer (PST) can control both real and reactive power in a transmission line, however it relies on mechanical tap-changers for its operation. The combination of current carrying parts while in motion leads to mechanical wear and tear of tap-changer contacts as well as degradation of transformer oil. Also, the complicated connections of the PST imply that designing the protection system for it is a considerable challenge. Further, it is also clear from the plots in figure 3.2 that the reactive power requirements of the PST are a substantial proportion of its actual rating.

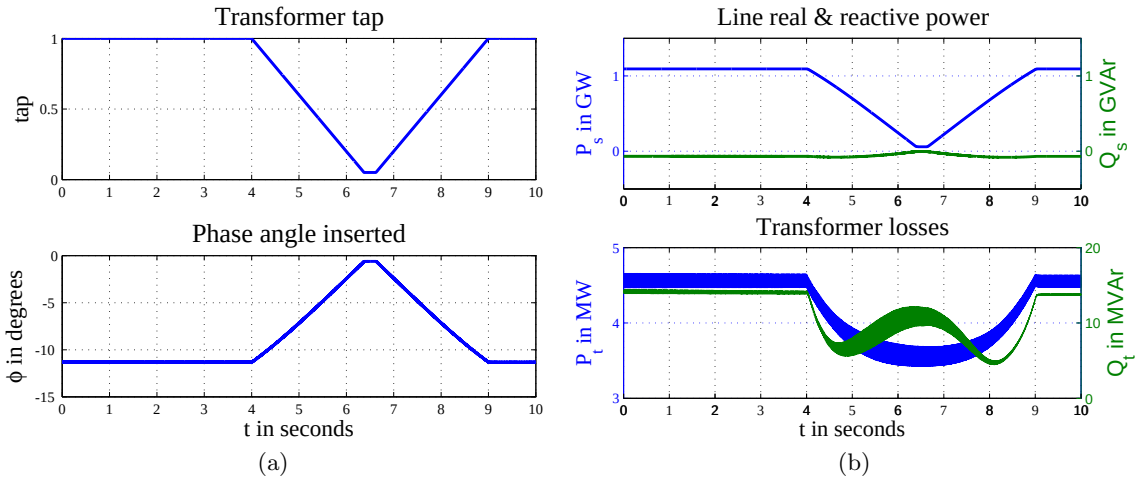

Figure 3.2: PST: Variation of ϕ, P_s, Q_s, P_t and Q_t over time

3.3 FACTS devices

This section will outline the typical control algorithms and control objectives of the STATCOM, the SSSC and the UPFC in detail. Also a brief description of multi-level converters will be given.

3.3.1 STATCOM

The STATCOM is a FACTS device which consists of a VSC connected in shunt with the bus requiring compensation. Usually, a STATCOM is connected to the bus through a step-up transformer, except in the case when the Modular Multi-level Converter (MMC) or Cascaded H-Bridge (CHB) type of VSC is used.

STATCOMs are generally used as a controllable source of reactive power in large power systems. Construction-wise, it is identical to a grid-side converter used in interfacing renewable energy resources with the 3-ϕ AC grid. However, functionally it has different control objectives. While the main function of the grid-side converter is to transform DC real power to AC real power, a STATCOM is typically used to provide reactive power support to the network. It exchanges a minimal amount of real power with the network for the purpose of keeping the DC capacitor voltage constant and recuperation of switching losses. STATCOMs can be controlled

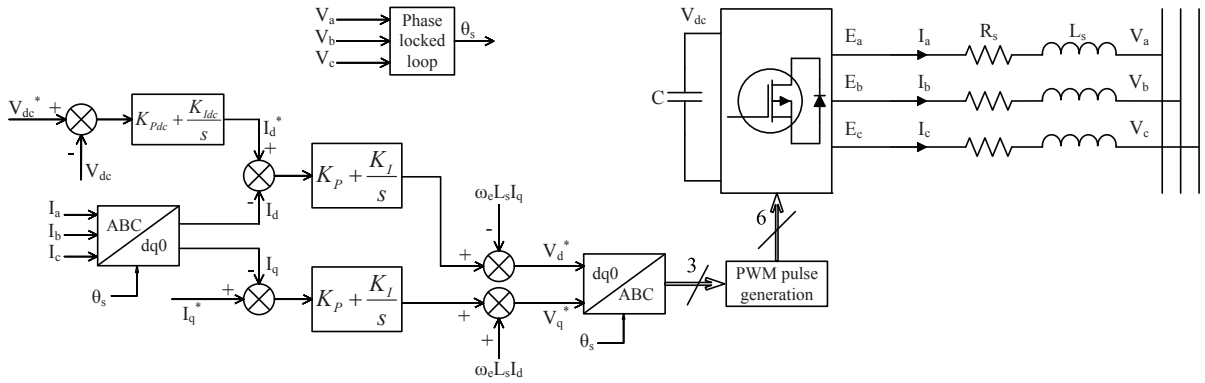

Figure 3.3: STATCOM type - I control block diagram

using two contrasting control schemes [10], which are listed below:

- **Type - I control**

  Type - I control involves controlling both d- and q- axis currents separately using their own control loops. The DC voltage is kept fixed through the d-axis control loop. This control requires PWM for proper operation.

- **Type - II control**

  Type - II control, also referred to as "angle control", involves controlling the phase angle between the AC side terminal voltage and the STATCOM output voltage. This control is suitable for line frequency switching.

Type - I control

The type - I control technique is typically used with IGBTs or MOSFETs which are suitable devices for PWM switching and is used in CHB or MMC type converters in conjunction with other capacitor charge balancing algorithms. Figure 3.3 shows the block diagram for type - I control used in STATCOMs. This control is designed around a particular choice of rotating reference frame, specifically, a rotating reference frame with its d-axis aligned with phase A line

voltage V_a, which makes $V_q = 0$. This linearizes equation (2.9) as

$$\begin{aligned} P &= \frac{3}{2} V_d I_d \\ Q &= \frac{3}{2} V_d I_q \end{aligned} \tag{3.4}$$

From equation set (3.4), it is apparent that real power output is directly proportional to I_d, while the reactive power output is directly proportional to I_q. In general, the magnitude of the AC side terminal voltage remains fairly constant and V_d equals the peak magnitude of the voltage sine wave in the chosen reference frame. The command I_d^* is obtained by comparing the reference DC bus voltage with the actual DC bus voltage. The command I_q^* is driven by the control objectives for the STATCOM, namely:

- Provide reactive power support
- Regulate the AC terminal voltage
- Unity power factor operation, i.e. $I_q^* = 0$.

When the STATCOM provide reactive power support, the q-axis current reference is calculated as $I_q^* = \dfrac{2Q^*}{3V_d}$, where Q^* is the reactive power reference. When the STATCOM operates as a voltage regulator, it exploits the coupling between reactive power and line voltage, which is common in modern power systems. A PI controller can be used to obtain I_q^* as

$$I_q^* = \left(K_{PV} + \frac{K_{IV}}{s} \right) (V_d^* - V_d) \tag{3.5}$$

The current references thus generated are given to current controllers along the respective axes to generate the voltage references for the converter. The voltage references are transformed to the *abc* frame and then compared with a high frequency triangle carrier wave to generate the pulse width modulated (PWM) pulses for the power electronic switches. Figure 3.4 shows the operation of a STATCOM connected at the far end of an unloaded long 230 kV transmission line. Initially, since the line is unloaded, the receiving end terminal voltage of the transmission

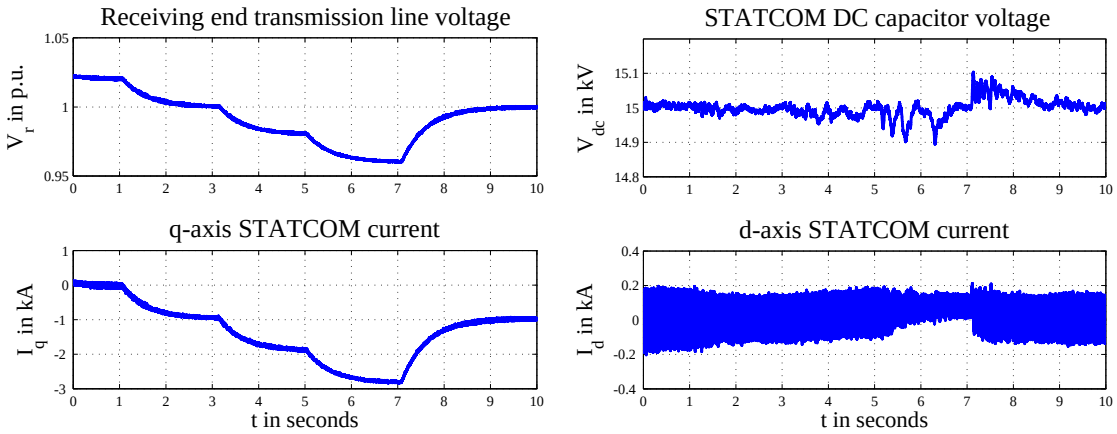

Figure 3.4: Type - I STATCOM: Variation of V_r, I_q, V_{dc} and I_d over time

line rises to about 1.02 p.u. The voltage is reduced by 0.02 p.u. every 2 seconds till the voltage reaches 0.96 p.u., starting at t = 1 second. Finally the voltage set-point is raised back to 1.0 p.u.. The transmission line receiving end voltage V_r, q- and d-axis current I_q and I_d, and DC capacitor voltage V_{dc} are plotted versus time and shows the performance of the type - I controller. As discussed before, it maintains the DC capacitor voltage constant within a tight band.

Type - II control

Type - II control is usually implemented in converters using Gate Turn-off (GTO) thyristors, which are suitable for line frequency switching. Understanding type - II control requires the inclusion of the DC capacitor voltage equations within the control algorithms. Assuming that the loss in the switches is negligible, the power balance equation can be written as

$$V_{dc} I_{dc} = \frac{3}{2} \left(E_d I_d + E_q I_q \right) \tag{3.6}$$

E_d and E_q are the d- and q-axis voltages produced at the STATCOM terminals, whereas, I_{dc} is the transient current leaving the capacitor terminals. By applying Kirchoff's current law on

the DC side, we get

$$\frac{dV_{dc}}{dt} = -\frac{1}{C}\left(I_{dc} + \frac{V_{dc}}{R_p}\right) \tag{3.7}$$

Combining equations (3.6) and (3.7), we get

$$\frac{dV_{dc}}{dt} = -\frac{1}{C}\left[\frac{3}{2V_{dc}}\left(E_d I_d + E_q I_q\right) + \frac{V_{dc}}{R_p}\right] \tag{3.8}$$

Let $k = \dfrac{\sqrt{E_d^2 + E_q^2}}{V_{dc}}$ and $\alpha = \arctan\dfrac{E_q}{E_d}$. For type - I control, both k and α are controlled separately (since both E_d and E_q can be controlled). However, for type - II control, k is fixed while α is controlled to control the STATCOM current. Hence, this control is also termed as 'angle control', where α is the angle that is controlled. Equation (3.8) can be rewritten in terms of k and α as

$$\frac{dV_{dc}}{dt} = -\frac{1}{C}\left[\frac{3}{2}kI_d\cos\alpha + \frac{3}{2}kI_q\sin\alpha + \frac{V_{dc}}{R_p}\right] \tag{3.9}$$

Since k is fixed, V_{dc} changes as the operating point of the STATCOM changes. The dynamics of V_{dc} can be incorporated into the STATCOM model by combining equation (3.8) with equation (3.1) as

$$\frac{d}{dt}\begin{bmatrix} I_d \\ I_q \\ V_{dc} \end{bmatrix} = \begin{bmatrix} -\frac{R_s}{L_s} & \omega_e & \frac{k}{L_s}\cos\alpha \\ -\omega_e & -\frac{R_s}{L_s} & \frac{k}{L_s}\sin\alpha \\ -\frac{3k}{2C}\cos\alpha & -\frac{3k}{2C}\sin\alpha & -\frac{1}{R_p C} \end{bmatrix}\begin{bmatrix} I_d \\ I_q \\ V_{dc} \end{bmatrix} - \frac{1}{L_s}\begin{bmatrix} V_d \\ 0 \\ 0 \end{bmatrix} \tag{3.10}$$

The 0-axis dynamic equation is ignored as its dynamics are not important in this analysis. Equation (3.10) is of the form $\dot{x} = \mathbf{A}x + \mathbf{B}u$, where $x = [I_d\ I_q\ V_{dc}]^\top$ and $u = [V_d\ 0\ 0]^\top$. It has the form of a linear state-space equation, however equation (3.10) is non-linear since the $\mathbf{A}$ matrix is non-linearly dependent on α. If we linearize this equation around an operating point

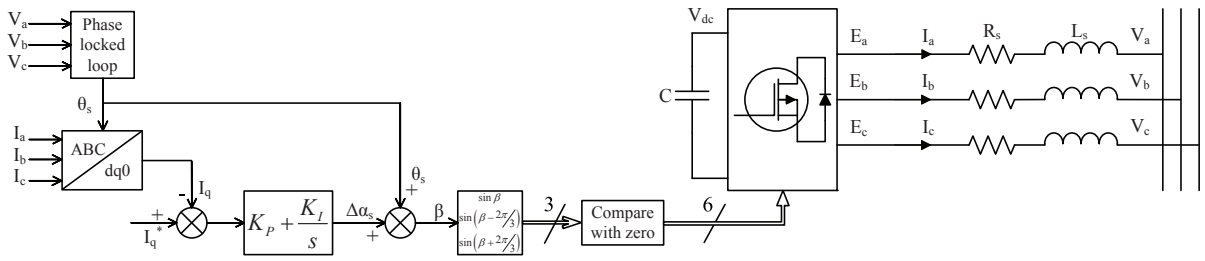

Figure 3.5: STATCOM type - II control block diagram

α_0, I_{d0}, I_{q0} and V_{dc0}, we get

$$\frac{d}{dt}\begin{bmatrix}\Delta I_d\\ \Delta I_q\\ \Delta V_{dc}\end{bmatrix} = \begin{bmatrix} -\frac{R_s}{L_s} & \omega_e & \frac{k}{L_s}\cos\alpha_0 \\ -\omega_e & -\frac{R_s}{L_s} & \frac{k}{L_s}\sin\alpha_0 \\ -\frac{3k}{2C}\cos\alpha_0 & -\frac{3k}{2C}\sin\alpha_0 & -\frac{1}{R_pC}\end{bmatrix}\begin{bmatrix}\Delta I_d\\ \Delta I_q\\ \Delta V_{dc}\end{bmatrix} + \begin{bmatrix} -\frac{1}{L_s} & -\frac{kV_{dc0}}{L_s}\sin\alpha_0 \\ 0 & \frac{kV_{dc0}}{L_s}\cos\alpha_0 \\ 0 & \frac{3k}{2C}\left(I_{d0}\sin\alpha_0 - I_{q0}\cos\alpha_0\right)\end{bmatrix}\begin{bmatrix}\Delta V_d\\ \Delta\alpha\end{bmatrix} \tag{3.11}$$

where all symbols have their usual meanings and the 0-subscript indicates the steady-state value of that said quantity. From equation (3.11), it is clear that under the small-signal assumption, a first order differential relationship exists between Δx and $[\Delta V_d\ \Delta\alpha]^\top$. The term ΔV_d acts like a disturbance term whereas $\Delta\alpha$ is the main control input. The control input can be obtained using the following control law as a function of the error in I_q,

$$\Delta\alpha = \left(K_P + \frac{K_I}{s}\right)\left(I_q^* - I_q\right) \tag{3.12}$$

The control input $\Delta\alpha$ needs to be added to the angle estimated by the phase locked loop (PLL) which is measuring the terminal voltage angle θ_s. The total angle $\beta = \theta_s + \Delta\alpha$ is used to then generate the reference carrier wave which is compared with zero to create the ON/OFF signals for the GTOs. This control can be seen in figure 3.5.

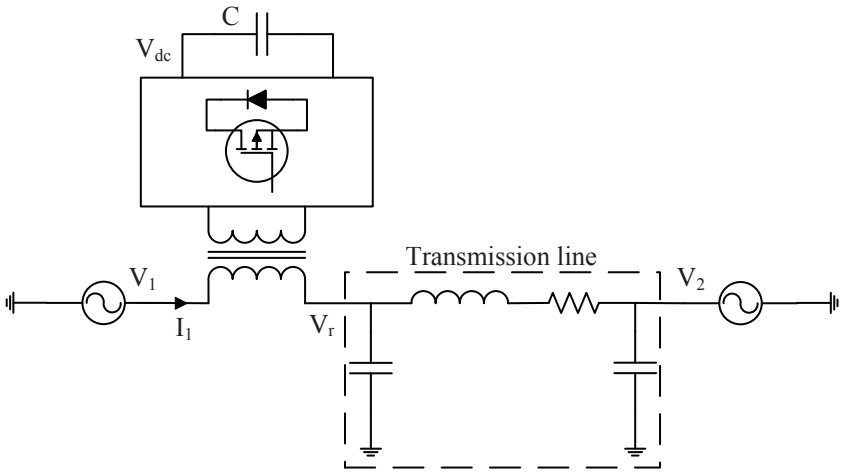

Figure 3.6: SSSC connected in a two-bus system with a transmission line

3.3.2 SSSC

The Static Series Synchronous Compensator (SSSC) is a Flexible AC Transmission Systems (FACTS) device connected in series with a transmission line in order to provide a form of controllable series compensation to the said line [23]. Figure 3.6 shows the SSSC consists of a Switching Converter, usually a Voltage Source Converter (VSC) connected to the transmission line through a series transformer. It primarily injects a controllable voltage in series with the transmission line, the voltage injected being nearly at quadrature with the line current. The phase difference is quite close to 90° since the SSSC only exchanges real power with the transmission line in order to control its DC bus voltage value and to compensate for the losses that occur in the switches in the converter [24].

Designing a SSSC is a significant challenge because, although it handles a relatively small amount of volt-amperes, it is supposed to carry the full line current reflected onto the secondary side of the series transformer, which can be a large current. The SSSC cannot be directly disconnected from the network and can only be bypassed using a circuit breaker connected in parallel to the SSSC [25]. Protection schemes for SSSC are quite complex and is one of the chief reasons preventing large scale adoption of SSSCs into the network.

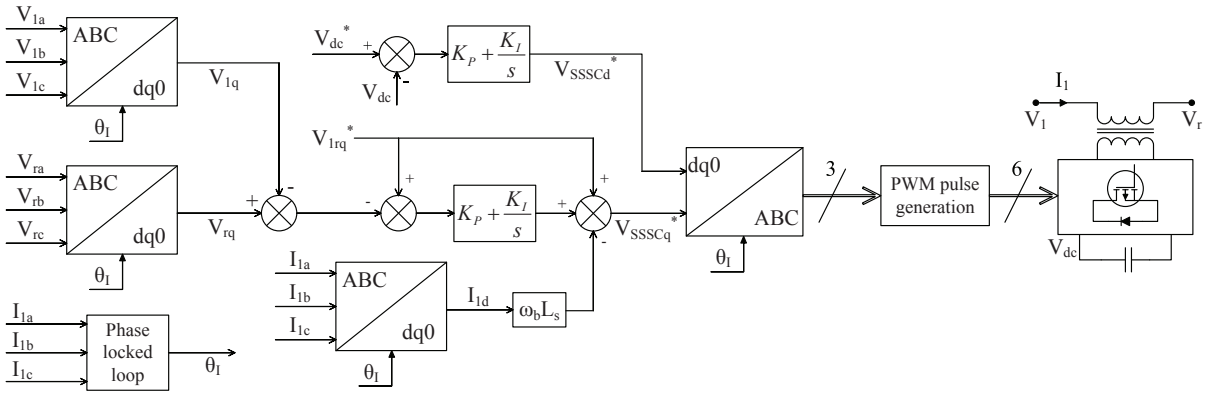

Figure 3.7: Control block diagram for a vector-controlled SSSC

The primary application of the SSSC is active power flow control over the transmission line it is connected in series with [2]. Other applications discussed in literature include the sub-synchronous resonance (SSR) mitigation [26] - [27], damping of inter-area oscillations [28] and offshore wind farm integration [29].

As in the case of STATCOMs, SSSCs can be controlled using two control techniques:

- **Vector control**
- **Angle control**

Vector Control

As in the case of STATCOM, SSSC vector control involves the control of VSC d- and q- axis voltage injections separately in their own control loops. However, the SSSC controls are quite simplified since they do not require current control for their operation.

There are several choices for aligning the d-axis of the rotating reference frame in SSSC control: Sending end phase A voltage V_{1a}, phase A transmission line current I_{1a}. Both of these choices are equally valid, however, it is common to align the d-axis of the synchronously rotating reference frame with I_{1a}. In this reference frame, the equations for real and reactive

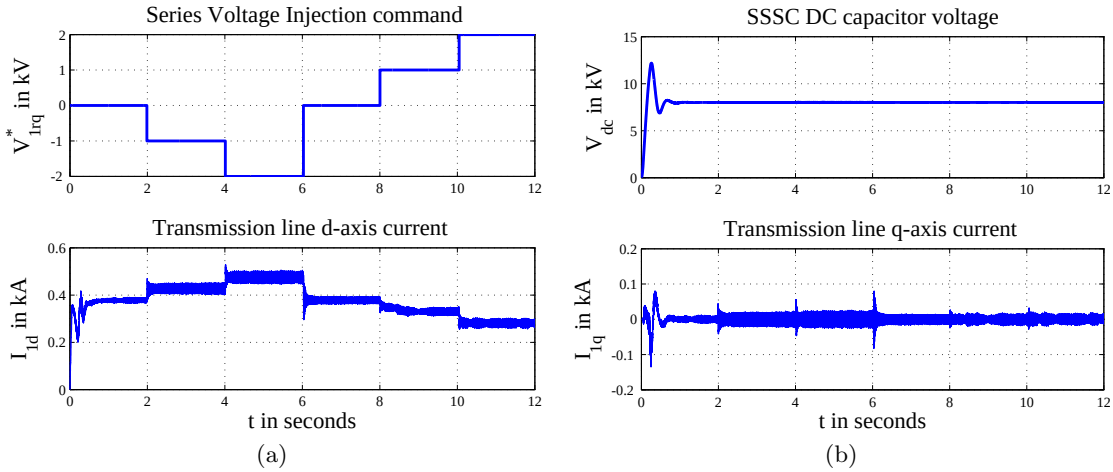

Figure 3.8: Vector controlled SSSC: Variation of V^*_{1rq}, I_{1d}, V_{dc} and I_{1q} over time

power exchanged by the SSSC get simplified as,

$$\begin{aligned} P_{SSSC} &= \frac{3}{2} V_{SSSC_d} I_{1d} \\ Q_{SSSC} &= -\frac{3}{2} V_{SSSC_q} I_{1d} \end{aligned} \tag{3.13}$$

P_{SSSC} and Q_{SSSC} are the real and reactive powers absorbed by the SSSC, V_{SSSC_d} and V_{SSSC_q} are the d- and q-axis voltages injected by the SSSC in series with the transmission line. The SSSC DC bus voltage control algorithm controls V_{SSSC_d} which maintains the DC bus voltage at the specified constant value. V_{SSSC_q} is controlled in different ways to attain different control objectives, like real power flow control or power oscillation damping.

Figure 3.7 shows the control block diagram of the SSSC which includes the DC voltage regulation loop and the line current regulation loop. The dq reference voltages can be generated for the SSSC as

$$\begin{aligned} V^*_{SSSC_d} &= \left(K_p + \frac{K_i}{s}\right)(V^*_{dc} - V_{dc}) \\ V^*_{SSSC_q} &= \left(K_p + \frac{K_i}{s}\right)\left[V^*_{1rq} - (V_{1q} - V_{rq})\right] \\ &\quad + V^*_{1rq} - \omega_b L_s I_{1d} \end{aligned} \tag{3.14}$$

The reference V^*_{1rq} is calculated depending on the control objective of the SSSC; for example,

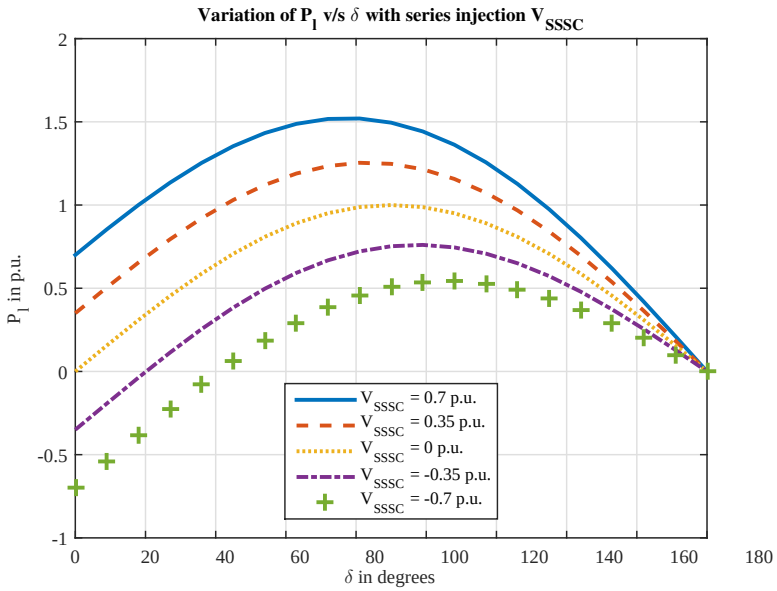

Figure 3.9: Variation of transmission line power-angle curves with changing V_{SSSC}

if the SSSC is required to insert a capacitive reactance X_q^* in series with the line, $V_{1rq}^* = I_{1d}X_q^*$ is the control input. In case of series voltage injection, the calculation is trivial. Figure 3.8 shows the operation of a SSSC where it is used to inject a controllable voltage in series with the transmission line.

SSSC's primary application is power flow control. The power flow across a transmission line is defined as $P_l = \dfrac{V_1 V_2}{X_t} \sin\delta$, where $V_1\angle\delta$ and $V_2\angle 0$ are the line voltage phasors at the sending and receiving end of the transmission line. A simplistic transmission line model is considered where the line is represented as a series inductive reactance X_t. Typically, the sending and receiving end line voltage magnitudes are maintained within tight limits and it is normal to assume that $V_1 = V_2 = V$. If the series voltage injection of the SSSC is V_{SSSC}, then the power flow across the transmission line is [2]

$$P_l = \frac{V^2}{X_t}\sin\delta + \frac{VV_{SSSC}}{X_t}\cos\frac{\delta}{2} \tag{3.15}$$

From equation (3.15), it can be seen that the SSSC increases the power flow along the transmis-

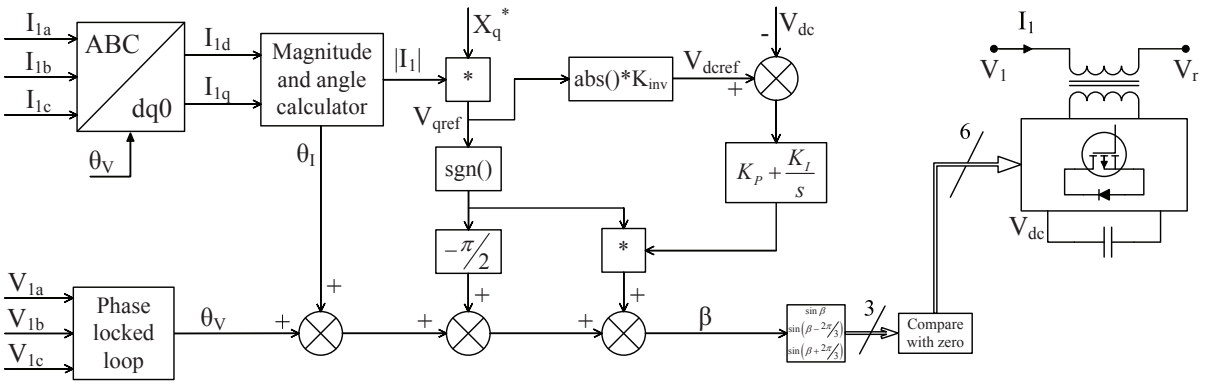

Figure 3.10: Control block diagram for a angle-controlled SSSC

sion line in an additive manner, as opposed to a TCSC which does so in a multiplicative manner. Also, the second term in equation (3.15) varies linearly with the series voltage injection V_{SSSC} and in general, insertion of V_{SSSC} affects the real power flow in a transmission line linearly. Thus control wise, the real power reference can be used to generate the command V_{1rq}^* through an appropriately designed PI controller.

$$V_{1rq}^* = \left(K_{pp} + \frac{K_{ip}}{s}\right)(P_l^* - P_l) \tag{3.16}$$

Figure 3.9 shows the variation of power angle curves for the transmission line with the changing series voltage injection. All quantities are per unitized for simplicity, with $V = 1p.u.$ and $X_t = 1p.u.$ in the plots. From figure 3.9, it can be seen that the SSSC can provide the maximum range of real power regulation when the power angle δ is less than 90°. However, this is not a matter of concern since $0 \leq \delta < 90°$ is the stable zone for real power transfer and most transmission line power angles do not exceed 45°.

Angle Control

As in the case of STATCOMs, angle control can be used to control SSSCs. The plant model of the angle controlled SSSC is identical to the one derived for type - II STATCOM in equations (3.10) and (3.11). The control block diagram for angle controlled SSSCs has been described in

detail in [2, 24, 30] and can be seen in figure 3.10. The angle β calculated by the algorithm is used to generate $3-\phi$ voltage references, which are then used to generate the switching signals for the converter.

3.3.3 UPFC

The Unified Power Flow Controller (UPFC) is a FACTs device that combines the functionality of the STATCOM and the SSSC in a single unit. The UPFC utilizes two back-to-back (BTB) connected VSCs, i.e. two converters with their DC buses connected to each other. One of the VSCs is connected in shunt with the local bus and it effectively functions like a STATCOM. The second VSC is connected in series with the transmission line connected to the same local bus, like a SSSC. However, unlike a SSSC, the series connected VSC can inject a completely controllable voltage in series with the transmission line. This means that the series VSC can inject a voltage of any magnitude at any controllable angle, and thus it can control both real and reactive power flowing across the transmission line [31, 32, 33].

The controls for the shunt-connected VSC are exactly identical to that of a STATCOM and will not be described here in detail. The primary function of this VSC is to maintain the DC bus voltage constant, however it must be noted that the DC bus voltage will be forced to change due to the voltage injection of the series-connected VSC. Thus the shunt-connected VSC will be primarily providing for the real power requested by the series-connected VSC over the DC bus. If the shunt-connected VSC still has some MVA capacity left, the VSC can provide reactive power support with its remaining MVA capacity.

The series-connected VSC functions in a similar manner to the SSSC. The SSSC, however, injects a controllable voltage in series with the transmission line, but the voltage angle is close to 90° and is not a controllable quantity. The series-connected VSC in the UPFC can inject a series voltage whose magnitude and angle can be controlled independently, allowing the UPFC to control both real and reactive power flows across a given transmission line. The control block diagram of the UPFC can be seen in figure 3.11. UPFC series converter control has been

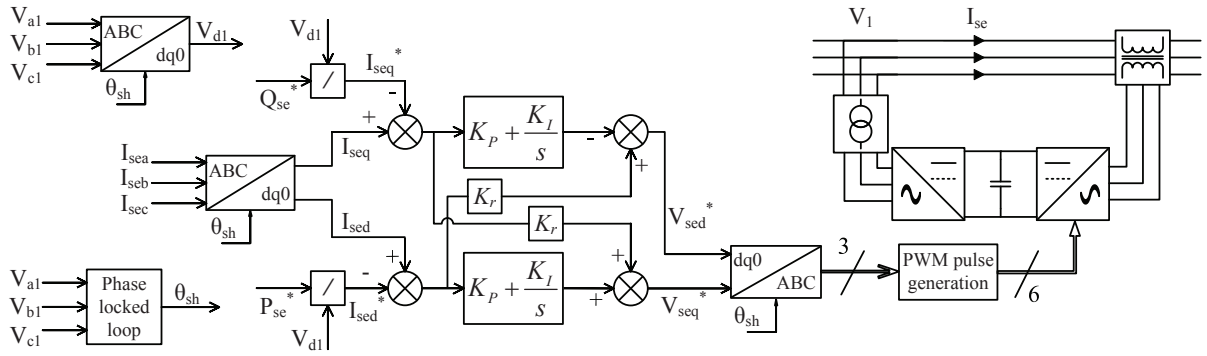

Figure 3.11: Control block diagram of a Unified Power Flow Controller

discussed extensively in literature [34, 35, 36], and the control increases in complexity as the converter construction becomes more complex.

Cross-coupling method is a rudimentary control technique, whose control law can be written as

$$\begin{bmatrix} V^*_{sed} \\ V^*_{seq} \end{bmatrix} = - \begin{bmatrix} 0 & -K_P - \frac{K_I}{s} \\ K_P + \frac{K_I}{s} & 0 \end{bmatrix} \begin{bmatrix} I^*_{sed} - I_{sed} \\ I^*_{seq} - I_{seq} \end{bmatrix} \tag{3.17}$$

K_P and K_I are the proportional and integral gains of the active and reactive power controller. The controller response can be improved upon by adding K_r to the diagonal elements in the square matrix in equation (3.17). K_r is the control gain which is used to damp power fluctuations. It is important to note that this power fluctuation is different from the "power swing" oscillations understood by the power system engineers. Power swings are low frequency oscillation ($\leq 1Hz$) related to the moments of inertia of the turbine alternator. K_r is used to damp the oscillations associated with UPFC operation in the range of 100 Hz and higher [35]. The d-q components of the series inverter voltage are then calculated as [37]

$$\begin{bmatrix} V^*_{sed} \\ V^*_{seq} \end{bmatrix} = - \begin{bmatrix} K_r & -K_P - \frac{K_I}{s} \\ K_P + \frac{K_I}{s} & K_r \end{bmatrix} \begin{bmatrix} I^*_{sed} - I_{sed} \\ I^*_{seq} - I_{seq} \end{bmatrix} \tag{3.18}$$

The damping ζ and the natural frequency of oscillation ω_n of the combined plant and control

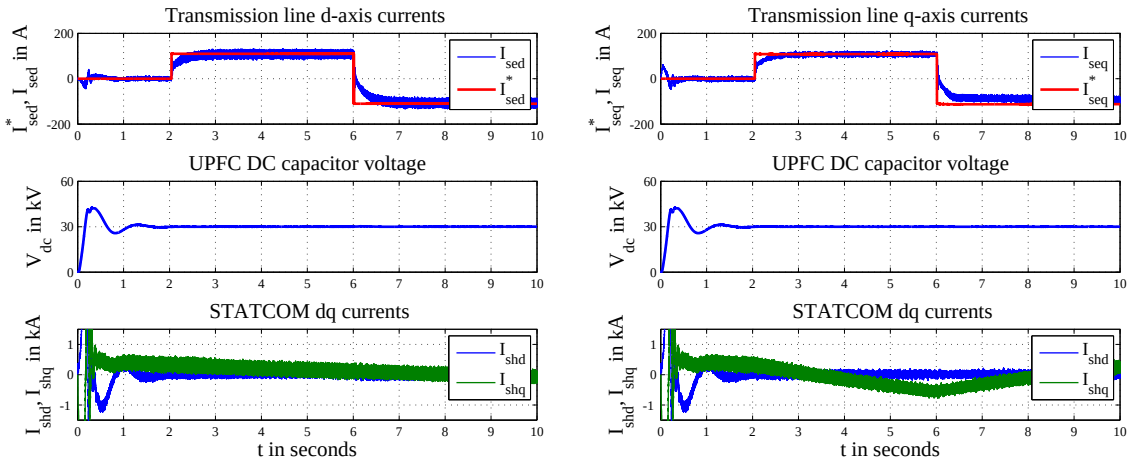

Figure 3.12: UPFC currents and DC capacitor voltage plots for changing P^*_{se} and Q^*_{se}

system is then calculated as [35]

$$\omega_n = \frac{\sqrt{(\omega_e L + K_P)^2 + (R + K_r)^2}}{L}$$
$$\zeta = \frac{R + K_r}{\sqrt{(\omega_e L + K_p)^2 + (R + K_r)^2}} \tag{3.19}$$

The settling time can then be calculated as:

$$\tau = \frac{1}{\zeta \omega_n} = \frac{L}{R + K_r} \tag{3.20}$$

Inspection of equations (3.19) and (3.20) reveals the fact that both damping and response time of UPFC can be controlled to some extent by adjusting K_r. Increasing K_r decreases the system response time. However there should be a compromise between faster response and damping. From equation (3.19), K_r will be calculated as

$$K_r = \frac{\zeta \sqrt{(\omega_e L + K_p)^2}}{\sqrt{1 - \zeta^2}} - R \tag{3.21}$$

Figure 3.12 shows the performance of a UPFC for different real and reactive power commands.

Figure 3.12a shows the performance of the UPFC when the real power reference is varied while the reactive power reference is kept fixed at 0 $MVAr$. The real power reference P^*_{se} is changed to 5 MW at $t = 2$ s and it is sent to the controller as a current command I^*_{sed}. The controller tracks I^*_{sed} and the the d-axis transmission line current changes to match the requested real power command. At $t = 6$ s, P^*_{se} is changed to -5 MW which is also tracked by the controller.

Figure 3.12b shows the performance of the UPFC when the reactive power reference is varied while the real power reference is kept fixed at 0 MW. The reactive power reference Q^*_{se} is changed to 5 $MVAr$ at $t = 2$ s and it is sent to the controller as a current command I^*_{seq}. The controller tracks I^*_{seq} and the the q-axis transmission line current changes to match the requested real power command. At $t = 6$ s, Q^*_{se} is changed to -5 $MVAr$, which the controller attempts to track, however the requested reactive power command reduces the line voltage at the sending end. This has the adverse effect that the current reference I^*_{seq} is pushed even higher, which the controller then tries to track. The reactive current I_{shq} supplied by the shunt converter changes to regulate the changing sending end voltage and can be seen in figure 3.12b.

3.4 Conclusion

This chapter discussed the control and performance of various FACTS devices like the STATCOM, SSSC and the UPFC. The performance of the PST was included in this chapter, since it is a popular alternative for FACTS devices in power flow control. It was noted that the PST can control both real and reactive power along a transmission line, just like the UPFC. However, the PST has large reactive power requirements as compared to the UPFC. Further, it involves mechanical current carrying moving parts like the load tap changer (LTC) which require a lot of maintenance for its proper operation.

Two control schemes for the STATCOM and SSSC were discussed: Angle control, and Vector control. Angle control is a non-linear control scheme where complex voltage phasor generated by the VSC is controlled using a single variable, namely the voltage angle α. Vector control, on the other hand, uses a linear control scheme to generate two orthogonal voltage

commands along the d- and q- axes. These voltage commands are used to generate switching pulses for the VSC using pulse width modulation. Finally, a description of the UPFC, which is the combination of a SSSC and STATCOM, was given and its control was explained in detail.

In addition to the control objectives discussed in this chapter, FACTS controllers can also be used as dampers for power oscillations, usually caused by reduction in system inertia. As discussed in chapter 2, reduction in system inertia could be due to several reasons, like loss of generation or increased renewable penetration. Design and performance of damping controllers for FACTS devices is explored in Chapter 6.

Chapter 4

Multi-Area Power System Model Identification

4.1 Introduction

Chapter 2 discusses the performance of renewable energy resources and highlights the problems that will emerge after the gradual replacement of conventional energy resources with renewables. However, the impact of renewables on a large power system can be quantitatively explained through actual simulation of the large power system with renewable energy penetration.

Given the large size of any realistic power system, such as the Western Electricity Coordinating Council (WECC), it is very difficult to derive the pre-event or post-event dynamic model for an entire network using measurements in real-time. System operators are, rather, more interested in constructing reduced-order models that capture the dominant inter-area modes of oscillations for their system [38]. Once constructed, these models can be continuously updated with newer measurements at regular intervals of time, and used for accurate prediction of the frequency and damping with which the different coherent clusters of the system may oscillate with respect to each other in face of any future event. Such reduced-order models are often referred to as *wide-area* models [39]-[40].

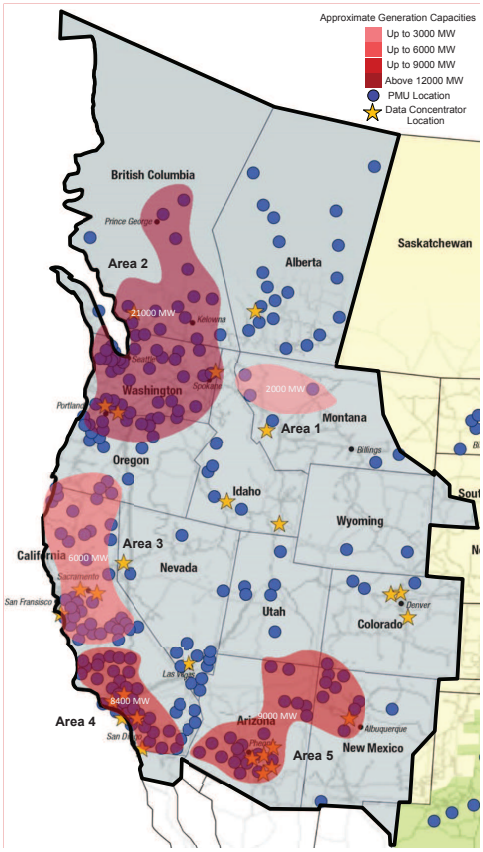

Figure 4.1: WECC 500 kV transmission grid divided into five coherent generation areas, indicated by red. The color map indicates the amount of generation provided by any area. Blue circles indicate PMU locations.

Such a wide-area model of the WECC power system, starting from the major generation clusters in Alberta, Washington and Oregon to the load clusters in Southern California, Montana and Arizona with intermediate voltage support at appropriate points is shown in fig. 4.1, referenced from [41]. This figure shows the wide-area view of the WECC transmission grid, breaking the system into five well-defined, and well-recognized coherent generation/load clusters that oscillate with respect to each other in face of different disturbances. Various characteristics of these inter-area oscillations have been studied extensively over the past decade using synchrophasors [42]-[43], and are well-understood for the traditional operating conditions of the WECC. However, with gradual expansion in transmission infrastructure as well as tremendous

penetration of renewable power including wind and solar photovoltaic in the west coast over the next decade, several dynamical properties of the WECC will change significantly, and so will the characteristics of the inter-area oscillations and their stability margins. Such projected changes are neither well-understood from an analytical perspective nor well-established from an experimental or validation point of view.

The goal of this chapter is to bridge this gap by investigating how real-time changes in operating conditions, unforeseen contingencies, and amount of renewable generation have an impact on the inter-area oscillations in WECC, and validate those observations using a real-time emulation framework. This goal is achieved by identifying a five-machine equivalent model of the five-area WECC 500 kV power system as shown in fig. 4.2 using PMU measurements collected from the terminal buses of each area. This model is implemented in a Real-time Digital Simulator (RTDS), and tune its parameters for model validation. Thereafter, the model is used to emulate the inter-area power flow oscillations in response to different types of disturbances such as generator losses and line losses, as well as wind power penetration, and predict the resulting slow oscillation frequency and damping. An algorithm is proposed to determine the criticality of line loss events within any area based on the divergence of load flow. The model allows us to test the sensitivity of the phase angle and frequency responses of any area to wind injection in any other area, and also the limiting value of the penetration beyond which dynamic performance starts degrading significantly. A series of experiments is carried out to illustrate these sensitivity factors for different levels and locations of wind injection in WECC.

4.2 Description of the five-area model

The WECC 500 kV network is divided into five coherent non-overlapping areas as shown in Fig. 4.2. Each area is associated with a unique terminal bus, which is a 500 kV substation, conveniently referred to as a pilot bus. The identity of the pilot bus is chosen such that

1. The substation must have a PMU installed at its location

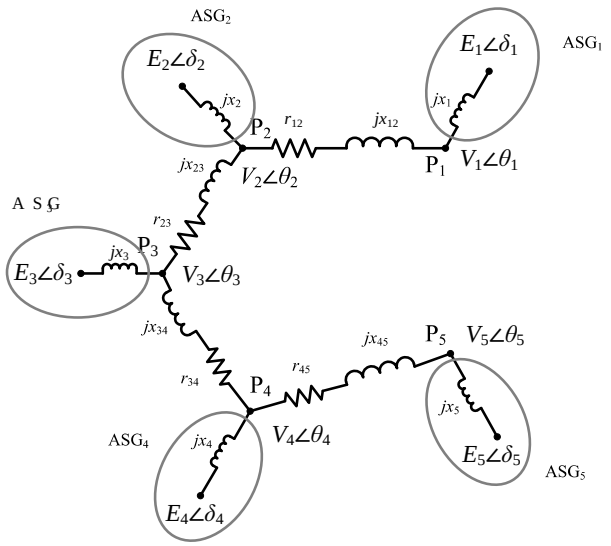

Figure 4.2: Five-machine equivalent of WECC. The linear topology is validated by oscillation analyses in WECC [41].

2. All generators within that area must lie electrically behind this substation.

A dynamic equivalent model for this network is then constructed by assuming each area to be an equivalent generator, also referred to as an aggregated synchronous generator (ASG), with the interconnecting 500 kV lines between the pilot buses of any two areas reduced to a single equivalent transmission line, as shown in Fig. 4.2. The identity of the pilot bus of every area is, therefore, retained in the reduced-order model. The buses are considered to be connected in a line topology following the model given in [41]. The impedance of the equivalent tie-line between pilot buses P_i and P_j is denoted as $r_{ij} + x_{ij}$.

The voltage phasor $V_i\angle\theta_i$ is known at each pilot bus P_i owing to availability of PMU data at that bus. Furthermore, the current $I_i\angle\alpha_i$ being injected at each pilot bus P_i can be calculated from the difference in line currents flowing in and out of that pilot bus. Looking from the pilot bus into the area, the equivalent generator is modeled as a Thevenin voltage source with internal EMF $E_i\angle\delta_i(t)$, and Thevenin reactance $Z_i = jx_i$. It can be shown that if the Thevenin impedance is considered as $r_i + jx_i$ then the system may become unidentifiable. This is further elaborated upon in Section 4.3.2.

The aggregated synchronous generator is modeled as a second-order damped oscillator described by the swing equation [44]:

$$M_i\ddot{\delta}_i(t) = P_{mi} - \frac{E_i V_i(t)}{x_i}\sin\left(\delta_i(t) - \theta_i(t)\right) - D_i\dot{\delta}_i(t) \tag{4.1}$$

where M_i, P_{mi} and D_i are the equivalent inertia, mechanical power input and damping factor of the i^{th} ASG. Since ASG_i is a fictitious generator, field measurements for this generator are not available, and hence higher-order models of synchronous generators are not used for analysis. Our objective is to use PMU measurements of $V_i\angle\theta_i$, $I_i\angle\alpha_i$, $i = 1, ..., 5$ in the actual system to identify the following parameters of the equivalent model, namely:

1. Identification of inter-area tie-line impedance $r_{ij} + jx_{ij}$
2. Identification of Thevenin reactance jx_i of ASG_i
3. Identification of inertia M_i and damping D_i of ASG_i

Since the ASG_i is obtained by collapsing the coherent areas of the network so that the reduced-order model only captures the inter-area oscillation dynamics, the fast oscillation modes in the PMU data resulting from intra-area oscillations between local generators in area A_i must be removed. Considering a small-signal model of the actual WECC system, due to clustering any PMU measurement can be decomposed as

$$y(t) = \underbrace{y_0(t)}_{\text{DC modes}} + \underbrace{\sum_{i=1}^{r} R_i e^{(\sigma_i + j\omega_i)t}}_{y_s(t)\text{: Inter-area modes}} + \underbrace{\sum_{k=r+1}^{N} R_k e^{(\sigma_k + j\omega_k)t}}_{y_f(t)\text{: Intra-area modes}}. \tag{4.2}$$

The number r is selected such that $\omega_i \,\epsilon\, (0, 2\pi]$ rad/s, assuming that all inter-area modes for WECC are less than 1 Hz [45]. Depending on baselining of the system using historical PMU data, this range can be expanded or reduced for better estimation. The first task is to apply any standard modal decomposition method (for example, see [42, 43, 46]) to extract $y_s(t)$ from the phase angle and frequency measurements at the five pilot buses. In the next sections we

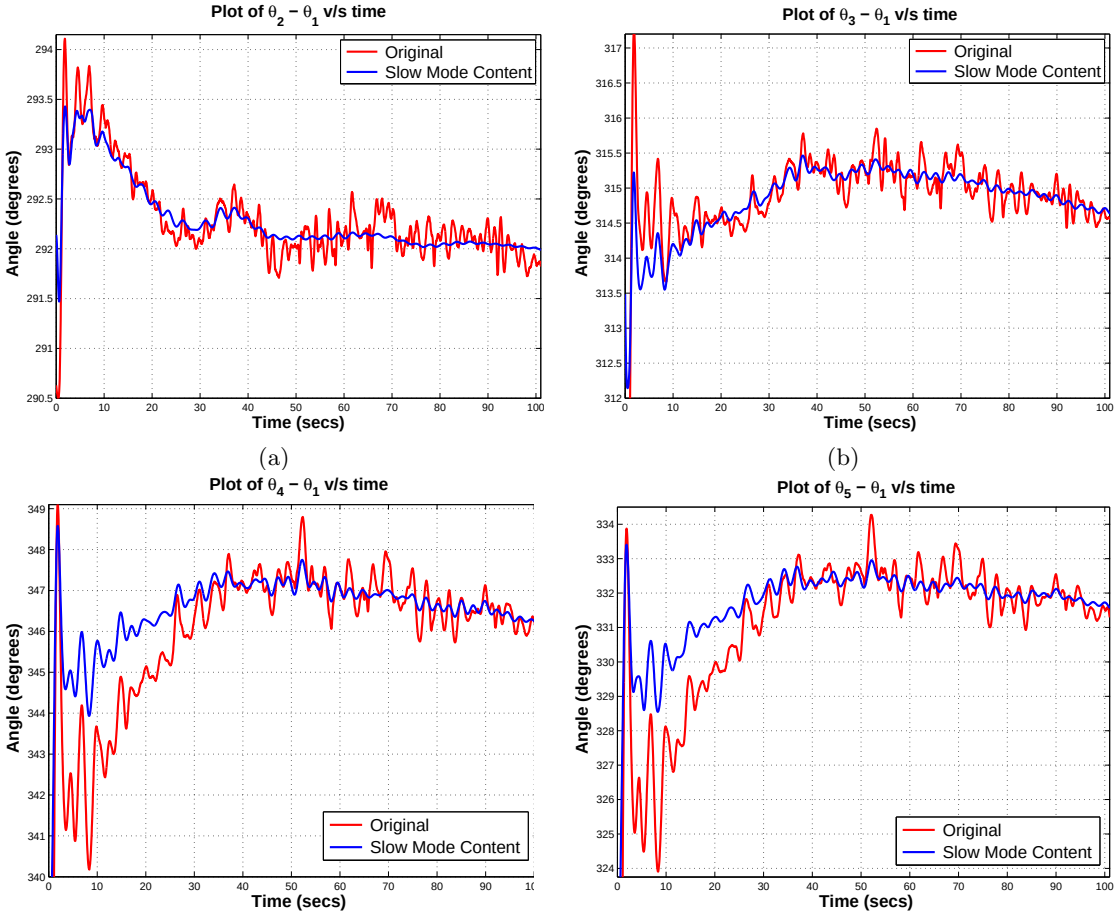

Figure 4.3: Voltage angle data for four pilot buses and their slow mode content

describe how we can use $y_s(t)$ to identify reduced-order model parameters. Fig. 4.3 shows the application of Prony analysis on the pair-wise difference between voltage angles of two consecutive buses from fig. 4.1.

4.3 Identification of model parameters

4.3.1 Identification of inter-area tie-line impedance

The reduced-order model assumes that each pilot bus P_i is connected to the next pilot bus P_j through a single equivalent transmission line. Since this line is a reduction of several long 500 kV transmission lines, ideally speaking an equivalent-π model of the transmission line should be used. However, in order to calculate the equivalent shunt admittance at the end of each line, we require the voltage at the pilot buses as well as the line charging current. If the line charging current at any bus is not available from PMU data then it is not possible to estimate the equivalent shunt admittance. The following two approaches can be adopted in such a scenario:

1. The shunt admittance values of a transmission line of a given length can be estimated from typical values of admittance per mile values for 500 kV transmission lines for a given conductor configuration, or

2. The shunt admittance of the transmission lines can be merged with the shunt load present at the ASG, thus effectively eliminating them from the computation.

To ensure that all parameters can be evaluated using PMU data only, the second approach is adopted in this chapter and the long transmission lines are represented by pure series impedance. Additionally, physical 500 kV lines between every pair of pilot buses are identified, and lines with substantially larger currents are selected for analysis. The net current $I_{ij}(t)\angle\beta_{ij}(t)$ along the fictitious transmission line is taken as the phasor sum of the currents in the selected transmission lines at any point of time t. Using the voltages and currents thus obtained, the inter-tie

impedance can be calculated using Ohm's law in the phasor domain as,

$$V_i\angle\theta_i(t) - V_j\angle\theta_j(t) = I_{ij}\angle\beta_{ij}(t) \cdot Z\angle\theta_z. \tag{4.3}$$

Separating out real and imaginary parts, the estimation of Z and θ_z can then be posed as the following non-linear least squares problem [47]:

$$\min_{Z,\theta_z} \int_0^T \left|\left| \begin{array}{c} V_i\cos\theta_i - V_j\cos\theta_j - I_{ij}Z\cos\gamma \\ V_i\sin\theta_i - V_j\sin\theta_j - I_{ij}Z\sin\gamma \end{array} \right|\right|_2^2 dt \tag{4.4}$$

where $\gamma = \theta_z + \beta_{ij}$. For this particular case study, the impedance values for the various equivalent transmission lines were observed to be fairly constant over time if they are computed for each time point using (4.3) instead of (4.4). These values were averaged over time, and the average closely matched the solution of (4.4).

4.3.2 Identification of Intra-Area Thevenin reactance

After the estimation of "inter-tie" impedances, the next step is to estimate the small "intra-tie" impedance values that connect the generator voltage source to the respective pilot bus. Following a classical generator model for every ASG, we assume E_i to be constant, albeit unknown. Field dynamics are ignored due to the absence of field currents and voltages for any ASG. From fig. 4.4, it is clear that the phasors $\bar{E}$, $\bar{V}$ and $\bar{I}Z$ at any time t for any ASG_i form a triangle, with both $\bar{E}$ and $\bar{I}Z$ being unknown at all times. V is known, but E and IZ both can take an infinite pair of values so that they satisfy Ohm's law. Hence, to make the system identifiable, the following assumptions are made:

1. $E_i = 1\ p.u.$, and

2. $r_i = 0$, i.e. $Z_i = jx_i$.

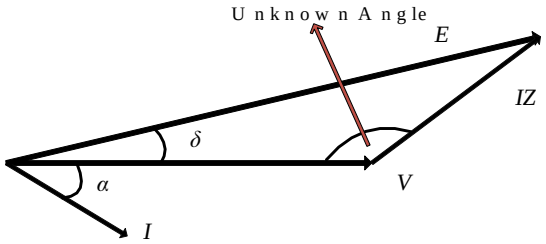

Figure 4.4: Phasor Diagram for the Aggregated Synchronous Generator

If we apply sine rule to the triangle using the above two assumptions, the following two equations can be written:

$$\left.\begin{array}{rcl} \delta_i(t) & = & \cos^{-1}(V_i(t)\cos\alpha_i(t)) - \alpha_i(t) \\ x_i & = & \frac{\sin\delta_i(t)}{I_i\cos\alpha_i(t)} \end{array}\right\} \tag{4.5}$$

The estimate of x_i was generated by solving (4.5) algebraically at every time step. The final value of x_i for each ASG_i was obtained by taking its average over the defined time interval. An alternative would be to compute the least squares estimate using the non-linear least squares formulation similar to (4.4). The estimated value of x_i is affected by changes in power flows within area A_i, so the pre- and post-disturbance values of x_i differ slightly from each other. Pre-disturbance values of x_i were considered for estimation of M_i and D_i as well as in the reduced-order dynamic model implemented in the RTDS.

4.3.3 Identification of Inertia and Damping

Linearize (4.1) under the assumption that the steady state value of rotor speed, $\omega_s = 1\ p.u.$. If the p.u. deviation in speed is defined as $\omega_i = (\omega_{ri} - \omega_s)/\omega_s = \dot{\delta}_i/\omega_s$,

$$\begin{bmatrix} \Delta\dot{\delta}_i \\ \Delta\dot{\omega}_i \end{bmatrix} = \begin{bmatrix} \omega_s\Delta\omega_i \\ \frac{-2D_i}{M_i}\Delta\omega_i - \frac{1}{M_i}\Delta P_{ei} + \frac{1}{M_i}\Delta P_{mi} \end{bmatrix} \tag{4.6}$$

where ω_{ri} is the actual rotor speed. However, the expression for P_{ei} is given as

$$P_{ei} = \frac{E_i V_i}{x_i} \sin(\delta_i - \theta_i) \tag{4.7}$$

Linearizing (4.7), we get an expression for the small signal variation in $P_e = col(P_{e1}, ..., P_{e5})$,

$$\begin{aligned} \Delta P_e &= diag\left(\frac{E_i}{x_i} \sin(\delta_{i0} - \theta_{i0})\right) \Delta V(t) \\ &+ diag\left(\frac{E_i V_{i0}}{x_i} \cos(\delta_{i0} - \theta_{i0})\right) \Delta\delta(t) \\ &- diag\left(\frac{E_i V_{i0}}{x_i} \cos(\delta_{i0} - \theta_{i0})\right) \Delta\theta(t) \end{aligned} \tag{4.8}$$

where V_{i0}, θ_{i0} and δ_{i0} represent the steady-state values of V_i, θ_i and δ_i. For the network, $\vec{I} = \bar{Y}_{bus}\vec{V}$ can be written using Kirchoff's Current law, where Y_{bus} is the bus admittance matrix. But for the generators, from Kirchoff's Voltage law, $\vec{I} = \bar{Y}_g(\vec{E} - \vec{V})$, where $\bar{Y}_g = diag(1/jx_i)$. Combining these equations, we get $\vec{V} = \bar{Y}\vec{E}$, where $\bar{Y} = (\bar{Y}_{bus} + \bar{Y}_g)^{-1}\bar{Y}_g$. Separating out real and imaginary parts,

$$V_R = V_i \cos\theta_i = Y_R E_i \cos\delta_i - Y_I E_i \sin\delta_i \tag{4.9}$$

$$V_I = V_i \sin\theta_i = Y_I E_i \cos\delta_i + Y_R E_i \sin\delta_i \tag{4.10}$$

where $\bar{Y} = Y_R + jY_I$, and Y_R and Y_I are real matrices. Linearizing (4.9) and (4.10), it can be easily shown that

$$\begin{bmatrix} \Delta V(t) \\ \Delta\theta(t) \end{bmatrix} = \begin{bmatrix} F & 0_{5\times5} \\ G & 0_{5\times5} \end{bmatrix} \begin{bmatrix} \Delta\delta(t) \\ \Delta\omega(t) \end{bmatrix}$$

$$\text{where } \begin{bmatrix} F \\ G \end{bmatrix} = \begin{bmatrix} diag(\cos\theta_{i0}) & -diag(V_{i0}\sin\theta_{i0}) \\ diag(\sin\theta_{i0}) & -diag(V_{i0}\cos\theta_{i0}) \end{bmatrix}^{-1} \times \begin{bmatrix} -Y_R diag(E_i\sin\delta_{i0}) & -Y_I diag(E_i\cos\delta_{i0}) \\ Y_R diag(E_i\cos\delta_{i0}) & -Y_I diag(E_i\sin\delta_{i0}) \end{bmatrix} \quad (4.11)$$

Substituting (4.11) in (4.8), ΔP_e can be expressed purely as a function of $\Delta\delta$ as follows,

$$\begin{aligned} \Delta P_e &= \Big[diag\left(\tfrac{E_i}{x_i}\sin(\delta_{i0}-\theta_{i0})\right)F \\ &\quad + \; diag\left(\tfrac{E_iV_{i0}}{x_i}\cos(\delta_{i0}-\theta_{i0})\right)(I-G)\Big]\Delta\delta \\ &= L\Delta\delta \end{aligned} \quad (4.12)$$

Substituting (4.12) in (4.6), Equation (4.13) is obtained.

$$\underbrace{\begin{bmatrix} \Delta\dot{\delta} \\ \Delta\dot{\omega} \end{bmatrix}}_{\dot{X}} = \underbrace{\begin{bmatrix} 0_{5\times5} & \omega_s I_{5\times5} \\ diag\left(\frac{-1}{M_i}\right)L & diag\left(\frac{-2D_i}{M_i}\right) \end{bmatrix}}_{A} \underbrace{\begin{bmatrix} \Delta\delta \\ \Delta\omega \end{bmatrix}}_{X} + \underbrace{\begin{bmatrix} 0_{5\times5} \\ diag\left(\frac{1}{M_i}\right) \end{bmatrix}}_{B} \underbrace{\Delta P_m}_{U} \quad (4.13)$$

where $\Delta\delta = col(\Delta\delta_1, ..., \Delta\delta_5)$, $\Delta\omega = col(\Delta\omega_1, ..., \Delta\omega_5)$, $\Delta P_m = col(\Delta P_{m1}, ..., \Delta P_{m5})$, $\Delta V = col(\Delta V_1, ..., \Delta V_5)$ and $\Delta\theta = col(\Delta\theta_1, ..., \Delta\theta_5)$. The prefix Δ denotes a small-signal change over the pre-existing equilibrium. Equation (4.11) shows the small-signal change in the pilot bus

voltage and angles as a function of the state variables,

$$\underbrace{\begin{bmatrix} \Delta V(t) \\ \Delta\theta(t) \end{bmatrix}}_{Y} = \underbrace{\begin{bmatrix} F & 0_{5\times5} \\ G & 0_{5\times5} \end{bmatrix}}_{C} \underbrace{\begin{bmatrix} \Delta\delta(t) \\ \Delta\omega(t) \end{bmatrix}}_{X} \tag{4.14}$$

Equations (4.13)-(4.14) are of the form

$$\left.\begin{aligned} \dot{X}(t) = AX(t) + BU(t), \;\; X(0) = X_0 \\ Y(t) = CX(t). \end{aligned}\right\} \tag{4.15}$$

The estimation of M_i, D_i, ΔP_{mi}, $i = 1, ..., 5$, can then be posed as the following non-linear least squares problem:

$$\min_{M_i, D_i, \Delta P_{mi}} \int_{t=0}^{t^*} \|Y(t) - \hat{Y}(t)\|_2^2 dt \tag{4.16}$$

where

$$\hat{Y}(t) = Ce^{At}X(0) + \int_{\tau=0}^{t} Ce^{A(t-\tau)}B\Delta P_m d\tau, \tag{4.17}$$

$Y(t)$ is the PMU data stream post modal decomposition, and t^* is the length of time selected so as to include all the post-disturbance oscillations. Estimation of M_i, D_i, ΔP_{mi} from (4.16) completes the identification of the reduced-order system. The actual least squares estimation was limited to consider only the small-signal pilot bus voltage angles $\Delta\theta$, i.e. the following output equation, $\Delta\theta(t)_{5\times1} = G_{5\times5}\Delta\delta(t)_{5\times1}$ was considered. The actual PMU data stream can vary between 3 to 5 minutes in duration, and using the entire length of data gives no advantage in estimation of dynamic parameters, while it increases the computational costs at the same time. Hence, in these estimations, t^* is defined as the time interval from the start of the disturbance event to the point where the oscillations are indistinguishable from noise in the PMU data stream.

Table 4.1: Parameters used in simulation

Machine	Station 1	Station 2	Station 3	Station 4	Station 5
Inertia (MW-s/MVA)	75	162.92	244.636	32.42	24.82
Damping (p.u./p.u.)	10	15	3.688	0.594	0.621
Rated MVA	1500	2500	3000	3000	3000
Machine Internal Voltage	1.012 pu	0.995 pu	1.023 pu	0.988 pu	0.997 pu
Bus Load Prefault MW	0	679	3000	2791	1000
Bus Load Postfault MW	0	0	3000	2000	2216
Pre-Fault Governor Setting	0.4926 pu	0.8646 pu	0.4687 pu	0.6389 pu	0.5856 pu
Post-Fault Governor Setting	0.4644 pu	0.8349 pu	0.4068 pu	0.6780 pu	0.5705 pu
Calculated Tie-line Reactance	$24.8986j$	$18.1871j$	$-3.4j$	$18.7462j$	$34.4729j$
Used Tie-line Reactance	$24.8986j$	$18.1871j$	$18.7462j$	$18.7462j$	$34.4729j$
Exciter Model (IEEE)	Type ST1	Type ST1	Type ST1	Type ST1	Type ST1
Governor model (IEEE)	Type 1	Type 1	Type 1	Type 1	Type 1
Bus Type	PQ	PQ	Slack	PQ	PQ

4.4 Tuning for Model Validation

The output of the identified model already matches the PMU measurements in a least-squares sense. Therefore, one may question the necessity of validating the model further. The reason, however, is that, theoretically speaking, the identification is done only for the second-order ideal swing model (4.13), but when this model is implemented in RTDS using RSCAD, one must design additional generator components such as the excitation system, AVR, power system stabilizers, and governors, each of which has its own nonlinear dynamics that were not identified in the steps listed in section III. Therefore, upon implementation of this software model, the predicted response may not match the response of the identified model. A second round of parameter tuning is needed. We next describe the steps of this tuning process. Table 4.1 gives an overview of all the final values used in the tuned model.

4.4.1 Capacitor at Station 3

The estimate of the intra-area or internal reactance of the ASG at Station 3 was found to be negative, indicating a large capacitive VAR flow in the line. This observation is consistent with the fact that there is indeed a large switched capacitor bank near the location of the pilot bus

Table 4.2: Estimated inter-tie impedance values

Line	Reactance
Station 1 - Station 2	$56.34 + 120.39j$
Station 2 - Station 3	$0.64 + 22.67j$
Station 3 - Station 4	$30.83 + 81.16j$
Station 4 - Station 5	$11.03 + 94.51j$

Table 4.3: Validation of Pilot Bus Voltages via Load Flow

Bus	Voltage	
	Simulated	PMU Data
Station 1	1.012 pu	0.996 pu
Station 2	0.995 pu	0.963 pu
Station 3	1.023 pu	1.006 pu
Station 4	0.988 pu	0.977 pu
Station 5	0.997 pu	0.982 pu

3 [48]. However, no data pertinent to the number of capacitor banks switched in during the event was available. Therefore, a capacitor bank was considered at Station 3 in the RSCAD simulation whose size was determined by matching the pre-fault voltage at Station 3 with that observed from the PMU data. The final values of the inter-area impedances are given in Table 4.2.

4.4.2 Voltage Tuning

Though matching of phase angles (or power flow) and frequency is of primary interest for oscillation analysis, matching the bus voltages to a reasonable level of accuracy is also important. Internal generator voltages were therefore, tuned so that load-flow compilation yielded a close match of the pilot bus voltage to that observed from the PMU measurements. Table 4.3 lists the voltages from RTDS versus that in the PMU data. The values are within two percent of each other.

Table 4.4: Voltage angle and Power flow change across Inter-area tie-lines

Line	Angle			Power Flow in MW		
	Pre-fault	Post-fault	$\Delta\theta$	Pre-fault	Post-fault	ΔP
Station 1 -Station 2	17.45°	17.49°	0.04°	669	670.5	1.5
Station 2 -Station 3	8.43°	11.15°	2.72°	1916	2595	679
Station 3 -Station 4	-4.02°	-10.98°	-6.96°	-247	-672	-425
Station 4 -Station 5	12.38°	-11.17°	-23.6°	639	-577	-1216

4.4.3 Matching post-fault power flows with switched loads

At the instant of the fault or disturbance, the phase angles show a sudden sharp increase or decrease from their equilibrium values. The actual values of these changes are shown in table 4.4. Three of the four phase angles in the filtered PMU data (i.e., after modal decomposition) display a large change in angle at the immediate time of the fault. Using (4.1), it is possible to calculate the change in power necessary to recreate these instantaneous phase angle changes. This was modeled by adding or subtracting resistive loads on appropriate buses.

The pre- and post-fault steady-state phase angles were further tuned using the governor load reference set-points. The values of the steady-state phase angles pre- and post-fault are compared against the PMU data in Table 4.5. Essentially, the machines have different power set-points post-fault compared to pre-fault. This change has allowed very close matching of the steady-state phase angles. The exact values used for these governor load reference set points are shown in Table 4.1. It should be noted that changing the governor setpoint changes the phase angles across the lines over a slower time-scale than changing the immediate load at each pilot bus. In order to recreate both the sharp changes occurring at the instant of the fault as well as the slow dynamic response of the angles together with their eventual convergence to the respective steady-state values, both of these methods were implemented together.

Table 4.5: Simulated v/s real values of Pilot Bus Angles

Line	Pre-fault Angle		Post-fault Angle	
	Simulated	Real Data	Simulated	Real Data
Station 1-Station 2	17.45°	17.45°	17.48°	17.49°
Station 2-Station 3	8.44°	8.43°	11.17°	11.15°
Station 3-Station 4	-4.02°	-4.02°	-10.98°	-10.98°
Station 4-Station 5	12.38°	12.38°	-11.18°	-11.17°

Table 4.6: Inertia and Damping

Machine	Inertia		Damping	
	Calculated	Model	Calculated	Model
Station 1	1.257	75	4.776	10
Station 2	162.920	162.920	15	15
Station 3	244.636	244.636	3.688	3.688
Station 4	32.420	32.420	0.594	0.594
Station 5	24.82	24.82	0.621	0.621

4.4.4 Tuning Inertias and Damping Factors

The estimated values of the inertia and damping factors of the aggregated machines in the identified model are shown in Table 4.6. The inertia and damping of ASG_1, both of which are relatively small, were retuned such that the transient response of the RSCAD model matches the filtered PMU data, again in a least squares sense. This matching is shown in fig. 4.5.

4.5 Predicting Stability Margins

The reduced-order model is next used for predicting the dynamic responses of the power flows between every pair of machines, which in the actual WECC system will correspond to the power transfer between those two areas, following three common contingencies:

1. Generator tripping resulting in loss of injected power at a pilot bus and inertia of the corresponding ASG

2. Line tripping resulting in increase in intra-area reactance

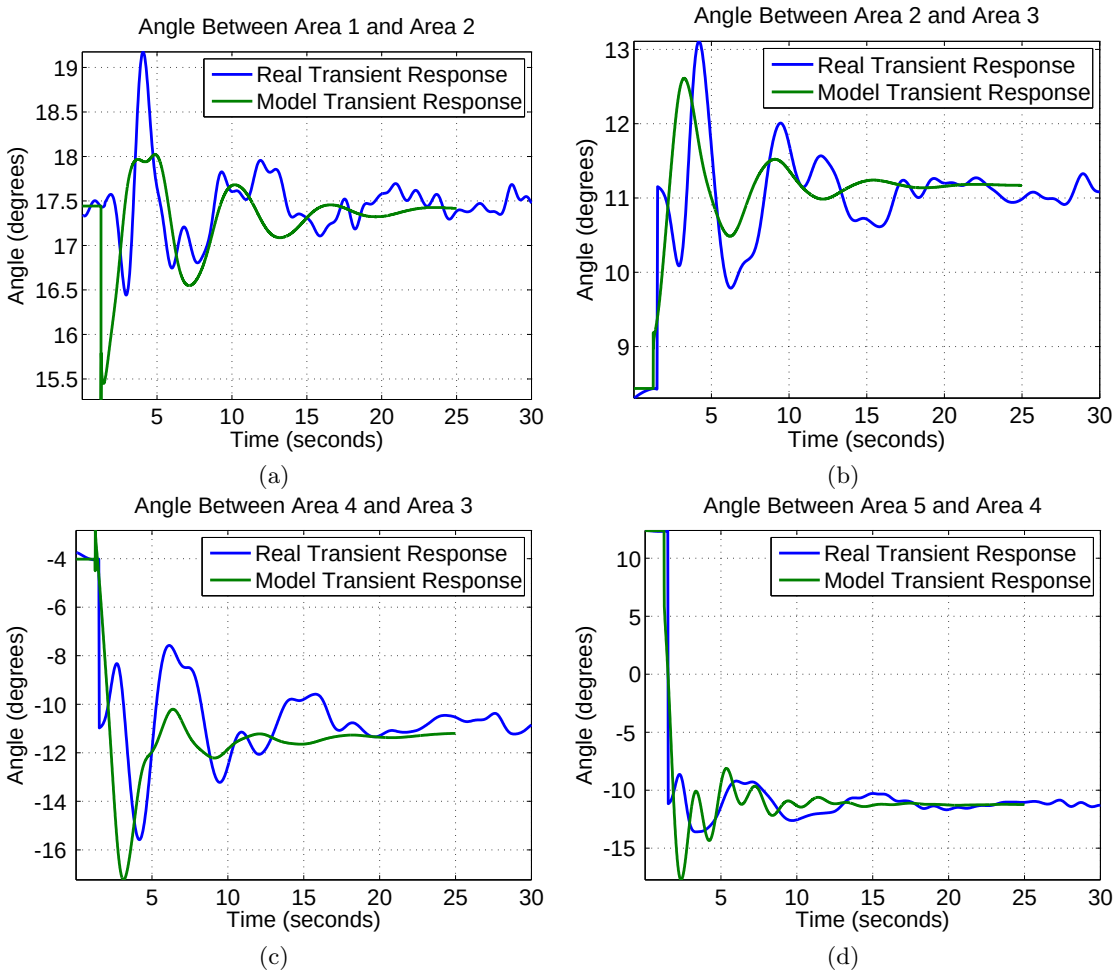

Figure 4.5: Comparison of simulated versus actual phase angle difference

3. Addition of wind turbines (modeled by doubly-fed induction generators) at pilot buses, also resulting in an effective loss of inertia of the corresponding ASG.

The effects of generator trips are relatively simpler to emulate by manipulating the generation rating and inertia of the ASGs. Detailed simulations for this type of disturbance will be shown in the next section. The line trip events are further elaborated as follows.

For any area S_i with N_i buses, the equivalent admittance matrix Y_{bus_i} is known to the operator of that given area, along with the admittance matrix Y_{ro} for the reduced order WECC network. Also it is assumed that the operator of that area has knowledge of the pre-disturbance

power flow of area S_i as well as the power flow of the reduced order WECC model. Now, if a fault occurs within S_i, the current within the faulted line increases for a very short time and the line's protection system removes the line from the network. Mathematically, the removal of a line between buses i and j is be represented by updating y_{ij} and y_{ji} elements to zero, and adjusting y_{ii} and y_{jj} elements accordingly. Let Y'_{bus_i} be the modified admittance matrix of the network after the line is removed. The admittance matrices of S_i and WECC's reduced order model are combined as follows:

$$Y_{c_i} = \begin{bmatrix} Y'_{bus_i} & Y_{cp} \\ Y_{cp}^T & Y_{ro} \end{bmatrix}. \tag{4.18}$$

Here Y_{cp} represents the inter-tie admittance between pilot bus S_i and the other pilot buses, and is a relatively sparse matrix. The resultant network has $N_i + 4$ buses, making Y_{bus_c} a square matrix of size $N_i + 4$. Assuming that the power set-points of the ASGs do not change significantly due to this line loss, the power flow at PV or PQ bus j is given as,

$$P_j = Re\left[\tilde{V_j} \cdot \sum_{k=1}^{N_i+4} Y_{c_i}(j,k) \cdot \tilde{V_k}\right] \tag{4.19}$$

$$Q_j = -Im\left[\tilde{V_j} \cdot \sum_{k=1}^{N_i+4} Y_{c_i}(j,k) \cdot \tilde{V_k}\right] \tag{4.20}$$

We solve these power flow equations for every bus j using Newton-Raphson's method, and compute the updated value of $V_j \angle \theta_j$ for the j^{th} bus. The updated value of the voltage phasor at the pilot bus of area S_i can then be used to estimate the new value of x_i using (4.5). We also develop Algorithm 1 to compute the maximum allowable line loss that leads to the critical value of x_i^c for which the identified model shows an unacceptably large magnitude of inter-area oscillations. The value of x_i^c can be obtained by simulating the reduced-order model for incremental values of x_i, and tracking the point at which sustained oscillations are observed in the phase angle difference between the pilot buses. This indicates that in the actual WECC system, every area-level operator must keep track of the lines and load changes inside their areas such that the aggregated value of x_i does not fall below the critical value x_i^c. Although it

Algorithm 1 Determine criticality of a line within area S_i

1: **Input:** Y_{bus_i}, Admittance matrix of area S_i
2: **Trip** a new line within S_i
3: **Update** Y_{bus_i} to Y'_{bus_i} to reflect the loss of line
4: **Input:** Y_{ro}, Admittance matrix of WECC's reduced order network
5: **Combine** Y'_{bus_i} with Y_{ro} to form Y_{c_i}
6: **Compute** Power flow with pre-fault values for generation and loads at all buses and Y_{c_i} as the admittance matrix
7: **Update** $V_j \angle \theta_j$ at all buses
8: **Compute** x_i using (4.5) for pilot bus P_i
9: **Input:** $x_{i_{cr}}$, the value of internal reactance which produces sustained oscillations
10: **if** $x_i > x_{i_{cr}}$ **then**
11: **Mark** the line as critical for operation
12: **end if**
13: **Goto** Step 2

is not explicit from the above equations, loss of a line invariably results in an increase in internal reactance of a ASG. This is due to the dual effect of losing a line which directly influences x_i, and the increased power flow along the unaffected lines, which increases the effective magnitude of x_i due to in-feed effects.

The operator can perform this analysis for several scenarios using Algorithm 1 by modifying the admittance matrix in different ways. Each scenario will produce a value of x_i which can be compared against the critical value of x_i^c for that area.

Finally, the addition of wind farms in an area is modeled by inserting a doubly-fed induction generator (DFIG) at its pilot bus. Assuming that the total power output of the area remains constant, the inertia of the ASG is also decreased to model the replacement of synchronous power with DFIG power.

4.6 Predictive Analysis of various Contingencies

This section describes a series of experiments for simulating the dynamic response of the reduced-order model following the three types of disturbances listed in the previous section. These responses are used for predicting the frequency and damping factor of the inter-machine oscilla-

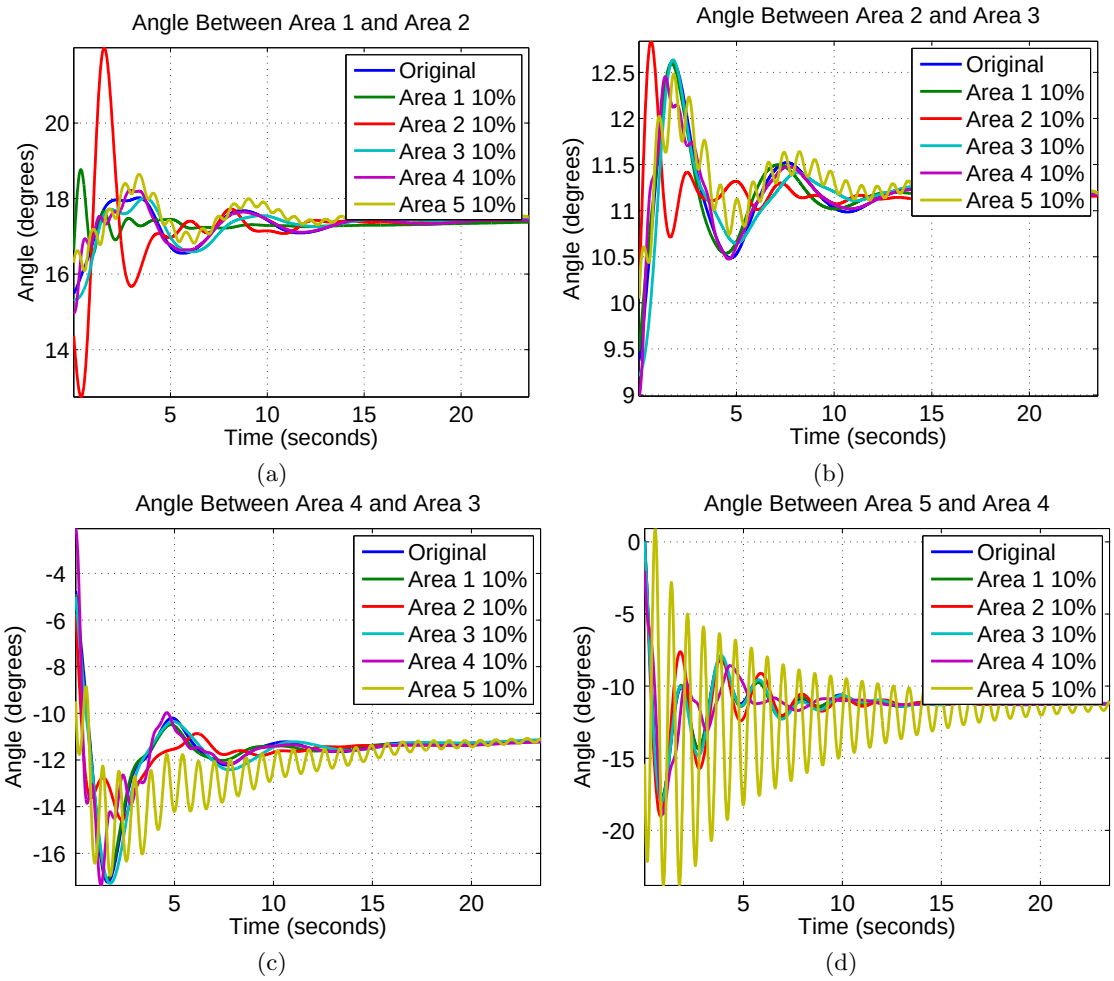

Figure 4.6: Inter-machine Phase Angle Responses for Inertia Loss Contingencies

tions, which in the actual WECC system will correspond to inter-area oscillations. Sensitivity of angle oscillations of any area with respect to disturbances occurring in other areas is also analyzed, thereby providing a way by which the WECC utilities can evaluate their dynamic coupling and dependence on their neighbors before any disturbance hit the system.

4.6.1 Loss of Inertia

An important point to remember is that unlike the small-signal model (4.13), the model implemented in RSCAD is highly nonlinear, similar to the real WECC system. Therefore, it was

Table 4.7: Modal Analysis of Power Flow with loss of inertia

$\Delta\theta$	No Inertia loss		S_1 Inertia Loss		S_2 Inertia Loss		S_3 Inertia Loss		S_4 Inertia Loss		S_5 Inertia Loss	
	Freq. (Hz)	Damp.	Freq. (Hz)	Damp.	Freq. (Hz)	Damp.	Freq. (Hz)	Damp.	Freq. (Hz)	Damp.	Freq. (Hz)	Damp.
$\theta_1 - \theta_2$	0.1376	0.1995	0.1621	0.2484	0.2168	0.2678	0.1237	0.3365	0.1346	0.1865	0.1263	0.8105
$\theta_2 - \theta_3$	0.1342	0.2447	0.1476	0.2749	0.2085	0.2217	0.1366	0.2472	0.1315	0.2484	0.1183	0.2532
$\theta_4 - \theta_3$	0.1425	0.2646	0.1584	0.3007	0.2384	0.6145	0.1351	0.2396	0.1442	0.2481	0.1338	0.2249
$\theta_5 - \theta_4$	0.4115	0.1065	0.4116	0.1066	0.4061	0.1084	0.4102	0.1072	0.3681	0.1481	1.0631	0.0167

noticed that very small changes in the generator inertias did not cause any significant change in the oscillatory characteristics. Our goal, therefore, was to perturb the system with medium to large changes in inertial values, and test the resulting nonlinear oscillations in the power flows. For example, in the first set of contingencies, the inertia of each machine was individually decreased by approximately fifty to ninety percent. A fault that simulates 1300 MW loss of generation in Area 5 was used to excite the model. The phase angle response across the four major transmission lines linking the five pilot buses was recorded. These phase angle plots are shown in fig. 4.6. Though all five cases are seen to be stable, some areas are more susceptible to loss of inertia than others. Area 5, in particular, is most susceptible, as testified by the intense underdamped oscillations that propagated all the way to Area 3 following the fault. Eigenvalue Realization Algorithm (ERA) [46] is applied to the power flows, and the most energetic modes from the modal decomposition are listed in Table 4.7. Inspection of this table clearly indicates that the bus whose ASG is subjected to the loss of inertia shows the highest increase in the slow mode frequency, as reflected in its power transfer with its neighboring buses.

4.6.2 Loss of internal tie-lines

For the second set of contingencies, the intra-area tie-line impedance of each ASG was increased individually by integer multiples of its identified value until the model became unstable. Again, note that a small-signal model will never become unstable due to such an increase. The instability is caused essentially due to the nonlinearity of the RSCAD model. Driving the system close to the verge of stability, an impulse fault was applied on all five pilot buses simultane-

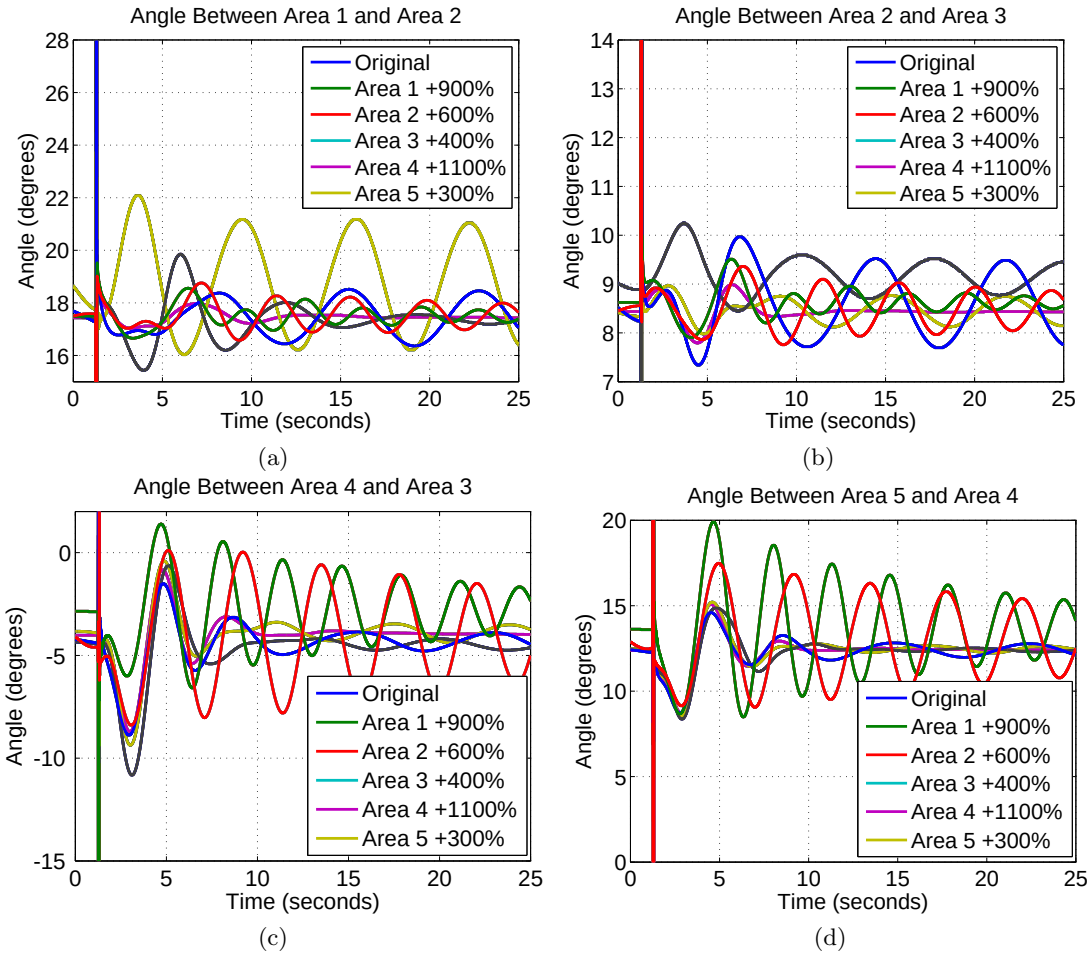

Figure 4.7: Inter-machine Phase Angle Responses for Increase in Intra-Area Impedance

ously to emulate a worst-case disturbance. The phase angle response across the four aggregated transmission lines are shown in fig. 4.7. The plots show that for this particular set of model parameters, x_1 (the internal reactance of Area 1) can be increased by a factor of ten before instability, whereas x_5 can be increased only by a factor of four. In every case there is one phase angle that is almost completely undamped. This is where the instability would start when the intra-area impedance is increased slightly above its critical value. ERA is applied to the power flows through the four lines. Table 4.8 lists the most energetic mode per curve from each plot. The table shows that critical line loss in Area 1 can lead to negative damping in the power flows between areas 2 and 3, and also areas 3 and 4. Similarly, critical line loss in Area 4 doubles

Table 4.8: Modal Analysis of Power Flow with Increase in intra-area impedance

$\Delta\theta$	No Line loss		Line Loss at S_1		Line Loss at S_2		Line Loss at S_3		Line Loss at S_4		Line Loss at S_5	
	Freq. (Hz)	Damp.	Freq. (Hz)	Damp.	Freq. (Hz)	Damp.	Freq. (Hz)	Damp.	Freq. (Hz)	Damp.	Freq. (Hz)	Damp.
$\theta_1 - \theta_2$	0.1365	0.2842	0.1306	0.0064	0.1241	0.2239	0.1131	-0.0055	0.2570	0.0180	0.1989	0.0380
$\theta_2 - \theta_3$	0.1006	0.4767	0.1293	-0.005	0.1100	0.0396	0.1119	0.0103	0.2557	0.0339	0.1926	0.0286
$\theta_4 - \theta_3$	0.1358	0.2503	0.1288	-0.0031	0.1122	0.1053	0.1157	0.0388	0.2551	0.0356	0.1952	0.0217
$\theta_5 - \theta_4$	0.1682	0.3659	0.1276	0.0526	0.1099	0.3500	0.1163	0.0279	0.2552	0.0335	0.1950	0.0232

Table 4.9: Pre-fault Power in MW and Voltage Angle Under Wind Penetration

Parameter	No Wind	Wind Farm at			
		Station 2	Station 3	Station 4	Station 5
θ_{12}	17.56°	17.52°	17.56°	17.49°	17.48°
θ_{23}	8.35°	8.44°	8.38°	8.42°	8.41°
θ_{43}	−3.94°	−4.06°	−3.94°	−4.17°	−4.11°
θ_{54}	12.58°	12.51°	12.57°	12.47°	12.46°
P_1	684.3	681.5	684	681.4	681
P_2	2100	1398	2100	2095	2094
P_3	1697	1693	998	1692	1697
P_4	1894	1890	1894	1192	1894
P_5	1658	1655	1658	1654	955.5

the frequency of the slow mode to 0.25 Hz from its nominal value (no line loss). Interestingly, however, the dominance of this 0.25 Hz mode is found to be uniform in all the phase angle differences, consistent with the observations in [49].

4.6.3 Wind penetration at pilot buses of WECC

Wind farms were placed on buses S_2 to S_5, one at a time, in the RSCAD model such that 700 MW of the power injection on that bus now came from wind penetration rather than the conventional synchronous machine. The ASG inertia was also altered by an equivalent amount to reflect the decommissioning of active machines in that area. The model was faulted by a 4-cycle line-to-ground fault, and the resulting transient responses of the bus angles were recorded. The pre-fault steady-state power and angle values for all buses are recorded in Table 4.9. The angles clearly indicate that when wind power is injected to a bus, the corresponding generation of the ASG steps down accordingly. The phase angle response across the four aggregated

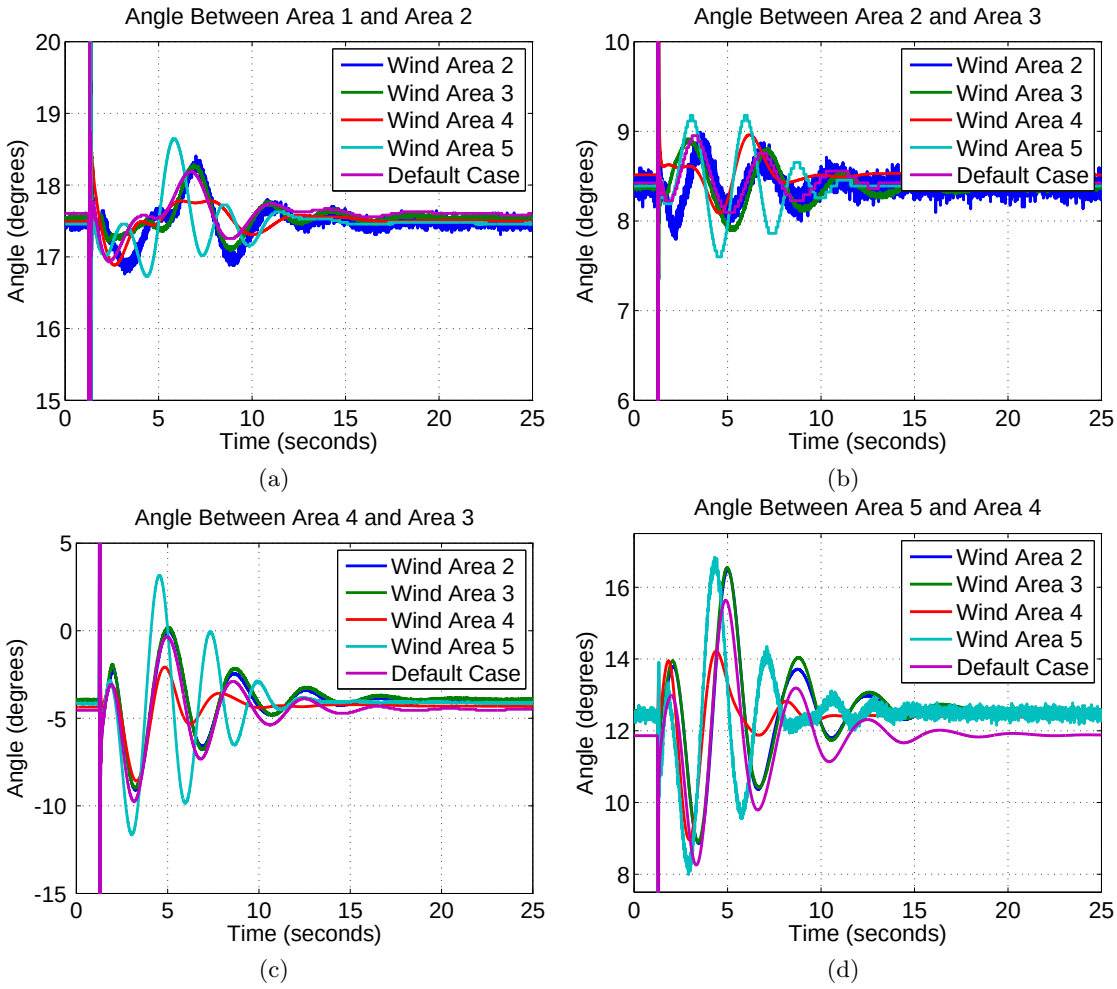

Figure 4.8: Effect of Wind Injection in Different Areas on Inter-area Oscillations

transmission lines are shown in fig. 4.8. The results from ERA applied to these plots are shown in Table 4.10, listing the oscillation modes with the highest energy for each wind penetration level. This reveals that, in general, increase in wind penetration in area 5 reduces the damping of the most energetic modes for all pair-wise angle differences. $\theta_5 - \theta_4$ is affected by wind penetration in all five areas, making pilot bus 5 the weakest point in the system. Wind in Area 5, however, favors damping in Area 4, i.e., the area closest to it.

Table 4.10: Modal Analysis of Power Flow with and without wind penetration

$\Delta\theta$	No Wind		Wind at S_2		Wind at S_3		Wind at S_4		Wind at S_5	
	Freq. (Hz)	Damp.	Freq. (Hz)	Damp.	Freq. (Hz)	Damp.	Freq. (Hz)	Damp.	Freq. (Hz)	Damp.
$\theta_1 - \theta_2$	0.1188	0.3520	0.1267	0.4923	0.2262	0.1620	0.1073	0.2677	0.3049	0.1703
$\theta_2 - \theta_3$	0.2635	0.6081	0.2248	0.5149	0.0866	0.9429	0.2416	0.3782	0.1339	0.7990
$\theta_4 - \theta_3$	0.2175	0.1706	0.2198	0.1777	0.2146	0.1858	0.2489	0.3046	0.1927	0.8725
$\theta_5 - \theta_4$	0.2166	0.1770	0.2174	0.1668	0.2147	0.1690	0.2610	0.3050	0.2772	0.2241

4.7 Conclusion and Future Work

In this chapter, we developed a predictive dynamic-equivalent model for the WECC power system using Synchrophasors. Modal decomposition followed by nonlinear least squares is used as the primary tool for this identification. The resulting model, after validation in RTDS, is found to be a beneficial resource for predicting frequency and damping of inter-area oscillations following small-signal disturbances, as well as transient stability limits due to large-signal contingencies such as loss of major lines and generators. The model also predicts the sensitivity of the power flow oscillations inside any area with respect to faults and wind power penetration in any other area. The use of the model, however, is not limited to only making decisions on specific lines and generators but also to create "monitoring metrics" that can be used for wide-area monitoring. For example, in [45] it was shown how PMU measurements can be used to construct inter-area energy functions for transient stability monitoring. The model in [45], however, was restricted to only two areas connected by a radial topology, and hence, there was no need to estimate the topology. The work done in this chapter is a useful extension by which such energy functions can be estimated for any multi-area power systems connected by any arbitrary topology.

The power system oscillations seen in figures 4.6, 4.7 and 4.8 can be damped more effectively using a FACTS controller. However, as the five-machine reduced-order model only conserves the identity of the pilot buses from the WECC 500 kV network, only shunt-connected FACTS devices can be used for power oscillation damping for this reduced-order model.

Chapter 5

Static Series Synchronous Compensator

5.1 Introduction

Power flow in large power systems is often dictated by network dynamics, individual generators within the network, and the load profile of that network. It is nearly impossible to control the power flow on a particular transmission line in the absence of any compensating device connected in series with that line, or in shunt at one of the terminals of that line. Several series and shunt compensation-based devices were discussed in the previous chapters, including the SVC, TCSC, STATCOM, SSSC, among others. This chapter will focus exclusively on the various applications of the SSSC in power networks. Chapter 3 included an introductory discussion of the two control algorithms for the SSSC and demonstrates its ability to control real power flow along a transmission line.

This chapter will explore an additional application for the SSSC, namely Ferranti effect mitigation. Another application of the SSSC, power oscillation damping, will be covered in the next chapter. This chapter will also discuss control algorithms for SSSCs based on the cascaded H-bridge converter (CHB) configuration as well as distributed series connected FACTS devices.

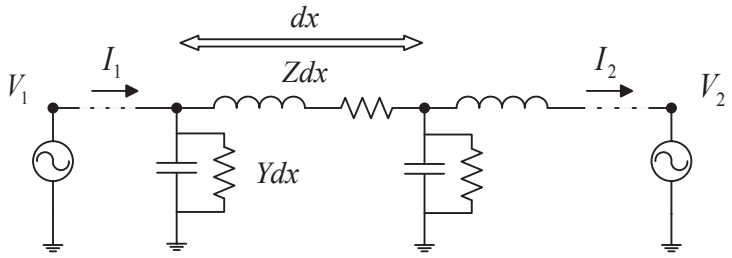

Figure 5.1: Exact model of a long transmission line showing the differential element of length dx

5.2 Ferranti effect mitigation

Ferranti effect is a phenomenon observed on long transmission lines which are energized from one end, while the other end is unloaded or lightly loaded. For a long transmission line shown in figure 5.1, the equations for voltages and currents at the sending end [50] are written as,

$$\begin{aligned} V_1 &= V_2 \cosh \gamma l + I_2 Z_c \sinh \gamma l \\ I_1 &= I_2 \cosh \gamma l + \frac{V_2}{Z_c} \sinh \gamma l \end{aligned} \tag{5.1}$$

The constants γ and Z_c in equation (5.1) are defined as $\gamma = \sqrt{YZ}$ and $Z_c = \sqrt{\frac{Z}{Y}}$, where $Z = R + jX$ and $Y = G + jB$ are the series impedance and shunt admittance of the transmission line per unit length. Z_c is referred to as the line characteristic impedance, and γ is the propagation constant.

Under no load conditions, $I_2 = 0$, and equation (5.1) reduces to

$$\begin{aligned} V_1 &= V_2 \cosh \gamma l \\ I_1 &= \frac{V_2}{Z_c} \sinh \gamma l \end{aligned} \tag{5.2}$$

In general, both γ and Z_c are complex numbers, however, if both R and G are approximated

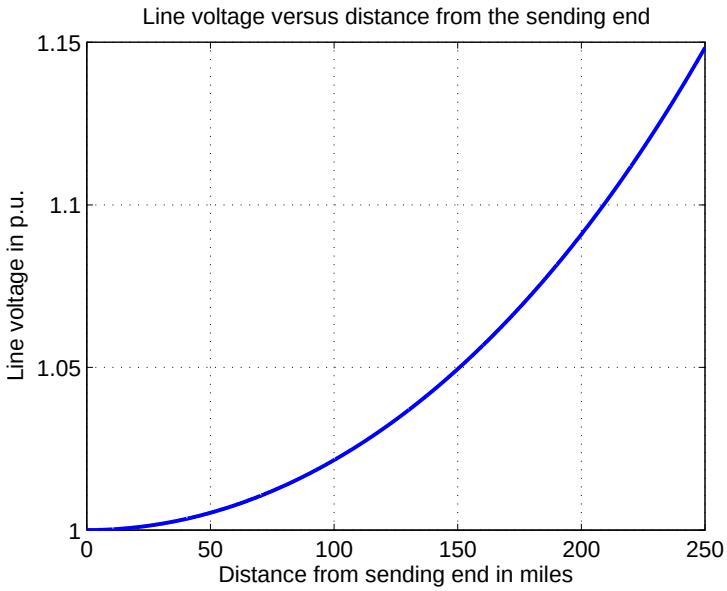

Figure 5.2: Line voltage in p.u. of an unloaded lossless line plotted as function of distance from sending end. Transmission line parameters: $L = 2.1955$ mH/mile, $C = 13.541$ nF/mile.

to be very small, $\gamma = j\sqrt{BX} = j\beta$ and $Z_c = \sqrt{\frac{X}{B}}$. Equation (5.2) gets simplified as,

$$V_2 = \frac{V_1}{\cos \beta l} \tag{5.3}$$

$$I_1 = j\frac{V_1}{Z_c} \tan \beta l \tag{5.4}$$

From equation (5.3), two conclusions can be made:

- Receiving end voltage V_2 is greater than the sending end voltage V_1, and

- Sending end line current leads the sending end voltage by 90°.

Figure 5.2 shows the variation of voltage on an unloaded transmission line. For extremely long transmission lines, it becomes impossible to maintain voltages within reasonable limits without some form of shunt compensation.

Since the SSSC can only inject a voltage that is nearly at quadrature with the line current, the SSSC finds a unique application in mitigating Ferranti effect. From equations (5.3) and

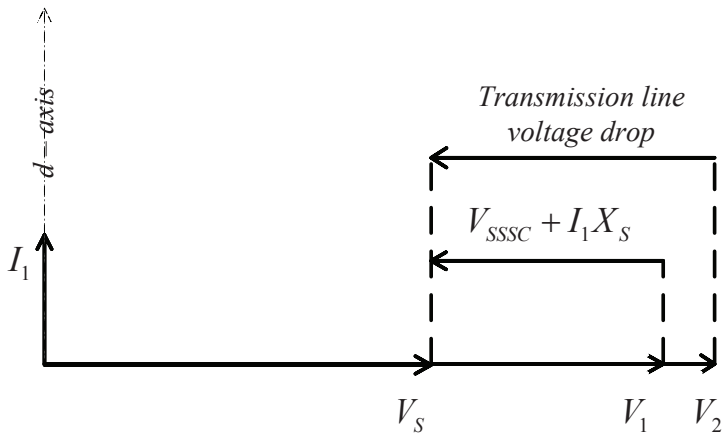

Figure 5.3: Phasor diagram showing SSSC operation with an unloaded transmission line

(5.4), it is clear that the line current under no load is also nearly at quadrature with the line voltage. Thus, if the SSSC injects a voltage under these conditions, that voltage will be in phase with the line voltage and can be used to either raise or lower the line voltage. The condition where a SSSC is used to lower the line voltage is demonstrated in the phasor diagram of Fig. 5.3. For simplicity, it is assumed that both R and G are very small. The SSSC reference $V^*_{1S_q}$ can be calculated using the identities in equations (5.3) and (5.4) as under:

$$\begin{aligned} V_{SSSC_q} &= V_2 - V_1 \\ &= -V_1 - j\frac{I_1 Z_c}{\sin \beta l} \\ \therefore\ V^*_{1S_q} &= -\left(|V_1| + \frac{I_1 Z_c}{\sin \beta l}\right) \end{aligned} \tag{5.5}$$

Both quantities V_1 and I_1 are known at the sending end and thus it is possible to estimate the receiving end voltage V_2 at the SSSC, provided that the transmission line characteristics Z_c and β are known. From Fig. 5.3, it is clear that the SSSC achieves the reduction in voltage magnitude at the receiving end by depressing the voltage magnitude V_S by an equal amount. Usually no other equipment is connected on the transmission line side of the SSSC and reducing V_S should not affect system operation. However, in certain situations it may be necessary to

Table 5.1: Transmission line parameters

Line Parameter	**Value**
Line length	250 km
Phase conductors	3
Phase conductor arrangement	Horizontal, equal spacing
Phase conductor spacing	10 meters
Phase conductor elevation	30 meters
Phase conductor type	Chukar, ACSR
Ground conductors	2
Ground conductor arrangement	Horizontal, equal spacing
Ground conductor spacing	10 meters
Ground conductor elevation	40 meters
Ground conductor type	0.5" high-strength steel
Ground resistivity	100 Ω-m

define a different set-point than the one defined in equation (5.5).

Voltage control in large power networks is usually performed with shunt devices located at or near the bus where the voltage magnitude needs to be controlled. The simplest shunt compensating device is the switched parallel inductor and capacitor banks which are connected to the voltage-controlled bus. Shunt connected devices like the Static VAR Compensator (SVC) and the Static Synchronous Compensator (STATCOM) are the most common FACTS devices used for voltage regulation at a given bus [2, 51] and would be more economical than SSSCs in mitigating Ferranti effect.

However, it also must be noted that the primary function of the SSSC is in real power flow control along the transmission line, as discussed in section 5.1. The decision of installing a SSSC on a transmission line is typically motivated by the flexibility in power flow control it provides within the power system. Ferranti effect mitigation is an ancillary function that the SSSC can perform when the long transmission line becomes unloaded due to some contingency. The SSSC would perform this function during the short periods of time when it actually cannot perform real power flow, making it a perfect complementary function. Further, it must also be noted that the proposed SSSC controller can perform voltage control under unloaded conditions from a remote energized bus, as opposed to other shunt devices which are required to be physically

Table 5.2: SSSC parameters

VSC Parameters	**Value**
No. of switches	6
Type of switch	SiC MOSFET with anti-parallel SiC diode
DC bus voltage	12000 V
DC bus capacitor	4700 μF
Transformer Parameters	**Value**
Transformer rating	6 MVA
VSC side winding rating	4 kV
Line side winding rating	16 kV
Leakage reactance	0.02 p.u.

located at the bus to be regulated.

5.2.1 Results

The simulation was performed on PSCAD on a 230 kV system with a three-phase transmission line connected between two buses. One end of the transmission line is energized (referred to as the 'source side'), while the other end is left open. The transmission line is considered to be ideally transposed for the purpose of the simulation and is modeled as per the Frequency Dependent model in PSCAD. Table 5.1 lists the transmission line parameters in detail.

The SSSC is connected at the source side of the line through a three-ϕ transformer, whose high voltage windings are connected in series with the transmission line, while the low voltage windings are connected in a star configuration before being connected to the VSC. Table 5.2 lists the SSSC parameters in detail. The converter can be built using 15 kV Silicon Carbide based power MOSFETs (SiC Metal-Oxide-Semiconductor Field-Effect-Transistor) to block 12 kV DC voltage at a switching frequency of 1 kHz while maintaining a reasonably high efficiency per switch [52]. The transmission line requires about 10 - 13 kV AC compensation to set the voltage to 1 p.u. Based on the series transformer's turns ratio, the VSC is required to generate about 3.25 kV rms at its terminals, i.e. 4.6 kV peak. For a three-phase, two-level, three-arm VSC bridge, the peak AC voltage V_m produced by the VSC is limited to $V_{dc}/2$, in order to

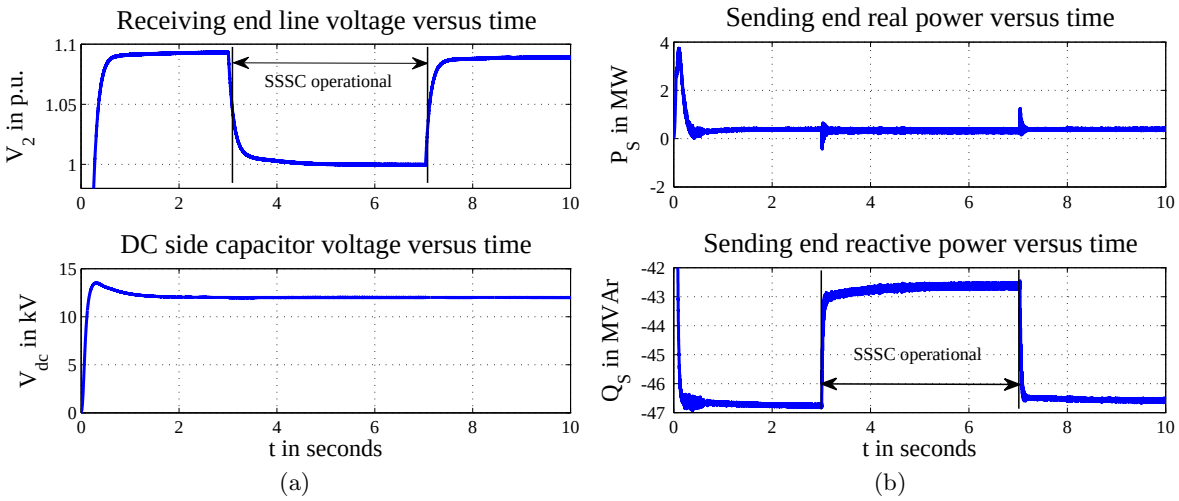

Figure 5.4: Plots of receiving end voltage, SSSC DC voltage, and sending end real and reactive power during SSSC compensation

avoid over-modulation. In this case, the minimum V_{dc} required works out to about 9.2 kV [53], which is rounded up to 12 kV.

The transmission line is operated at no-load, and due to Ferranti effect, the RMS receiving end voltage rises to about 1.09 p.u. At t = 3 s, the SSSC controls are turned on and the receiving end terminal voltage drops to 1 p.u. as seen in Fig. 5.4a. The DC bus voltage remains constant during the SSSC operation indicating that the average real power exchanged by the converter is zero, barring any losses in the switches. Fig. 5.4b shows the real and reactive power flowing into the transmission line from the source. The real power is nearly zero and it compensates for the resistive losses in the transmission line, except for the initial transient when the SSSC DC capacitor gets charged. The transmission line draws capacitive reactive power from the source, which gets reduced by about 3.8 MVAr when the SSSC is operating to reduce over-voltage at the receiving end.

The performance of the SSSC in mitigating Ferranti effect was tested under lightly-loaded conditions for two cases: a 75 MW resistive load, and a 75 MVAR inductive load connected to the far end of the transmission line. The capacitive load case is not considered for analysis, as

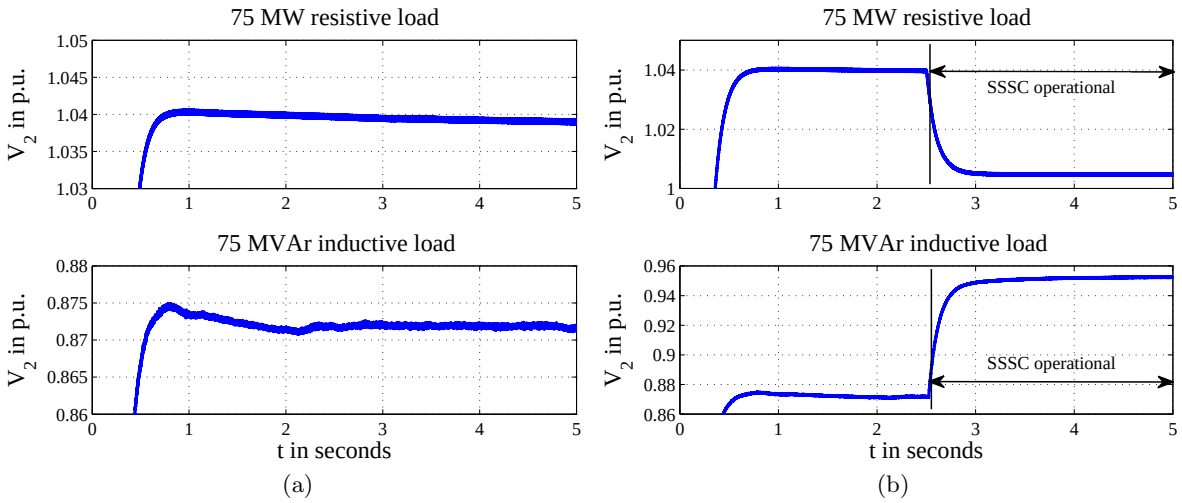

Figure 5.5: Plots of receiving end voltage V_2 for 75 MW resistive and 75 MVAr inductive loads, without and with SSSC compensation

it would only worsen the over-voltage and it would only be an extension of the case discussed in Fig. 5.4. The receiving end voltage V_2 for the two load cases are plotted in Fig. 5.5a. The control law defined in equation (5.5) is not applicable for lightly-loaded conditions, and thus the SSSC was used for series voltage injection with a direct command $V^*_{1S_q}$. Fig. 5.5b shows the performance of the SSSC for the two cases, and it is clear that the MVA rating of the SSSC is not adequate for bringing V_2 to 1 p.u. for both cases. However, the SSSC manages to keep the voltage within 1±0.05 p.u. with the SSSC operating at its peak voltage output. It is also apparent that the SSSC is more effective at compensating inductive loads than resistive loads.

5.2.2 Conclusion

In this section, we demonstrated a new application of the SSSC, which is a VSC based FACTS device connected in series with the transmission line. The SSSC can be used to mitigate Ferranti effect which manifests on unloaded and lightly loaded transmission lines. In order to do so, minor changes in the existing SSSC control loop are required, which involves changing the output voltage set-point calculation to the one as per Eq. (5.5). The system was simulated

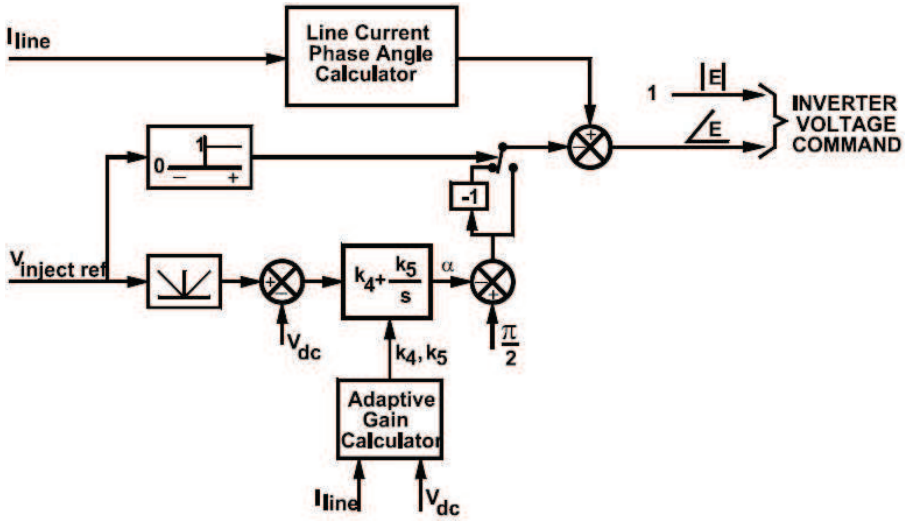

Figure 5.6: Type-II angle control for New York Power Authority's Convertible Static Compensator operating in SSSC mode [54]

in PSCAD and the SSSC control was able to reduce the over-voltage at the receiving end. It was also observed that the reactive power requirement of the transmission line reduced when the SSSC was in operation. It was also noted that the SSSC can produce a similar effect when the line is lightly loaded with inductive and resistive loads. It was observed that the SSSC was more effective at compensating for inductive loads than resistive loads. Future studies will investigate into the application of series connected distributed FACTS devices for performing a similar function.

5.3 Cascaded H-bridge converters

The VSCs currently installed within transmission networks are either based on Si-based Gate Turn-off thyristors (GTOs), Integrated Gate Commutated Thyristors (IGCTs) or Integrated Gate Bipolar Transistors (IGBTs) [55, 56]. GTOs typically have low conduction losses at the transmission level, but have poor performance at high switching frequencies. Thus, the VSCs based on GTOs are switched at line frequencies and type-II control [10] is used to control these VSCs. Line frequency switching has the disadvantage that the switching harmonics are

placed very close to the line frequency and this leads to expensive filter design. To counter this, GTO-based VSCs are often designed as multilevel converters where the voltage output of several converters is vectorially added to get a higher pulse level. An example of this is the New York Power Authority's Convertible Static Compensator (CSC) [36, 54, 57], which consists of two 100 MVA 48-pulse VSCs and it that uses GTOs switched at line frequency. The lowest harmonic frequency the grid sees due to this configuration is the 95^{th} harmonic $(2p-1)$ at a base frequency of 60 Hz, which corresponds to 5.7 kHz. Thus, the increase in pulse level reduces the filter size and cost tremendously, but it increases the project costs by adding a complicated multi-winding transformer which vectorially adds the voltage output from the individual converters. This transformer is usually in addition to a second step-up transformer which interfaces the converter side to the grid.

The requirement for type-II control is another disadvantage since this control is essentially nonlinear. This is evident in figure 5.6 which shows the type-II controller for a SSSC [54]. The two control loops of type-I control, V_q AC voltage injection, and DC bus voltage control, are conflated together in one control loop, and the PI controller is used to control the angle of the voltage injection being made by the converter. This leads to the non-linearity in control, which makes the controller design quite sensitive to the operating point and is somewhat undesirable. In spite of these disadvantages, GTO-based VSCs are quite popular at the transmission level since they are a well-proven commercialized technology.

IGCTs and IGBTs on the other hand can be switched at higher frequencies of around 500 Hz - 1 kHz, which helps in reducing filter design costs and size. This also eliminates the need for a special multi-winding transformer which vectorially adds the voltage outputs of multiple converters. Also, the VSCs that use the IGBTs and the IGCTs can be controlled using type-I control [10], which is an advantage due to the linearity of this control scheme.

Commercially available IGBTs and IGCTs are rated around 4.5 - 6 kV, which is considered to be in the medium voltage range. Several of these switches would be needed to be connected in series to sustain the transmission level voltages which are all greater than 132 kV. Although

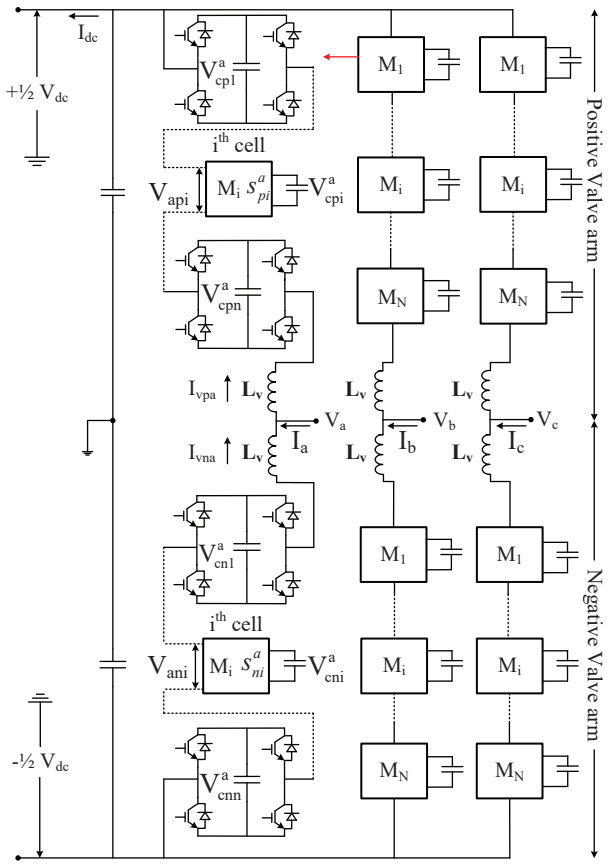

Figure 5.7: A $3-\phi$ Double-star modular multilevel converter with full-bridge cells

this is possible, there is a better way to utilize the same number of switches while interfacing the converter to the transmission network. The family of converter topologies which does this is called as the modular multilevel converter (MMC) topology.

The MMC topology was first proposed in 2005 [58] and its variants and its applications have been covered extensively in literature [59, 60, 61, 62, 63]. MMCs are characterized by multiple single-phase full-bridge or half-bridge converter blocks connected in series in each leg of the converter. The individual converter blocks are termed as "cells". MMCs can have multiple legs per phase, and they are classified as single-star, double-star, etc depending on the number of legs per phase [59]. The Cascaded H-Bridge (CHB) converter is a special case of the MMC topology with full-bridge cells in single-star configuration. CHB converters find applications

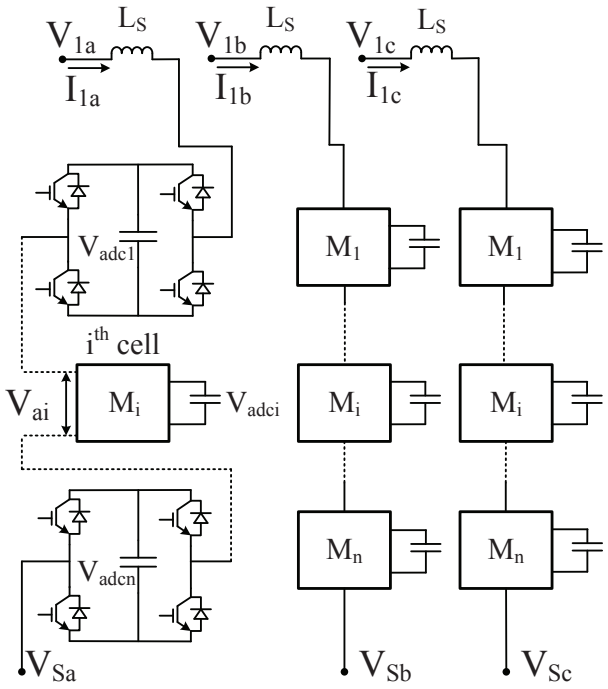

Figure 5.8: Circuit diagram for a $3-\phi$ Cascaded H-bridge converter with n cells per phase

where a common DC link between the all the individual converter cells is not essential, like in the case of a STATCOM or a SSSC [62, 64]. In case of the UPFC or HVDC converters, the double-star configuration as shown in Figure 5.7 is more suitable.

Fig. 5.8 shows the detailed block diagram of the CHB converter with n cells per phase. By appropriately selecting n, the CHB converter can eliminate the complicated $3-\phi$ multi-winding transformer that cancels harmonics in conventional multilevel converters like the Neutral Point Clamped (NPC) converters. Further, CHB converters can provide a near sinusoidal output with low total harmonic distortion (THD) even with low frequency carrier waves [65], if the phase-shifted multi-carrier modulation technique is used.

However, it has been observed that the DC capacitor voltage of the individual cells is unstable and can easily drift away from the mean DC voltage value across each phase. The average DC voltage per phase also can drift away from the DC voltage reference, while the overall average DC voltage can remain regulated. In order to correct this, several control algorithms

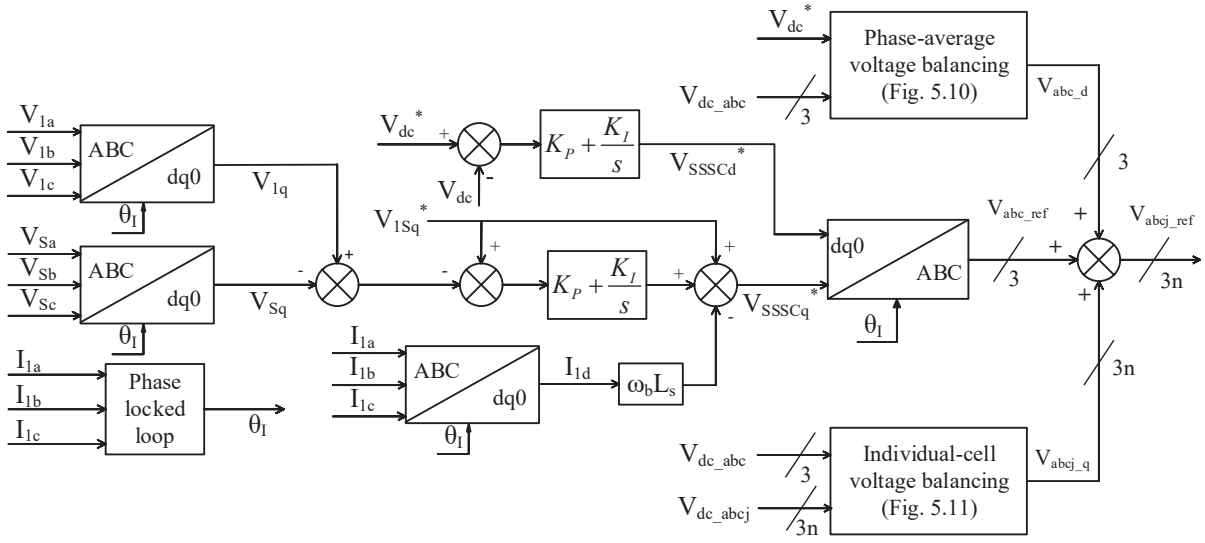

Figure 5.9: Control block diagram for a PWM-based two-level SSSC.

that perform DC capacitor voltage balancing for the individual cells have been proposed in literature [62, 61, 66, 67, 68]. However most of these algorithms are specific to CHB converters operated in shunt with the power system, like a STATCOM or in a back-to-back configuration. There has been no investigation into the application of CHB converters as a series-connected device like the SSSC. The design of the series-connected transformer which interfaces a SSSC with the transmission line is even more complicated than the one required for STATCOM, and thus, substantial savings can be made if this transformer is eliminated from SSSC design.

In this section, I developed controllers to counteract the capacitor voltage imbalance for the CHB-based SSSC. I also implemented the CHB-based SSSC in PSCAD and RTDS.

5.3.1 Basic Control of SSSC

Fig. 5.9 shows the control block diagram of the SSSC which includes the DC voltage regulation loop and the line current regulation loop. A synchronously-rotating $dq0$ reference frame with its d-axis aligned with the transmission line current is used for controller design. The

transformation is defined as $f_{dq0} = \boldsymbol{T} f_{abc}$ where T is defined as

$$\boldsymbol{T} = \frac{2}{3}\begin{bmatrix} \cos\theta & \cos(\theta - \frac{2\pi}{3}) & \cos(\theta + \frac{2\pi}{3}) \\ -\sin\theta & -\sin(\theta - \frac{2\pi}{3}) & -\sin(\theta + \frac{2\pi}{3}) \\ \frac{1}{2} & \frac{1}{2} & \frac{1}{2} \end{bmatrix} \tag{5.6}$$

As seen in Figure 5.9, the angle $\theta = \theta_I$ is obtained from a phase-locked loop (PLL) aligned with the a-phase transmission line current, I_{1a}. This choice simplifies the controller design substantially as $I_{1q} = 0$. The dq reference voltages for the SSSC are then generated as

$$V^*_{SSSC_d} = \left(K_P + \frac{K_I}{s}\right)(V^*_{dc} - V_{dc}) \tag{5.7}$$

$$V^*_{SSSC_q} = \left(K_P + \frac{K_I}{s}\right)\left[V^*_{1S_q} - \left(V_{1_q} - V_{S_q}\right)\right] + V^*_{1S_q} - \omega_b L_S I_{1d} \tag{5.8}$$

V^*_{dc} is the DC voltage reference for the DC-side capacitor on each cell, and V_{dc} is the average DC capacitor voltage across all cells and phases. V_{1_q} and V_{S_q} are the $q-$axis components of V_1 and V_S respectively. I_{1d} is the $d-$axis component of transmission line current I_1. ω_b is the base angular frequency of the phasors in rad/s, corresponding to a line frequency of 60 Hz in this case. L_S is the leakage inductance of the series transformer, or the effective series inductance of the L-C-L filter. The reference $V^*_{1S_q}$ in Equation (5.8) calculated depending on the control objective of the SSSC. For example if the SSSC is required to insert a capacitive reactance X^*_q in series with the line, $V^*_{1S_q} = I_{1d} X^*_q$ is the control input. In case of real power flow control, $V^*_{1S_q}$ can be generated from the real power command P^*_l as

$$V^*_{1S_q} = \left[K_{pP} + \frac{K_{iP}}{s}\right](P^*_l - P_l) \tag{5.9}$$

where P_l is the measured value of real power flow along the transmission line. The power flow control loop is very slow in the order of a few seconds and hence PI tuning is not an issue.

SSSCs typically inject less than 10% of the transmission line voltage in series with the line.

5.3.2 Capacitor Voltage Balancing

Before beginning a discussion on the capacitor voltage balancing algorithm, the nomenclature used in this paper needs a description. The DC side capacitor voltage of the j^{th} H-bridge cell in the i^{th} phase is denoted as V_{dcij}, where $j \in [1, n]$, $i \in \{a, b, c\}$, and n is the cascade number. The average DC capacitor voltage for all cells in the i^{th} phase is given as

$$V_{dci} = \frac{1}{n} \sum_{j=1}^{n} V_{dcij} \tag{5.10}$$

Finally, the average DC capacitor voltage across all cells and phases is calculated as

$$V_{dc} = \frac{V_{dca} + V_{dcb} + V_{dcc}}{3} \tag{5.11}$$

The control block diagram described in Fig. 5.9 uses a synchronous dq reference frame aligned with the transmission line current, which simplifies the SSSC controls. However, this reference frame is not helpful for designing the capacitor voltage balancing algorithm, and a different synchronous reference frame aligned with the sending-end voltage is considered. This voltage can easily be measured using potential transformers connected at the bus closest to the SSSC. The angle $\theta = \theta_v$ is obtained from a PLL aligned with phase-a of the sending-end phase voltage thus measured. Finally, the voltage balancing is attained in two steps:

A. Phase-average voltage balancing

B. Individual cell voltage balancing

Phase-Average Voltage Balancing

The purpose of this algorithm is to move the average DC capacitor voltage for all cells in the i^{th} phase, V_{dci} closer to the DC voltage reference V_{dc}^{*}. This is accomplished by making all the

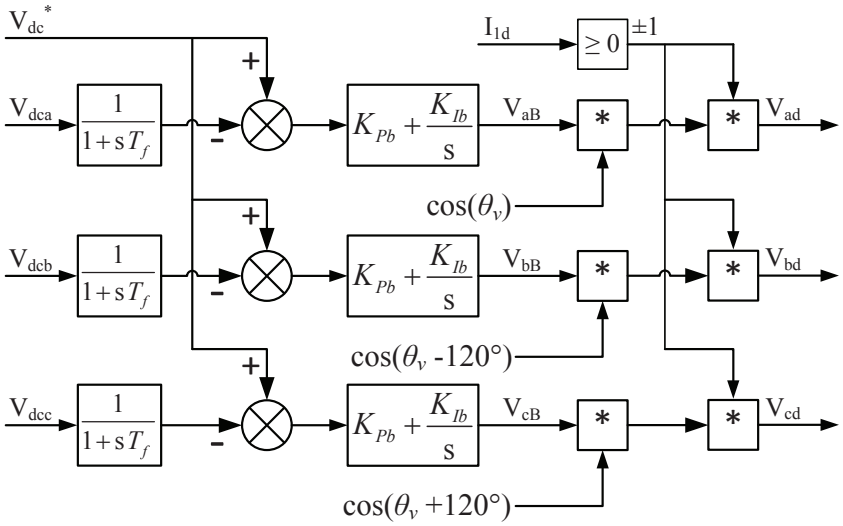

Figure 5.10: Control block diagram for the phase-average voltage balancing algorithm.

cells in the i^{th} phase inject a voltage in phase with the d-axis transmission line current. The peak voltage to be injected by each cell in the i^{th} phase as

$$V_{iB} = \left(K_{Pb} + \frac{K_{Ib}}{s}\right)\left[V_{dc}^{*} - \frac{V_{dci}}{1 + sT_f}\right] \tag{5.12}$$

The PI control gains K_{Pb} and K_{Ib} are kept same in all phases because each phase will have a different transient response if those constants were to be different. Such a response would be undesirable, and different injections across the phases is also not necessary as there is little phase-wise voltage imbalance in transmission. The actual injected voltage is obtained by aligning the voltages obtained in Eq. (5.12) with the d-axis transmission line current. Upon calculating $\boldsymbol{T}^{-1}$ from Eq. (2.6), it can be shown that the quantities V_{aB}, V_{bB}, and V_{cB} need to be multiplied with $\cos\theta_v$, $\cos(\theta_v - 120^\circ)$, and $\cos(\theta_v + 120^\circ)$ respectively. By doing so, the i^{th} phase of the converter exchanges real power with the d-axis current in order to charge or discharge the DC capacitors in that phase. Finally, the voltage command is multiplied with ± 1 depending upon the direction of the d-axis transmission line current, in order to obtain V_{id}.

The voltage V_{dci} contains second harmonic oscillations of the fundamental line frequency

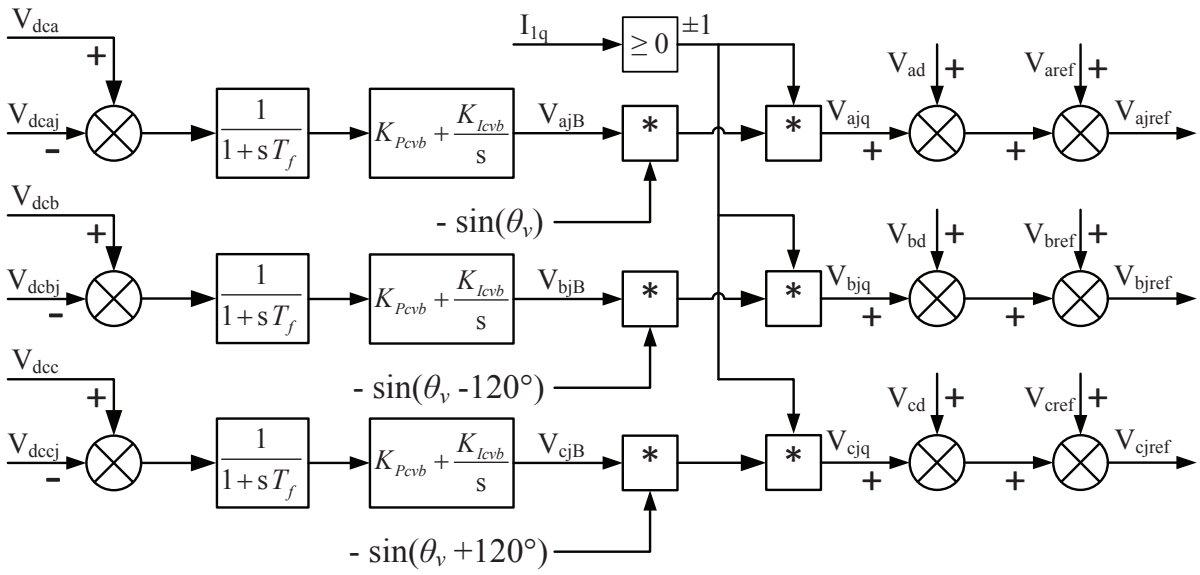

Figure 5.11: Control block diagram for the individual cell voltage balancing algorithm.

which are removed in the control algorithm by adding a low-pass filter with time constant T_f. T_f is determined by selecting a suitable cut-off frequency that removes the second harmonic component, which in this case was 120 Hz. The control block diagram for the balancing algorithm described in this subsection is shown in Fig. 5.10.

Individual Cell Voltage Balancing

The previous subsection details an algorithm to move the phase-wise average DC capacitor voltages closer to the DC voltage reference. This subsection details a control loop which moves the DC capacitor voltages of the individual H-bridge cells, V_{dcij} closer to V_{dci}. This is achieved by making the H-bridge cells exchange real power with the q-axis transmission line current, which is similar to the control algorithm proposed in [62] for balancing DC voltages in individual cells. As in the previous section, the DC capacitor voltages are filtered using a low-pass filter to remove the second harmonic oscillatory component. The peak voltage to be injected by the

Table 5.3: Transmission line parameters

Line Parameter	**Value**
Line length	200 km
Phase conductors	3
Phase conductor arrangement	Horizontal, equal spacing
Phase conductor spacing	10 meters
Phase conductor elevation	30 meters
Phase conductor type	Chukar, ACSR
Ground conductors	2
Ground conductor arrangement	Horizontal, equal spacing
Ground conductor spacing	10 meters
Ground conductor elevation	40 meters
Ground conductor type	0.5" high-strength steel
Ground resistivity	100 Ω-m

individual cells is obtained as

$$V_{ijB} = \left(K_{Pcvb} + \frac{K_{Icvb}}{s}\right)\left[V_{dci} - \frac{V_{dcij}}{1 + sT_f}\right] \tag{5.13}$$

V_{ajB}, V_{bjB} and V_{cjB} thus obtained are multiplied with $-\sin\theta_v$, $-\sin(\theta_v - 120^\circ)$, and $-\sin(\theta_v + 120^\circ)$ respectively to align the voltage injections with the q-axis line current. The voltage command is also multiplied with ± 1 depending upon the direction of the q-axis transmission line current. The resultant signal V_{ijq} is added to V_{id} from subsection 5.3.2 and V_{iref} from the basic SSSC control to obtain V_{ijref} which is the reference voltage wave for the j^{th} cell in the i^{th} phase. The complete control block diagram for individual cell voltage balancing can be seen in Fig. 5.11.

The voltage references V_{ijref} for each cell are normalized with respect to V_{dc}^* and the normalized reference is compared with a phase-shifted triangular waveform at $f_s = 1$ kHz to obtain pulses for the four switches in each cell using uni-polar modulation [65].

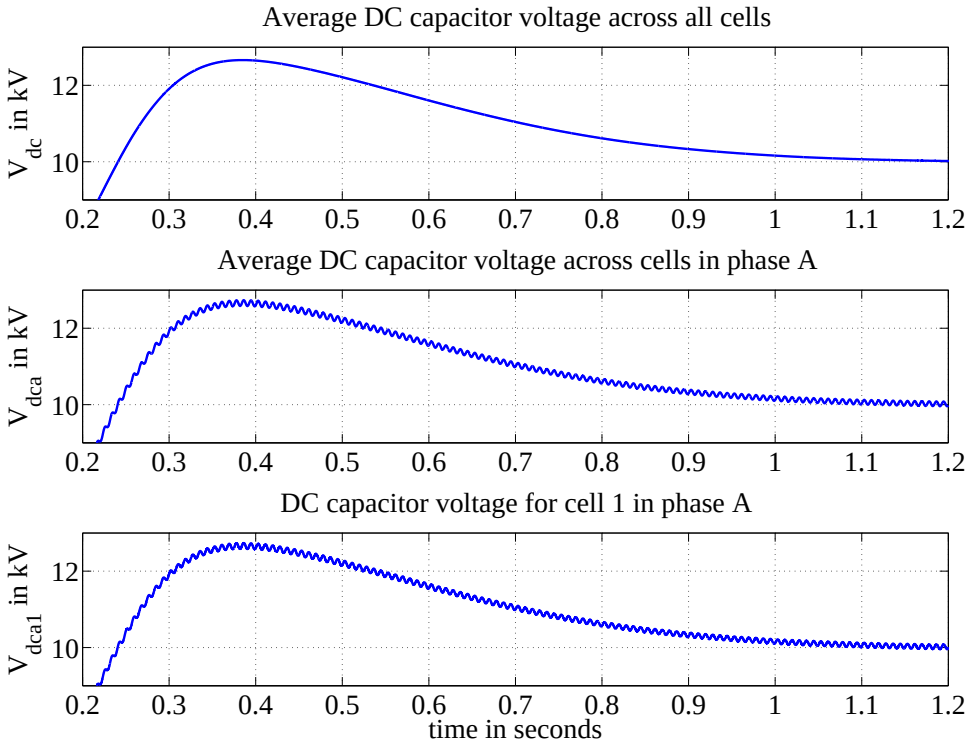

Figure 5.12: Plots of V_{dc}, V_{dca} and V_{dca1} for a voltage command $V^*_{1Sq} = -36.5$ kV

5.3.3 System description

The CHB-based SSSC was implemented in a two bus 230 kV power system in PSCAD with a 200 km long transmission line, the details of which are listed in Table 5.3. The transmission line is considered to be ideally transposed for the purpose of the simulation and is modeled as per the Frequency Dependent model in PSCAD. The receiving end source V_2 lags V_1 by 10°, which establishes a base power flow of 78.0 MW in the circuit from bus 1 to bus 2.

The CHB converter considered in the simulation has five H-bridge cells per phase connected in series, with the DC bus for each cell set at 10 kV. The CHB converter is also connected in series with an L-C-L filter which has a 3 dB cut-off frequency of 150 Hz and is located between the converter and bus 1. It is usual to consider a filter with 10 % series inductance. For a base voltage of 230 kV and base apparent power of 100 MVA, the total series inductance works out to be 0.15 H. The converter side inductance L_2 is set to 0.1 H, whereas the grid side inductance

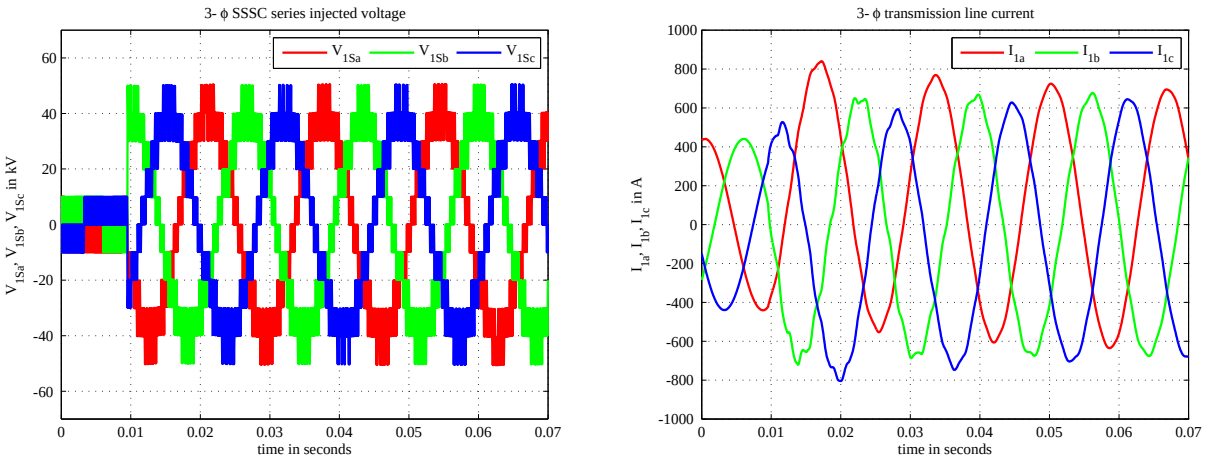

Figure 5.13: Plots of V_{1Sabc} & I_{1abc} for a voltage command $V^*_{1Sq} = -40$ kV at $t = 0.01$ s

L_1 is set to 0.05 H, considering an L_2/L_1 ratio of 2. Based on these values, the filter capacitance is set to 33.77 μF. It was observed that the filter reduces the total harmonic distortion (THD) in the transmission line current from about 1 % to under 0.30 %. It must be noted that the THD is already lower than the levels prescribed in IEEE 519 [69], which is primarily due to two reasons:

1. The CHB converter is using phase-shifted PWM which makes the effective switching frequency $2nf_s$

2. The transmission line series inductance also acts as an effective filter

Nonetheless, an L-C-L filter is considered in the design which may be necessary under inclement conditions.

5.3.4 PSCAD Results

The CHB-based SSSC was simulated in PSCAD along with the power system described in section 5.3.3, and the performance of the SSSC in controlling real power flow along the transmission line was recorded. Fig. 5.12 shows the performance of the capacitor voltage balancing controllers as they charge the capacitors from zero to 10 kV, with plots of V_{dc}, V_{dca} and V_{dca1}

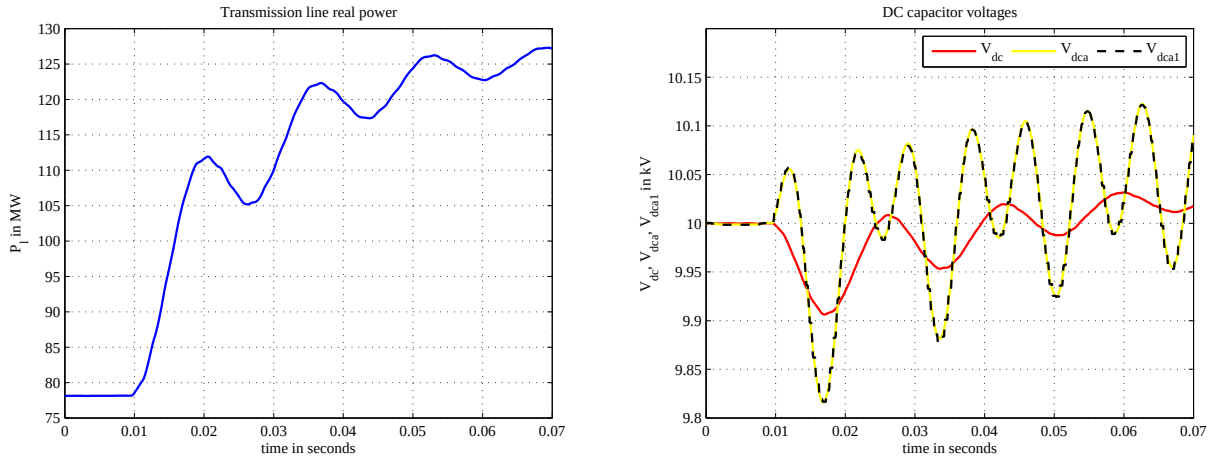

Figure 5.14: Plots of P_l & V_{dc}, V_{dca}, V_{dca1} for a voltage command $V^*_{1Sq} = -40$ kV at $t = 0.01$ s

versus time for a voltage step command of $V^*_{1Sq} = -36.5$ kV on the SSSC. The SSSC was intentionally given this command in order to enhance the 120 Hz harmonic in V_{dca} and V_{dca1} seen in Fig. 5.12. It can be seen that the capacitor voltage balancing controllers maintain V_{dca} and V_{dca1} within tight limits of V_{dc} as the basic DC bus voltage controller moves V_{dc} towards V^*_{dc}.

Figs. 5.13 and 5.14 show the performance of the CHB-based SSSC when a voltage step command of $V^*_{1Sq} = -40$ kV is given at $t = 0.01$ seconds. Upon receiving this command, the SSSC injects a 3-ϕ voltage in series with the transmission line which lags the line current by almost 90°. This reduces the transmission line inductive voltage drop, which causes the transmission line currents to increase, as shown in Fig. 5.13. The voltage command causes P_l to increase from the baseline 78 MW to 125 MW as seen in Fig. 5.14. The transients in V_{dc}, V_{dca} and V_{dca1} due to the voltage step command are also plotted in Fig. 5.14. The controller was designed with a settling time under 0.1 seconds and a peak overshoot of $\leq 5\%$, and the designed controller satisfied the requirements of the settling time with a resultant peak overshoot of 1.3%.

Fig. 5.15 shows the performance of the SSSC when a positive voltage command of $V^*_{1Sq} =$ 26.3 kV was given at $t = 0.1$ seconds, which effectively reduces P_l to 50 MW. As compared

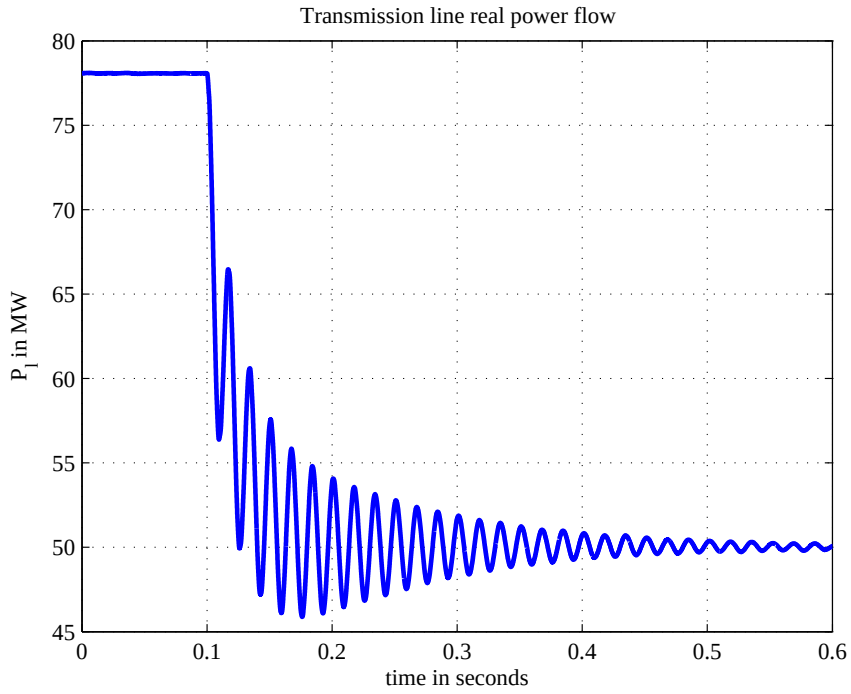

Figure 5.15: Plot of P_l for a voltage command $V^*_{1Sq} = 26.3$ kV at $t = 0.1$ s

to Fig. 5.14, the plot shows substantial ringing in the real power flow which is due to the transmission line approaching its power system stability limit. Further, upon increasing the V^*_{1Sq} command even further to 36 kV, sustained oscillations in P_l were observed. The system went unstable when V^*_{1Sq} was increased beyond 37 kV in order to reduce P_l under 40 MW.

The system was then simulated to observe the performance of the CHB-based SSSC in the power flow control mode. An additional control loop as described in Eq. (5.9) was implemented which gives a voltage reference to the inner loops. Two different cases were simulated. The first case involved giving a step change of 110 MW to the real power reference, followed by a step change down to 78 MW and further down to 50 MW. The performance of the controller for this reference change can be seen in figure 5.16. The performance of the power flow controller is more damped than the open-loop voltage injection seen in figures 5.14 and 5.15. This is more desirable in the case of closed-loop power flow control.

The second case involved the CHB-based SSSC tracking a trapezoidal real power reference

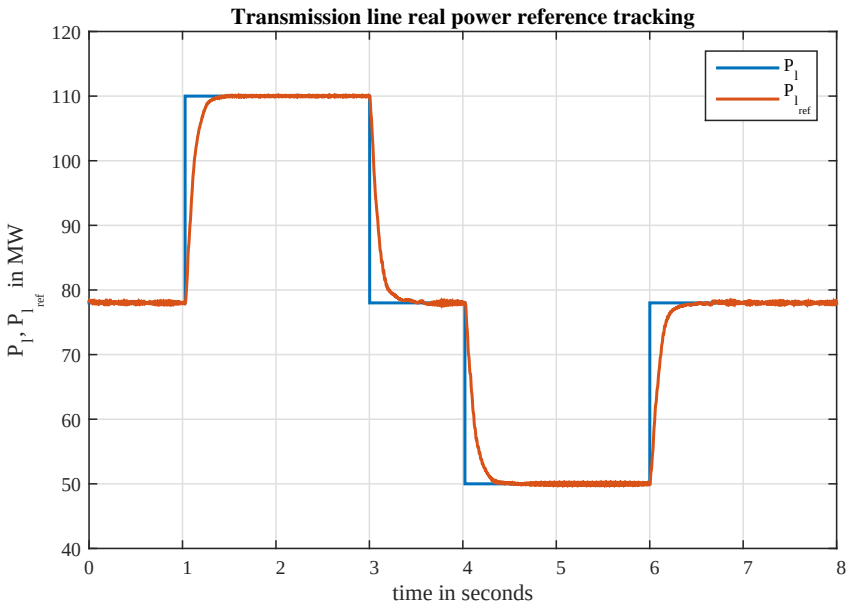

Figure 5.16: Plot of P_l tracking a staircase $P_{l_{ref}}$ command between 50 and 110 MW

as seen in figure 5.17. The trapezoidal reference varies between 48 MW and 108 MW with a ramp rate of ±30 MW/s between the steady state values. Performance of the controller in regulating power flow can be seen in figure 5.17. The controller has a steady-state error on the ramp as the PI controller behaves like a type-I system. The steady-state error is zero for the flat parts of the reference as expected. Figure 5.17 also shows the variation of reactive power Q_l at the sending end. It is observed that Q_l also follows a trapezoidal trajectory with a shape similar to that of the real power, but it is not a controllable variable.

5.3.5 RTDS Results

The CHB-based SSSC was also simulated in a real-time environment with the Real-Time Digital Simulator (RTDS). The AC system data was kept identical to the PSCAD case, but the converter size and rating was changed to a different value in order to optimize the simulation based on the capacity of the RTDS cards at the FREEDM Center. The number of H-bridges were reduced to 3 per phase, and each phase was simulated on a different processor using the

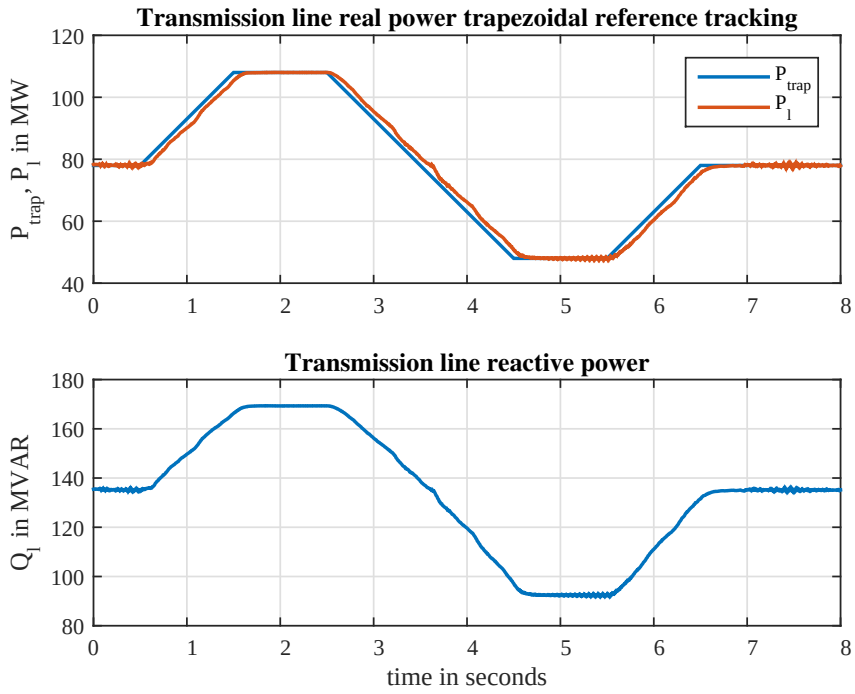

Figure 5.17: Plot of P_l tracking a trapezoidal P_{trap} reference, and Q_l

small-dt blocks. The small time-step side was simulated at a time step of 2.5 μs. The converters were interfaced to the transmission line with three single-phase series transformers, which also served the dual purpose of interfacing the 'small time-step' side with the 'large time-step' side of the simulation. The transformer rating can be seen in table 5.4. The DC bus voltage magnitude is maintained at 10 kV. An L-C-L filter was designed with $L_1 = 0.05$ H, $L_2 = 0.1$ H, and the filter capacitor $C = 6$ μF, with a design corner frequency of 360 Hz.

The converters on phase A were connected directly with the 'large time-step' side, whereas the other phases were processed on their separate processor that was connected to the phase A processor with optical fibers on the back-plane of the RTDS cards, as seen in figure 5.18. This was done so that the cards can communicate with each other at 'small time-step' speeds. However, doing so still results in some communication delays, and these delays between the processors were represented by a two-conductor, one kilometer long transmission line in the simulation. The construction details of this line can be seen in table 5.4. The same line was

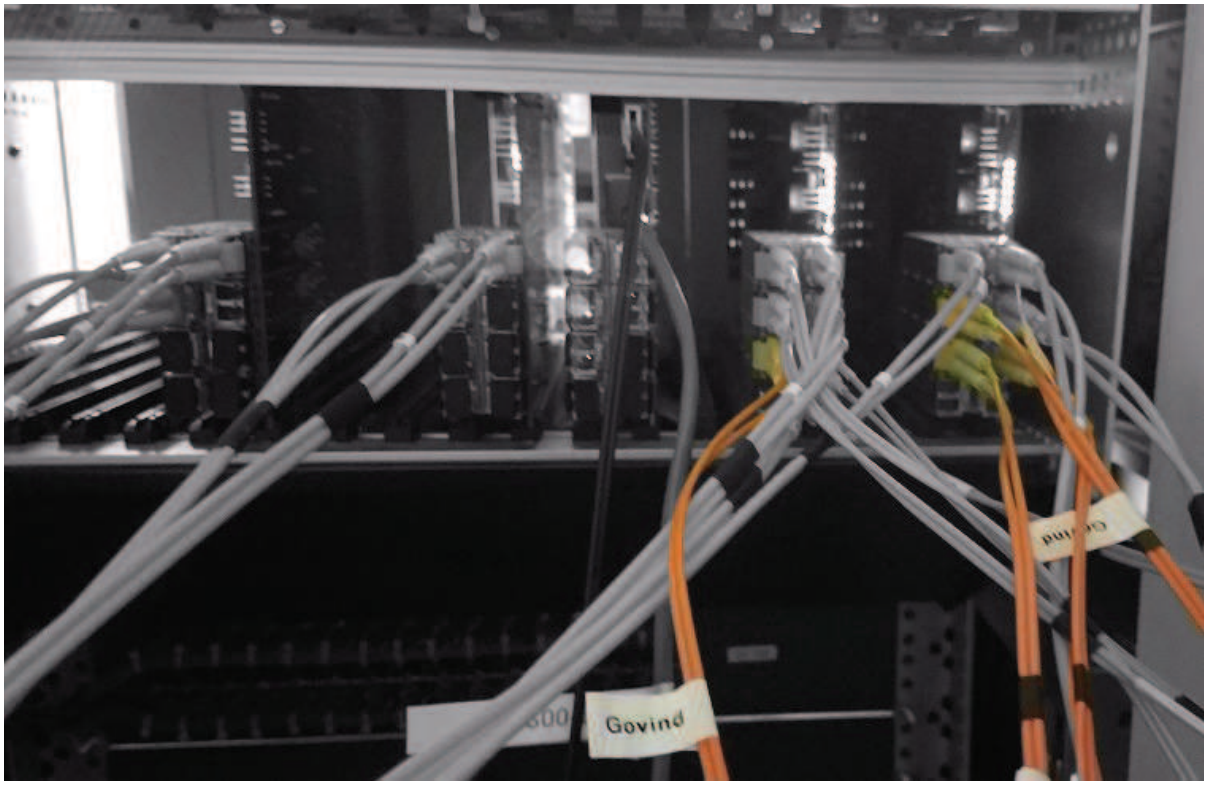

Figure 5.18: Back-plane interconnection between RTDS cards for 'small-dt' communication using optical fibers

also included in phase A of the converter to equalize the impedance in all three phases, even though the line was not required in the A-phase.

Figure 5.19 shows the performance of the CHB-based SSSC as implemented in RTDS. The transmission line under investigation is set up in such a way that there is a voltage angle difference of 25° across it. This establishes a power flow of 135 MW along the transmission line near the SSSC. A q-axis voltage command of $V_{1Sq} = -20$ kV is given to the SSSC as seen in figure 5.19a. This causes the real power flow in the line to steadily increase to 167 MW, as seen in figure 5.19b. Figure 5.19a shows the transients in the DC bus voltages, namely V_{dc}, V_{dca}, and V_{dca1}. V_{dca} and V_{dca1} show a 120 Hz oscillation on top of the steady-state value of 10 kV. The amplitude of the 120 Hz oscillation depends on the q-axis voltage injection value, and it increases with a capacitive and inductive injections.

Table 5.4: Transformer and 'small-dt' line parameters

Transformer parameters	**Value**
Type and no.	Single phase, three
Large dt side rated voltage	54 kV
Small dt side rated voltage	18 kV
Rated MVA	20 MVA
Resistance	0.01 p.u.
Reactance	0.1 p.u.
'Small-dt' line parameters	**Value**
Conductors	2
Conductor arrangement	Horizontal
Conductor spacing	10 meters
Conductor elevation	30 meters
Conductor type	Chukar, ACSR
Line length	1 km
Ground resistivity	100 Ω-m

5.3.6 Summary and Conclusions

In this section, a SSSC — a series connected FACTS device — was constructed with a cascaded H-bridge converter for the VSC, which was not reported in literature. A new DC-side capacitor voltage balancing algorithm was developed in section 5.3.2 for the CHB converter to operate as a series connected device, whose performance was evaluated in section 5.3.4 using simulations in PSCAD and RTDS. The performance of the SSSC in controlling real power flow along the transmission line was also evaluated in section 5.3.4, which validates the effectiveness of the designed controllers. This was demonstrated using staircase and trapezoidal power reference waveforms. It was also observed that the SSSC can drive a system towards instability if the real power reference is reduced beyond a particular value, leading to sustained oscillations.

SSSC protection is also an important topic while designing protection schemes for the power network. The principle of SSSC protection lies on the fact that the converter needs to be protected from carrying transmission line fault current in event of a fault. A detailed description of the protection strategy adopted for NYPA's CSC in the SSSC mode is given in [54]. A similar strategy can be adopted for the CHB-based SSSC in future research.

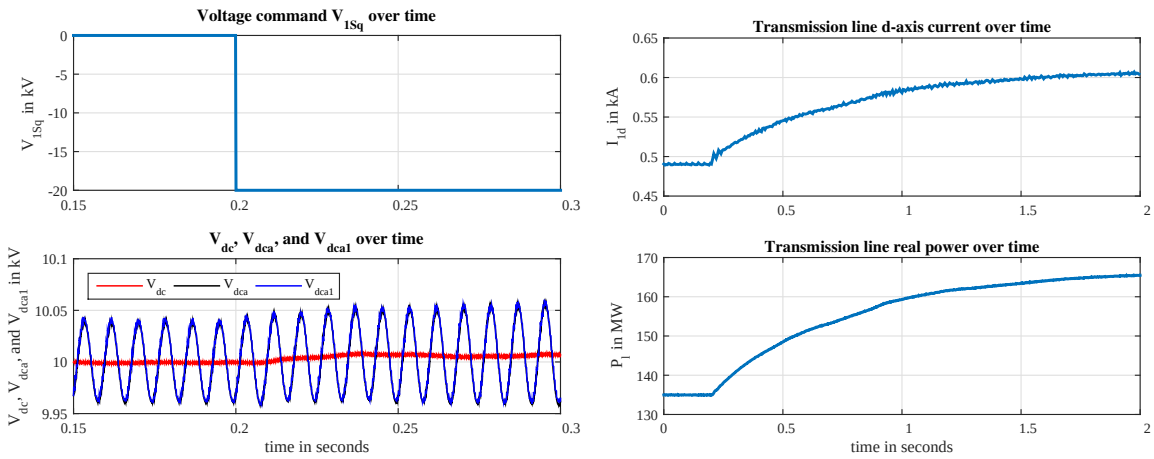

Figure 5.19: Plots of V_{dc}, V_{dca}, & V_{dca1}, I_{1abc}, & P_l for a voltage command $V^*_{1Sq} = -10$ kV at $t = 0.2$ s

5.4 Series-connected individual single-phase H-bridges

SSSCs based on Cascaded H-Bridge converters were explored in detail in the previous section. CHB converters are typically large installations rated in several MVA. The installation would be located at a single point within the network, and hence its optimal placement needs to be determined after several system studies within the network. Further, this optimal placement assumes that the location of the converter would remain as important in the future as it is now. This will not be the case if there is a change in generation, like the retirement of old power plants or the establishment of new wind and photo-voltaic power plants within other parts of the network. Large installations are typically not portable, and even if they are, it is usually a big expense for the utilities.

This can be countered by having the converter being distributed over a wider area in the form of multiple smaller devices. The replacement and relocation of these distributed devices is possible with lower costs in case of network changes. These individual SSSCs are typically rated under an MVA and can be coordinated to provide compensation in tandem with each other, thus achieving the same effect as that of a larger centralized SSSC. The SSSCs can communicate

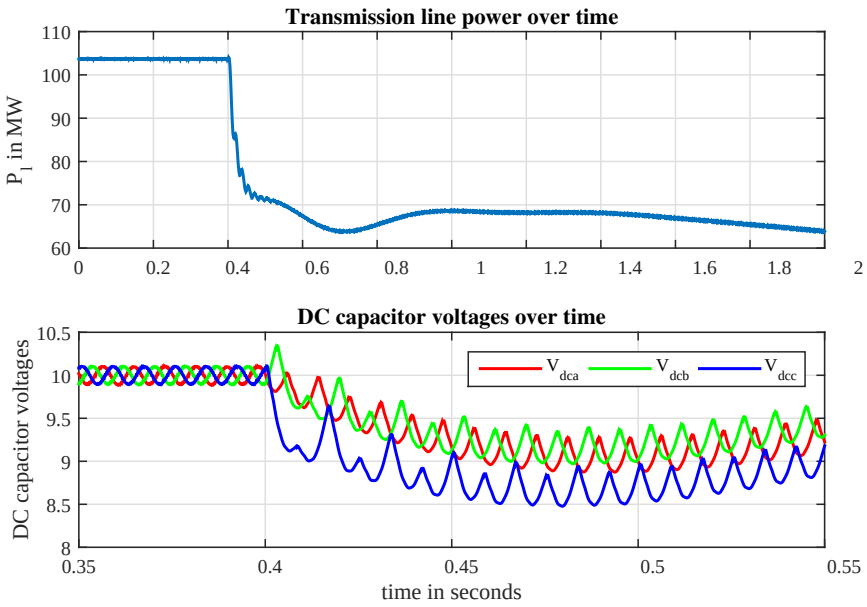

Figure 5.20: Plots of V_{dc}, V_{dca}, V_{dcb}, and V_{dcc} for a distributed SSSC with state-of-the-art controls for $V_{1Sq}^{*} = 20kV$ voltage command

with each other and determine the optimum voltage injections for each device depending on its location within the network. As a result, these series-connected FACTS devices are becoming popular for series compensation within transmission networks.

SSSCs can use various VSC topologies, however the topology with three individual H-bridges fits nicely into the distributed SSSC concept. Distributed SSSCs will be connected in series with transmission lines and located on transmission towers. Transmission towers typically have their phase conductors separated by several meters, and the physical separation makes the $3-\phi$ half-bridge converter configuration nonviable. The individual H-bridges can be mounted on the respective phase arms on the transmission line in their own housing with the interface transformer and filter. Each unit can also house its own control hardware which can control the $1-\phi$ H-bridge independently using voltage and current measurements on the phase it is connected in series with. The control for this configuration has been covered in literature [70, 71], but this control requires separate communication hardware for each H-bridge which will communicate information with a centralized location. Thus, this topology requires separate

control and communication hardware for each H-bridge.

This control was simulated in RTDS for a single SSSC using three $1-\phi$ H-bridges and its performance in controlling real power flow through a open-loop voltage injection can be seen in figure 5.20. In this figure, a AC voltage injection command of $V_{1Sq}^{*} = 20kV$ was given that caused the real line power P_l to drop to around 64 MW. It can be seen that the capacitor voltages for the individual DC buses are tightly grouped up before the command was given, but they desynchronize with each other immediately after the voltage command. It was observed that the voltages grouped up again after the system had stabilized.

A $3-\phi$ centralized controller for this application would require less control and communication hardware, and if it can be implemented for the SSSC based on individual H-bridges with the same performance or better as seen in figure 5.20, potential savings in controller and communication hardware is possible. Such a controller has not been documented in literature and in this section, a centralized controller for the distributed SSSC is proposed and developed based on the learnings of the CHB-based SSSC.

5.4.1 System Description

The distributed SSSC was simulated on the RTDS platform on a two-bus 230 kV $3-\phi$ AC system with a single transmission line interconnecting them, and the SSSC being in series with this transmission line. The transmission line parameters can be seen in table 5.3. The ratings of the small time-step interface transformer can be seen in table 5.4. The voltage angle for the receiving end bus is set at $-15°$ which establishes a power flow of 124 MW along the transmission line. The VSC topology used for the SSSC consists of three H-bridges, one per phase. Each H-bridge is controlled with the DC bus voltage reference set to 10 kV.

5.4.2 Centralized Controller design

The centralized controller discussed in this section is similar to the one discussed in section 3.3.2. The difference in the control arises from the fact that a $3-\phi$ half-bridge converter has a

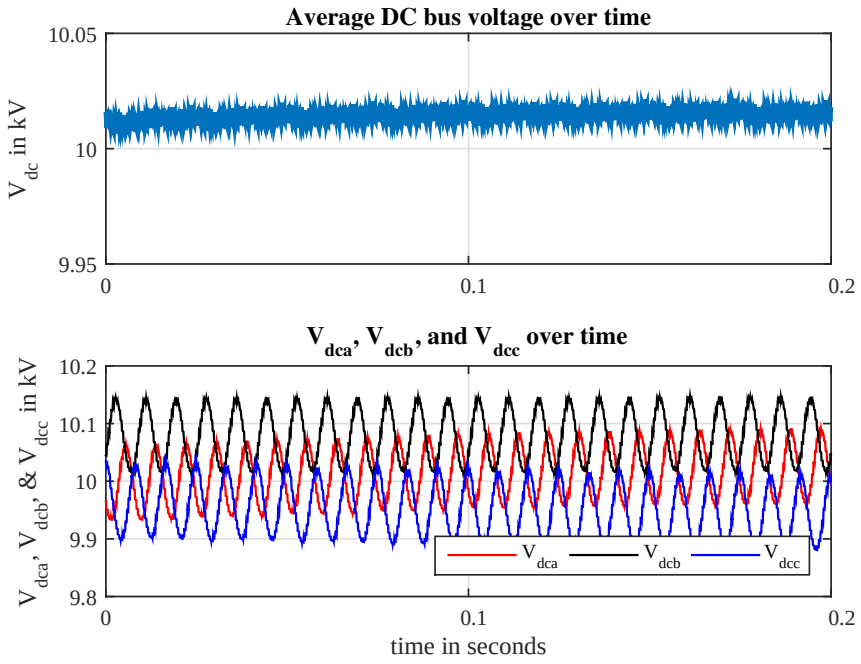

Figure 5.21: Plots of V_{dc}, V_{dca}, V_{dcb}, and V_{dcc} for a distributed SSSC with conventional controls

single DC bus for all three phases, whereas the distributed SSSC has three separate DC buses. The DC bus voltages of the distributed SSSC also have a 120 Hz oscillatory component similar to the one seen in figure 5.19a, over and above the DC bus steady-state voltage. The 120 Hz oscillatory components in V_{dca}, V_{dcb}, and V_{dcc} are all phase-shifted 120° with respect to each other, and thus the average DC bus voltage V_{dc} will reflect the steady-state value of the DC bus. Theoretically, if the average DC bus voltage is controlled in a fashion similar to the one in section 3.3.2, it should maintain the DC bus voltages of the individual H-bridges around the reference value.

However, it was observed that V_{dca}, V_{dcb}, and V_{dcc} do not remain tightly controlled around the operating point, and in fact they diverged in some situations while the average value of the DC bus voltage, V_{dc} remained steady. Figure 5.21 demonstrates this phenomenon. In this RTDS simulation, a distributed SSSC was controlled using the controller shown in figure 3.7. From the figure, it can be inferred that while the DC voltage controller can maintain V_{dc} near its reference value, the actual DC bus voltages do not converge to this value without an external

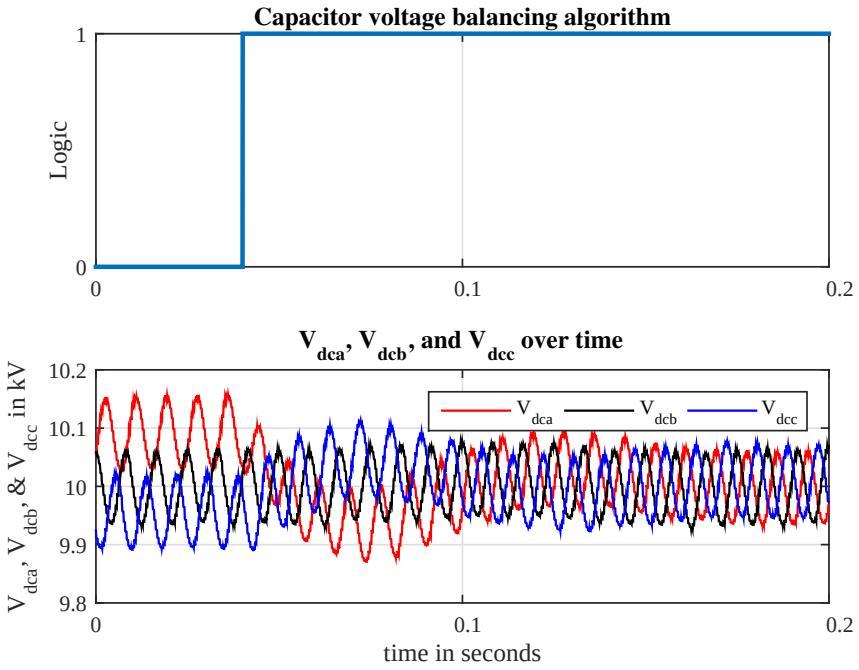

Figure 5.22: Plots of V_{dca}, V_{dcb}, & V_{dcc} showing the performance of the Capacitor Voltage Balancing algorithm based on the CHB converter

control. This is undesirable as unequal voltage injections can cause the $1-\phi$ series transformers to saturate. This problem is the primary challenge in developing a centralized controller for the individual $1-\phi$ H-bridges, and my contribution is in designing two different controllers which correct for this drift. Doing so will enable for savings in communication and controller hardware.

This is similar to the capacitor voltage balancing problem faced by the CHB-based SSSC covered in section 5.3.2, and a control algorithm similar to the one shown in figure 5.10 can be employed to rectify this. Figure 5.22 shows the effect of such an algorithm designed for the distributed SSSC in this section. It can be seen that when the control is activated, the steady-state value of V_{dca}, V_{dcb}, and V_{dcc} immediately converge to the average V_{dc} value of 10 kV.

The algorithm works, however it must be noted that the signal θ_v used in figure 5.10 is derived from the sending end voltage, whereas the rest of the control shown in figure 3.7 uses

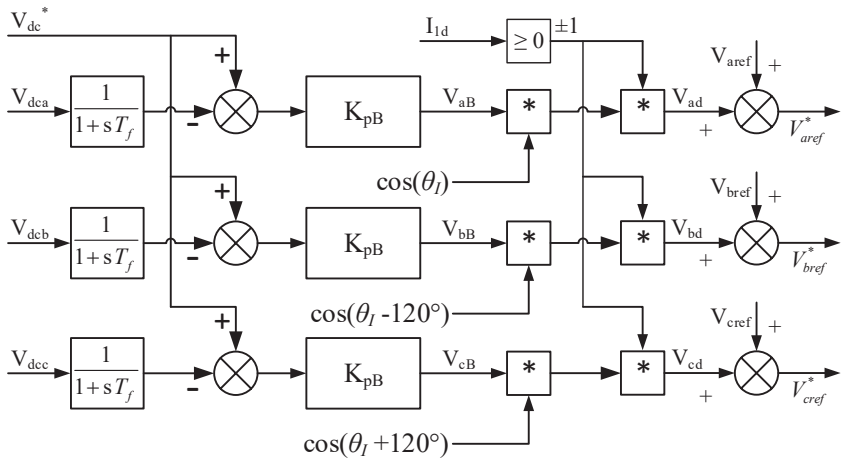

Figure 5.23: Control block diagram for the modified Capacitor Voltage Balancing algorithm

θ_I derived from the transmission line current. This was necessary in the case of the CHB-based SSSC as two different sets of quantities, V_{dci}s and V_{dcij}s, were being controlled through transmission line current. By linking up V_{dci}s and V_{dcij}s with the d-axis and the q-axis current respectively, relative to the voltage reference frame, both sets of quantities can be controlled independently with respect to each other. This is because the d- and the q- axis quantities are orthogonal to each other. When θ_I is used, $I_{1q} = 0$. This simplified the basic SSSC control, but it is not suitable for use in the capacitor voltage balancing algorithm used for the CHB-based SSSC.

However there is only one set of quantities, i.e. V_{dci} in the case of the distributed SSSC and thus it is possible to simplify the controls to a certain extent. For a rotating reference frame aligned with I_{1a}, $P_s = V_{1d}I_{1d}$. By injecting a voltage in phase with I_{1d} depending upon the drift between V_{dci} and V_{dc}, it is possible to correct for the difference between the two. The H-bridge which has a lower DC bus voltage absorbs real power by injecting a slightly larger d-axis voltage, and vice-versa. Figure 5.23 shows the control block diagram describing the modified capacitor voltage balancing control. The major advantage of this control is that it uses θ_I instead of the θ_v used in figure 5.10.

The performance of this control algorithm can be seen in figure 5.24, and it is apparent

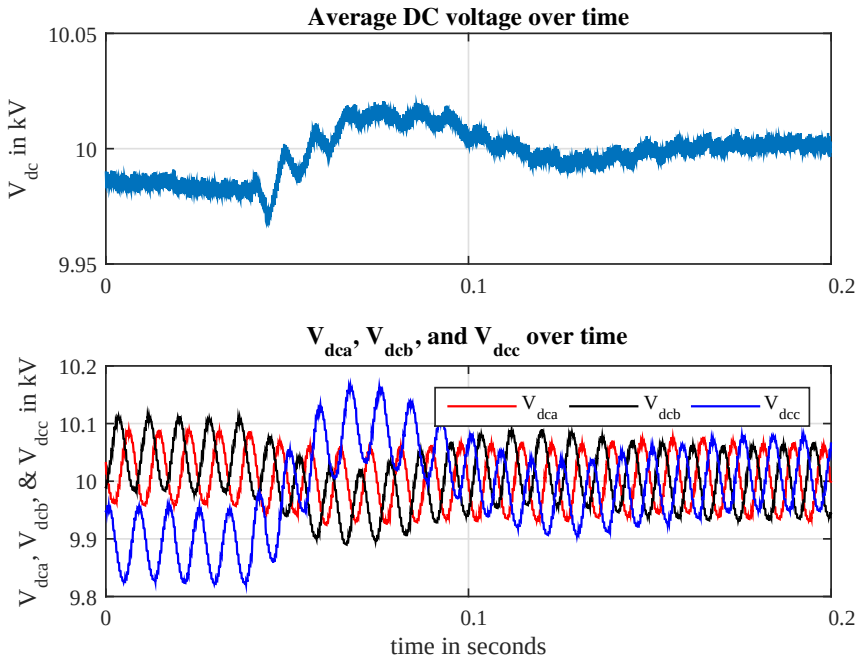

Figure 5.24: Plots of V_{dca}, V_{dcb}, & V_{dcc} showing the performance of the modified Capacitor Voltage Balancing algorithm

that the controller works just as well as the controller described in figure 5.10. The transient performance appears to be slightly different, but this is attributed to the difference in the initial conditions in figures 5.22 and 5.24. Figure 5.25 shows the performance of the controller when given a q-axis voltage command of $V^*_{1Sq} = 20kV$. The voltage command is given at $t = 0.4$ s, and this causes the power flow to reduce from 124 MW to 71.2 MW. The figure also shows the DC bus voltage variation when the command is given. The controller keeps the individual DC bus voltages close to the average, and the DC average voltage regulates itself over a longer time scale. If we compare figures 5.20 and 5.25 for their transient performance, it is clear that the controller designed in figure 5.23 has better transient performance than the state-of-the-art controller for the same amount of open-loop voltage injection.

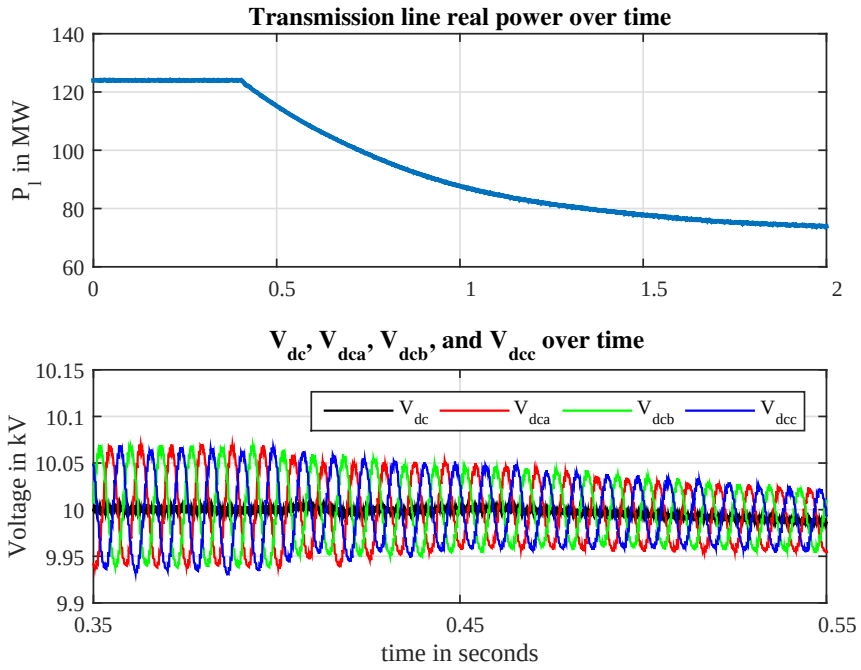

Figure 5.25: Plots of P_l, V_{dc}, V_{dca}, V_{dcb}, & V_{dcc} showing the performance of the modified controller for $V^*_{1Sq} = 20kV$

5.4.3 Conclusion

In this section, a modified centralized controller for a distributed SSSC was discussed and its performance was evaluated. Its performance was compared with the capacitor voltage balancing controller and it was observed that there was no drop in performance with the modified controller. The modified controller simplified the control to a certain extent as it uses the same rotating frame of reference as the basic SSSC control. The controller performance was also evaluated in controlling real power flow along the transmission line, and it had a slightly better transient performance than the state-of-the-art controller for the same amount of open-loop voltage injection of $V^*_{1Sq} = 20kV$.

5.5 Conclusion

In this chapter, we discussed the Static Series Synchronous Compensator which is a series-connected FACTS device used in controlling transmission line real power flow. The SSSC based on the Cascaded H-Bridge converter was proposed in this chapter and its performance was evaluated. Distributed SSSCs were also discussed in detail in this chapter and an alternative centralized control scheme for distributed SSSCs was proposed. Another application of the SSSCs is in power oscillation damping, which will be discussed in detail in the next chapter.

Chapter 6

Mitigation of Power Oscillations

6.1 Introduction

Conventional power systems consist of well-defined generation centers and large load centers, with the two centers typically connected by extra high voltage (EHV) AC transmission lines, due to the geographic distance between the two centers. The generation centers are typically thermal or hydro power plants where stored chemical or potential energy is converted into electrical energy by means of $3-\phi$ AC synchronous generators. The power balance relationship for the synchronous generator is modeled as a second-order damped oscillator described by the swing equation [44],

$$M\ddot{\delta} = P_m - P_e - D\dot{\delta} \tag{6.1}$$

where, M, D, P_e and P_m are the inertia, damping, electrical power output and mechanical power input for the synchronous generator. Power flow between two synchronous generators connected by a transmission line can be written as

$$P_e = \frac{E_1 E_2}{X_t} \sin(\delta_1 - \delta_2) \tag{6.2}$$

where $E_1\angle\delta_1$ and $E_2\angle\delta_2$ are the internal EMFs of the two generators in per unit. X_t is the total reactance between the two internal EMFs, including the transmission line reactance and the synchronous reactance of the two generators, also in per unit. If M_1, D_1 and M_2, D_2 are the rotational inertia and mechanical damping of the two synchronous generators, then the swing equations for the two generators can be written as

$$\begin{aligned} M_1\dot{\omega_1} &= P_{m1} - \frac{E_1E_2}{X_t}\sin(\delta_1 - \delta_2) - D_1\dot{\delta_1} \\ M_2\dot{\omega_2} &= P_{m2} + \frac{E_1E_2}{X_t}\sin(\delta_1 - \delta_2) - D_2\dot{\delta_2} \\ \dot{\delta_1} &= \omega_1 \\ \dot{\delta_2} &= \omega_2 \end{aligned} \tag{6.3}$$

If the equation set (6.3) is linearized around an operating point, we get

$$\begin{bmatrix} \Delta\dot{\delta}_1 \\ \Delta\dot{\delta}_2 \\ \Delta\dot{\omega}_1 \\ \Delta\dot{\omega}_2 \end{bmatrix} = \begin{bmatrix} 0 & 0 & \omega_s & 0 \\ 0 & 0 & 0 & \omega_s \\ -\frac{E_1E_2}{X_tM_1}\cos\delta_{12} & \frac{E_1E_2}{X_tM_1}\cos\delta_{12} & -\frac{D_1\omega_s}{M_1} & 0 \\ \frac{E_1E_2}{X_tM_2}\cos\delta_{12} & -\frac{E_1E_2}{X_tM_2}\cos\delta_{12} & 0 & -\frac{D_2\omega_s}{M_2} \end{bmatrix} \begin{bmatrix} \Delta\delta_1 \\ \Delta\delta_2 \\ \Delta\omega_1 \\ \Delta\omega_2 \end{bmatrix} + \begin{bmatrix} 0 & 0 \\ 0 & 0 \\ \frac{1}{M_1} & 0 \\ 0 & \frac{1}{M_2} \end{bmatrix} \begin{bmatrix} \Delta P_{m1} \\ \Delta P_{m2} \end{bmatrix} \tag{6.4}$$

where δ_{12} is the steady state rotor angle difference, and $\Delta\delta_i$ and ΔP_{mi} represent the small signal perturbations in δ_i and P_{mi}. From equation (6.4), it can be inferred that the square matrix has a zero eigenvalue, one negative exponential eigenvalue, and two complex conjugate eigenvalues with negative real parts. Equation (6.4) describes a simple two-machine power system, and in case of larger networks, each generator within the network will have its own second-order differential equation, which is coupled with other second-order equations through

Kirchoff's Voltage and Current laws. The eigenvalues of the resultant state-space formulation will also consist of complex eigenvalue pairs, which results in the emergence of oscillatory modes within the power system [72] for each complex pair. These oscillatory modes are excited by any impulse or step changes in the power flow, for example, by loss of critical transmission lines, loss of large loads, or change in renewable energy output. They are typically damped by the machine damping term and load, but if a situation arises where the system damping is not adequate, sustained power oscillations can be observed in the network.

As the penetration of renewable energy resources increases within power systems, the potential for excitation of these oscillatory modes increases. Further, the increased penetration of renewables would be accompanied with reduction and replacement of conventional sources of generation leading to reduction in the aggregate inertia of the network and this has an adverse effect on the stability of power systems [7].

The problem of power oscillation damping has been studied extensively in literature, and several solutions have been proposed to resolve this issue. This includes power system stabilizers (PSS) [73], thyristor-controlled switched capacitors (TCSCs) and Static VAR compensators [74, 75, 76], Static Synchronous Compensators (STATCOM) [77, 78], Unified Power Flow Controllers (UPFC) [33], SSSCs [79], and VSC-HVDC based wind farms [80], among others. However, current literature in power oscillation damping gives a lot of emphasis on the design of the Power Oscillation Damping (POD) controller, and assumes that the synchronous generator data is readily available to the controller.

This is typically not the case because power oscillations can occur anywhere in the network. Further, slow inter-area mode oscillations observed throughout the network are due to several generators swinging coherently with each other, and this makes it difficult to use a particular generator's parameters as the input to a POM controller. Under such circumstances, the controller needs to use local measurements like line power or line frequency in order to damp these oscillations. Further, the oscillation frequency can vary with network conditions and operating points [81], and thus the controller must be adaptive enough to estimate these changes

in real-time and correct accordingly.

Damping controllers based on energy storage like the BES (battery energy storage)-enabled shunt compensation, e.g. STATCOMs and front-end converters of wind farms, and the UPFC mitigate power oscillations by exchanging real power with the system. By doing so, they damp the oscillations by absorbing and releasing power into the network and they can modify the oscillatory behavior of the network through an increase in the damping coefficients σ_i for the mode under investigation. Other compensators like the PSS and the SVC can indirectly impact the power flow within the network by changing the voltage magnitude of the bus where the controlling equipment is connected. The changes in bus voltage affects the power consumption of constant-current and constant-impedance type loads, which indirectly damps out the power oscillations on the network. Thus the SVC and the PSS are also able to change the network dynamics by increasing σ_i for the mode being damped. The TCSC is a series compensation device that introduces small perturbations in X_t to damp power oscillations. However, the control for TCSCs is nonlinear, whereas the SSSC has linear control. This provides a significant advantage to the SSSC.

This chapter attempts to design a adaptive Power Oscillation Mitigation (POM) controller using a SSSC which is a series connected FACTS device. The SSSC, by design, does not exchange real power with the transmission line, except to charge its DC bus, and typically does not have battery storage on its DC bus. The SSSC is connected in series with a transmission line, and can only control the power flow on that particular transmission line. It can be shown that in a simple two-bus AC system with a SSSC on the transmission line, the power flow along the line can be given as [82]

$$P_l = \frac{E^2}{X_t}\sin(\delta_1 - \delta_2) + \frac{E}{X_t}V_q \cos\left[\frac{\delta_1 - \delta_2}{2}\right] \tag{6.5}$$

where $E\angle\delta_1$ and $E\angle\delta_2$ are the thevenin voltages of the sending and receiving end generators respectively, X_t is the total reactance, and V_q is the series voltage injection made by the SSSC.

V_q is almost orthogonal to the line current and hence there is little real power exchange between the SSSC and the transmission line at any point. Any real power exchange is done to cover for the power losses in the switches of the converter and this replenishes the DC bus. During a transient event, $(\delta_1 - \delta_2)$ goes through perturbations which causes line power P_l to oscillate. If the perturbations in $(\delta_1 - \delta_2)$ are small, Eq. (6.5) can linearized around δ_{12} as,

$$\Delta P_l = \left[\frac{E^2}{X_t}\cos\delta_{12}\right](\Delta\delta_1 - \Delta\delta_2) - \left[\frac{E}{2X_t}V_{q0}\sin\frac{\delta_{12}}{2}\right](\Delta\delta_1 - \Delta\delta_2) + \left[\frac{E}{X_t}\cos\frac{\delta_{12}}{2}\right]\Delta V_q \quad (6.6)$$

If we want to eliminate the oscillations in P_l, we can make $\Delta P_l = 0$ by injecting a small signal ΔV_q to cancel out the oscillations. If we assume that the SSSC is not injecting any voltage at $t = 0$, then $V_{q0} = 0$. We can rewrite Eq. (6.6) as

$$\Delta V_q = -\frac{E\cos\delta_{12}}{\cos\frac{\delta_{12}}{2}}(\Delta\delta_1 - \Delta\delta_2) \quad (6.7)$$

By injecting a q-axis voltage ΔV_q in opposition to the perturbation in $(\delta_1 - \delta_2)$, the SSSC can eliminate the oscillations along the transmission line. If Eq. (6.5) is used in Eq. (6.3), we can write down the equations as

$$\begin{aligned}
M_1\dot{\omega_1} &= P_{m1} - \frac{E^2}{X_t}\sin(\delta_1 - \delta_2) - \frac{EV_q}{X_t}\sin\frac{(\delta_1 - \delta_2)}{2} - D_1\omega_1 \\
M_2\dot{\omega_2} &= P_{m2} + \frac{E^2}{X_t}\sin(\delta_1 - \delta_2) + \frac{EV_q}{X_t}\sin\frac{(\delta_1 - \delta_2)}{2} - D_2\omega_2 \\
\dot{\delta_1} &= \omega_1 \\
\dot{\delta_2} &= \omega_2
\end{aligned} \quad (6.8)$$

Now, as before, steady-state value of V_q, V_{q0} is considered as zero. If it is also assumed that the small-signal deviations in P_{m1} and P_{m2} are also negligible due to the slow time-scale of the

governors, then the linearized small-signal model for Eq. (6.8) can be written as

$$\begin{bmatrix} \Delta\dot{\delta}_1 \\ \Delta\dot{\delta}_2 \\ \Delta\dot{\omega}_1 \\ \Delta\dot{\omega}_2 \end{bmatrix} = \begin{bmatrix} 0 & 0 & \omega_s & 0 \\ 0 & 0 & 0 & \omega_s \\ -\frac{E^2}{X_t M_1}\cos\delta_{12} & \frac{E^2}{X_t M_1}\cos\delta_{12} & -\frac{D_1\omega_s}{M_1} & 0 \\ \frac{E^2}{X_t M_2}\cos\delta_{12} & -\frac{E^2}{X_t M_2}\cos\delta_{12} & 0 & -\frac{D_2\omega_s}{M_2} \end{bmatrix} \begin{bmatrix} \Delta\delta_1 \\ \Delta\delta_2 \\ \Delta\omega_1 \\ \Delta\omega_2 \end{bmatrix} + \begin{bmatrix} 0 \\ 0 \\ -\frac{E}{X_t M_1}\cos\frac{\delta_{12}}{2} \\ \frac{E}{X_t M_2}\cos\frac{\delta_{12}}{2} \end{bmatrix} \begin{bmatrix} \Delta V_q \end{bmatrix} \tag{6.9}$$

If we substitute Eq. (6.7) in Eq. (6.9), we get,

$$\begin{bmatrix} \Delta\dot{\delta}_1 \\ \Delta\dot{\delta}_2 \\ \Delta\dot{\omega}_1 \\ \Delta\dot{\omega}_2 \end{bmatrix} = \begin{bmatrix} 0 & 0 & \omega_s & 0 \\ 0 & 0 & 0 & \omega_s \\ 0 & 0 & -\frac{D_1\omega_s}{M_1} & 0 \\ 0 & 0 & 0 & -\frac{D_2\omega_s}{M_2} \end{bmatrix} \begin{bmatrix} \Delta\delta_1 \\ \Delta\delta_2 \\ \Delta\omega_1 \\ \Delta\omega_2 \end{bmatrix} \tag{6.10}$$

Comparing Eqs. (6.4) and (6.10), it is evident that the SSSC modifies the A matrix in such a way that the compensated oscillatory modes are eliminated. The eigenvalues of the A matrix in Eq. (6.10) are $0,\ 0,\ -\frac{D_1\omega_s}{M_1}, \&\ -\frac{D_2\omega_s}{M_2}$, which implies that the compensated response would resemble that of an over-damped system if the compensation is perfect. Another observation we can make from the A matrix is that $\Delta\delta_1$ and $\Delta\delta_2$ are uncontrollable, which implies that the SSSC cannot control the oscillations in $(\delta_1 - \delta_2)$, but only impact the oscillations in P_l.

6.2 Modal Estimation

As discussed previously, the dynamic behavior of a given power system during transients will be defined by the eigenvalues of the system. The transient behavior attributed to electromagnetic

effects like the field winding and the damper windings are comparatively faster (> 10 Hz) and are heavily damped, and thus they do not affect power flow greatly. However, the transients originating from electro-mechanical phenomenon as described in Eq. (6.1) typically lie in the $0.1 \leq f < 3$ Hz range - depending on the machine inertia and system impedance - and do not have sufficient damping. This leads to sustained power oscillations which can stress power equipment. If the damping is negative, the oscillations can grow beyond stability limits, causing a cascading failure throughout the network.

The design of the POM controller depends upon estimation of the eigenvalues present in the real power signal. In the context of signal analysis and processing, the eigenvalues are termed as modes, and this term will be used in this chapter. Any measured signal $y(t)$ can be described as a sum of complex exponential terms as [72]

$$y(t) = y_0(t) + \sum_{i=1}^{N} R_i e^{(\sigma_i + j\omega_i)t} + n(t) \tag{6.11}$$

where

$y_0(t)$: DC and exponential modes which lead to the DC bias in the signal

$n(t)$: signal noise

N: Number of oscillatory modes

R_i: Complex residue of the i^{th} mode

$\sigma_i + j\omega_i$: Complex angular frequency of the i^{th} mode

Modal estimation implies the estimation of R_i, σ_i, and ω_i for all $i \in [1, N]$. The modal estimation can be done in the time domain, as well the frequency domain. Frequency domain techniques like using band-pass filters can be used for this purpose, however frequency domain filters tend to distort the reference signal due to the different phase shifts introduced for the various modes by the filter. The most popular time-domain estimation techniques like the Prony method and the Matrix Pencil method can be used to estimate the modal parameters without distorting the signal. In this chapter, the Matrix Pencil estimation technique as described in [83] will be used for modal estimation.

6.2.1 Matrix Pencil Method

The Matrix Pencil method involves estimating the modal information from a sampled signal like real power or line voltage magnitude. The sampled data $y(k)$ from the signal with n sample points is converted in to the matrix $[Y]$ as

$$[Y] = \begin{bmatrix} y(0) & y(1) & \cdots & y(l) \\ y(1) & y(2) & \cdots & y(l+1) \\ \vdots & \vdots & \ddots & \vdots \\ y(n-l-1) & y(n-l) & \cdots & y(n-1) \end{bmatrix}_{(n-1)\times(l+1)} \tag{6.12}$$

where l is called as the 'pencil parameter' and is selected in this case as the closest integer to $\frac{n}{2.5}$. The next step is to carry out the singular value decomposition (SVD) of Y as

$$[Y] = [U][\Sigma][V]^H \tag{6.13}$$

where the superscript 'H' denotes the conjugate transpose. $[U]$ and $[V]$ are unitary matrices and are made up to the eigenvectors of $[Y][Y]^H$ and $[Y]^H[Y]$ respectively, and $[\Sigma]$ is a diagonal matrix containing the singular values of $[Y]$. The matrix $[\Sigma]$ contain $l+1$ singular values and it needs to be truncated based on some criterion. In this chapter, the singular values σ_i that are more than 10^{-6} times smaller than the largest singular value are truncated. The eigenvectors in $[V]$ corresponding to the truncated singular values in $[\Sigma]$ are also deleted. The new truncated matrices $[\Sigma']$ and $[V']$ are then further processed. Let m be the number of eigenvalues left after the truncation. The parameter m is the number of estimated significant modes that are present in the signal y.

Matrices $[V_1']$ and $[V_2']$ are created by removing the last and the first row from $[V']$. Two

new matrices $[Y_1]$ and $[Y_2]$ are created as

$$[Y_1] = [U][\Sigma][V_1']^H \tag{6.14}$$

$$[Y_2] = [U][\Sigma][V_2']^H \tag{6.15}$$

The next step involves calculation for the Moore-Penrose pseudoinverse of $[Y_1]$ as

$$[Y_1]^+ = \{[Y_1]^H[Y_1]\}^{-1}[Y_1]^H \tag{6.16}$$

A vector $[z]$ is created using the eigenvalues of $[Y_1]^+[Y_2]$. The vector is truncated to a size of $m \times 1$ and a square matrix $[Z]$ is created from $[z]$ as

$$[Z] = \begin{bmatrix} 1 & 1 & \cdots & 1 \\ z_1 & z_2 & \cdots & z_m \\ \vdots & \vdots & \ddots & \vdots \\ z_1^{n-1} & z_2^{n-1} & \cdots & z_m^{n-1} \end{bmatrix} \tag{6.17}$$

The complex frequency of the m modes is calculated as a vector $[s] = f_s \log_e[z]$. f_s is the sampling frequency of the signal. The residues of these modes can then be calculated as

$$\begin{bmatrix} R_1 \\ R_2 \\ \vdots \\ R_m \end{bmatrix} = [Z]^+ \begin{bmatrix} y(0) \\ y(1) \\ \vdots \\ y(n-1) \end{bmatrix} \tag{6.18}$$

R_i and s_i are both complex numbers, with $s_i = \sigma_i + j\omega_i$ rad/s. The Matrix Pencil method estimates the fit for the reference signal with several hundred complex frequency pairs and exponential DC modes. However, most of these modes are extremely weak in terms of their energy content, or have extremely high damping, which makes them irrelevant to our application.

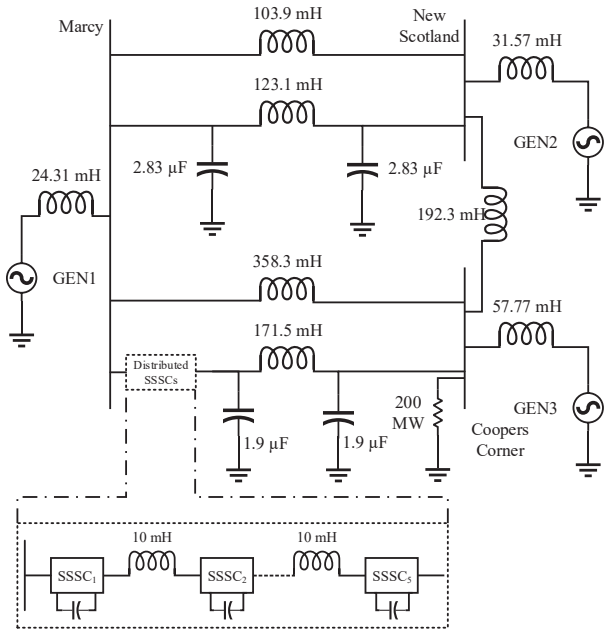

Figure 6.1: NYPA's three-bus AC system around Marcy substation

By eliminating them, an educated concise guess can be made about the dominant modes present in the measured signal. The DC modes are present for establishing the DC bias in the signal, and can be eliminated before-hand by subtracting the signal average from the raw signal data.

6.3 POM with SSSCs using single-phase H-bridges

In this section, the application of distributed SSSCs in mitigating power oscillations will be investigated in New York Power Authority's (NYPA) 345 kV system. For the purpose of simulation, five SSSCs, each having three $1-\phi$ H-bridges as their base converter are connected in series with the Marcy - Coopers Corner transmission line. Each SSSC is locally controlled using the centralized control algorithm developed in section 5.4, and an additional POM controller provides an AC voltage reference to the inner control loop. The design of this POM controller is my primary contribution from this section.

Table 6.1: Generator Parameters

Parameter	Unit	**GEN1**	**GEN2**
Apparent power	MVA	615	911
Rated line voltage	kV	15	26
X''_d	p.u.	0.23	0.193
X'_d	p.u.	0.2995	0.266
X_d	p.u.	0.8979	2.04
X''_q	p.u.	0.2847	0.191
X'_q	p.u.	n.a.	0.262
X_q	p.u.	0.646	1.960
X_p	p.u.	0.2396	0.154
T'_{d0}	s	7.4	6.0
T''_{d0}	s	0.039	0.039
T'_{q0}	s	0.071	0.9
R_a	Ω	0.001	0.001
Inertia Constant	s	5.148	2.486
Damping	p.u.	0.01	0.01
Air Gap Factor	n.a.	0.95	1.0

6.3.1 Equipment Description

AC System

The simulation is performed on the three-bus AC power system within New York Power Authority's (NYPA) network around Marcy substation as shown in [84]. The system voltage base is taken to be 345 kV, and the apparent power base at 100 MVA. The circuit is replicated here with the appropriate inductance and capacitance values in figure 6.1, as per the base MVA and base kV selected. The transmission lines represented by the π-model are actual transmission lines, whereas the simple inductances represent the equivalent power flow between the buses except for the direct transmission path. A 200 MW resistive load was connected at the Coopers Corner bus.

The voltage sources at Marcy and New Scotland buses are modeled as synchronous generators, whereas the voltage source at Coopers Corner is modeled as a stiff voltage source. Table 6.1 lists the parameters used for the two generators, as obtained from [85], with assumptions made for the missing parameters. The three voltage sources are initialized with the following

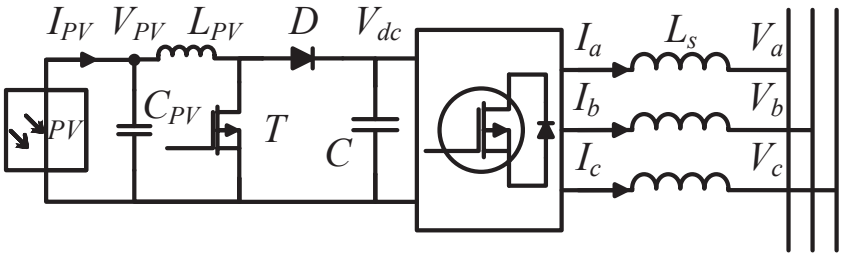

Figure 6.2: Circuit diagram for the designed photovoltaic system

per unit voltage values:

1. GEN1: $1.0\angle 0°$
2. GEN2: $1.0\angle -1.146°$
3. GEN3: $0.97\angle -10°$

The voltage angle values for GEN2 and GEN3 are selected in such a way that a reasonable power flow of around 160 MW is established on the Marcy - Coopers Corner transmission line.

Photovoltaic System

For the purpose of this study, a 30 MW photovoltaic (PV) plant was designed with a 3-ϕ two-level inverter connecting the photovoltaic system to the Marcy bus. The block diagram for the system can be seen in figure 6.2. A simple boost converter was used in the intermediate stage instead of the conventional dual-active bridge (DAB) converter since the design of the PV plant was not the primary focus of this paper.

The details of the PV system can be seen in table 6.2. The PV cells are operated at the maximum power point (MPPT) using the 'incremental conductance' algorithm [86], which determines the duty cycle D for the boost converter. The boost converter maintains the MPPT voltage across the PV terminals. The grid side inverter has two functions: maintain the DC bus voltage V_{dc} at a constant value, and transfer the real power produced by the PV cells to the grid. The grid-side inverter also provides voltage support in the absence of PV generation.

Table 6.2: Photovoltaic System Parameters

Parameter	Unit	Value
PV cell parameters		
Effective cell area	m^2	0.025
PV cell series resistance	Ω	0.01
PV cell shunt resistance	Ω	100
Diode ideality factor	n.a.	1.5
Band gap energy	eV	1.103
Reference dark current	kA	10^{-13}
PV cell short-circuit current	kA	0.0025
Temperature coefficient of photo current	A/K	0.001
PV array parameters		
Cells in series in each string	n.a.	36
Parallel strings in a module	n.a.	3
Series modules in each module string	n.a.	150
Module strings in parallel per array	n.a.	1000
Reference irradiation	W/m^2	1000
Reference temperature	$^\circ C$	25
Array open circuit voltage	kV	4.856
Array short circuit current	kA	7.687
Converter and transformer parameters		
L_{PV}	H	0.1
C_{PV}	μF	400
C	μF	4700
V_{dc}	kV	50
Transformer turns ratio	kV/kV	17.32/345
L_s	p.u.	0.14

6.3.2 Impact of Renewable Resources

Power oscillations are triggered within a network due to any event that would affect Eq. (6.1), like loss of transmission lines or generation. But these events are classified as contingencies, i.e. they are not expected to happen on a regular basis. Renewable energy sources like wind farms and PV plants are intermittent sources of generation which generate a variable amount of power depending upon weather conditions. The amount of power being generated by renewable sources is also uncontrollable to a certain extent. Renewable sources act like a negative load within the system which constantly excite the power system to produce oscillations within the

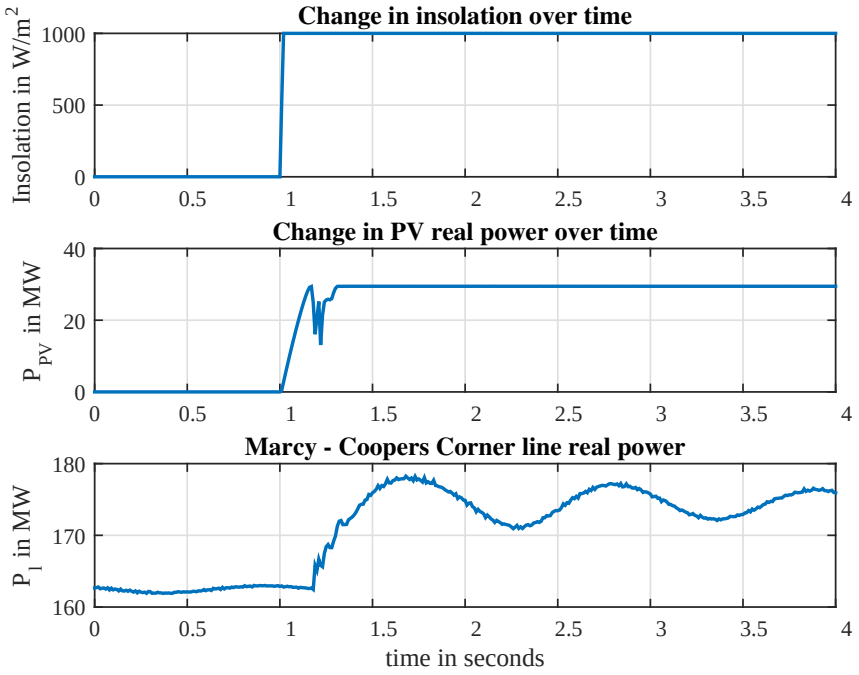

Figure 6.3: Impact of PV power injection on real power flow along the Marcy - Coopers Corner transmission line

network.

Finally, renewable sources that do not have any dedicated battery storage are inertia-less, in contrast with conventional sources of generation. Thus, if renewable generation replaces the older 'synchronous generator'-based power plants, it would lead to a net reduction of inertia within the network. This is undesirable as it will worsen the problem of power oscillations induced by the renewables within the network [7, 72]. Considering the current rate of growth of renewable energy resources as compared to the conventional sources of generation [3], it is expected that the power oscillation issues associated with renewable energy resources will become more prevalent as their penetration within power networks rises.

Fig. 6.3 shows the impact of the 30 MW PV plant as described in section II on the NYPA three-bus AC system as the plant produces real power as the weather becomes favorable for PV generation. The insolation rises to 1 kW/m^2 at $t = 1$ s, which causes the PV system's real power output to steadily rise to 30 MW. This sudden injection of real power near the Marcy

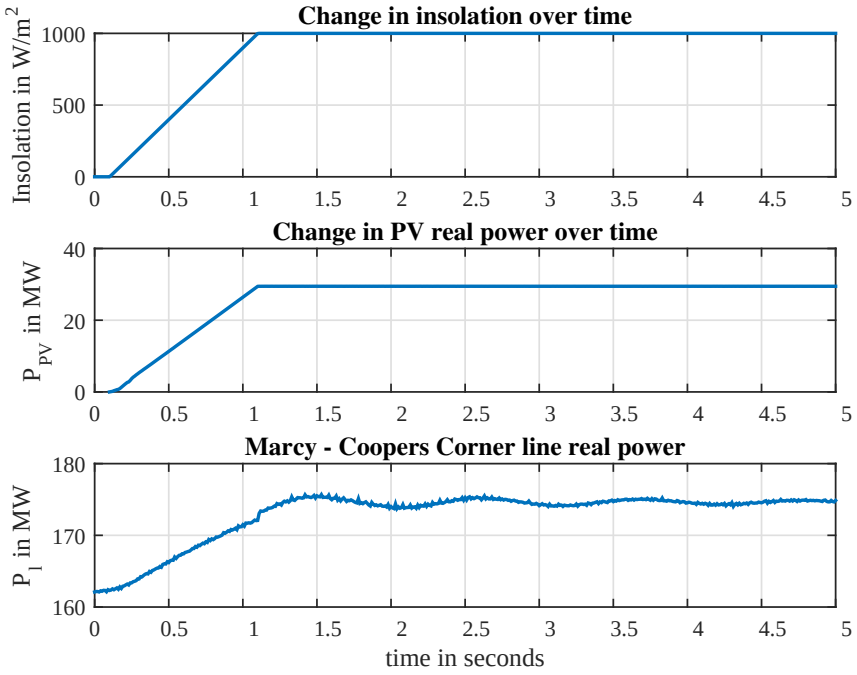

Figure 6.4: Power oscillations on the Marcy - Coopers Corner line due to a PV injection of 30 MW over 1 s

bus triggers under-damped oscillations in the steady-state real power flow P_l on the Marcy - Coopers Corner transmission line. From figure 6.3, it can be seen that the oscillations have a peak-to-peak value of 10 MW on their first swing, which is relatively quite high. A similar situation will occur when the plant stops producing real power as the sunlight reduces due to weather conditions.

However, this is not quite realistic, and the power output of the PV plant typically has a ramp rate associated with it. Fig. 6.4 shows the case when the same PV plant reaches its maximum power output in 1 second. It is clear from the figure that the addition of the ramp rate reduces the amplitude of the power oscillations, however they are not completely removed. Also, other events like line switching, faults, etc. are instantaneous events which can trigger large power oscillations, and thus it makes sense to design the POM controller based on the data obtained from fig. 6.3.

The Matrix Pencil method estimates the fit for the curve shown in figure 6.5, and the list of

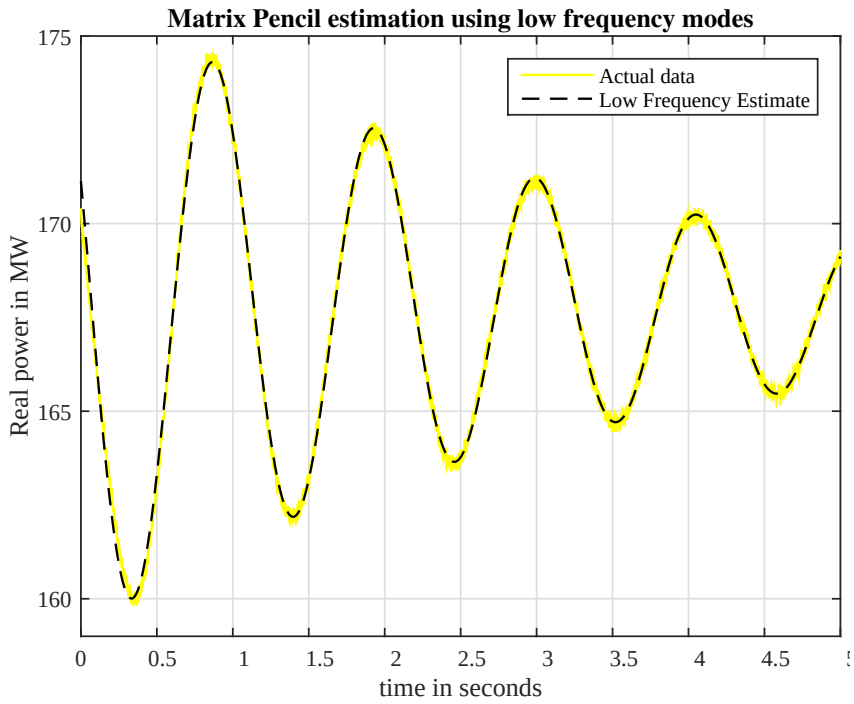

Figure 6.5: Comparison of the actual signal with the Matrix Pencil estimate using $f_{osc} = 0.9424$ Hz and exponential modes

modes, including exponential modes, obtained through this process for figure 6.5 can be seen in table 6.3.

From the results of this analysis, we can see that $f_{osc} = 0.9424$ Hz is the most dominant oscillatory mode in the system, and it is also the least damped with a damping ratio of 0.2944. The exponential modes perform the function of establishing the DC power flow within the

Table 6.3: Dominant modes in the NYPA three-bus system

Frequency (Hz)	Damping coefficient (s^{-1})	Residue (MW)	Phase (rad)
0	3.0980	0.4987	-3.1416
0	0.00023	167.8370	0
1.7515	1.1300	0.4746	2.8063
1.9079	0.8671	0.3407	-1.3983
1.1247	0.7647	0.1091	1.3615
0.9424	0.2944	4.2228	1.1053

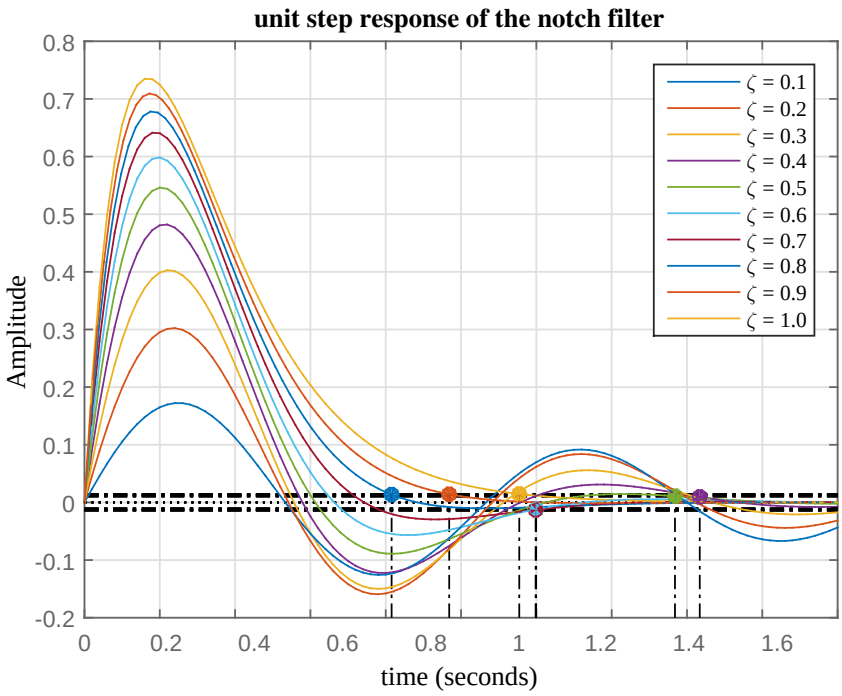

Figure 6.6: Step response of different notch filters with $0.1 \leq \zeta \leq 1.0$ for optimizing settling time

system which is 167.837 MW. The other modes have much smaller residues and higher damping than f_{osc}, and do not contribute to the estimate greatly. This can be verified by visually comparing the actual curve in figure 6.5 with the dominant mode and the exponents, as seen in the low frequency estimate.

6.3.3 Damping Controller Design

The problem of designing controllers for damping power oscillations has been discussed in literature [33]. Damping controllers typically employ FACTS devices to perform their function, but other alternatives like using HVDC converters for damping has also been proposed [87]. Distributed series-connected FACTS devices, which are essentially small Static Series Synchronous Compensators (SSSCs) of lower rating, will be used for the purpose of power oscillation damping.

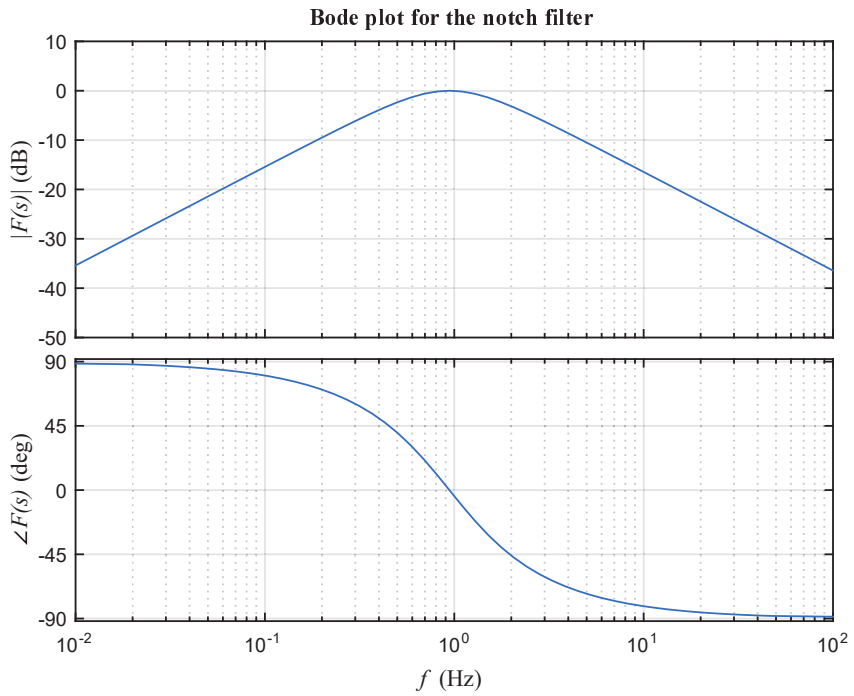

Figure 6.7: Bode plot for the notch filter transfer function given in Eq. (6.20).

The reference signal for the damping controller can be obtained from various parameters, and for the purpose of this paper, transmission line real power is used. The real power signal P_l in this case consists of the DC component and other harmonics, so a second-order notch filter centered on f_{osc} is used to extract the oscillatory mode from P_l. The general structure of this filter is

$$F(s) = \frac{2\zeta\omega_{osc}s}{s^2 + 2\zeta\omega_{osc}s + \omega_{osc}^2} \tag{6.19}$$

where $\omega_{osc} = 2\pi f_{osc}$ rad/s. Selection of ζ depends upon how well the filter rejects the initial step response, specifically, the filter with the lowest settling time. The step response of the filter was plotted for various values of ζ, which can be seen in fig. 6.6. It can be seen from the figure that the lowest settling time for a 2% band margin, it is suitable to select $\zeta = 0.8$. Thus, the transfer function of the selected notch filter is

$$F(s) = \frac{9.474s}{s^2 + 9.474s + 35.06} \tag{6.20}$$

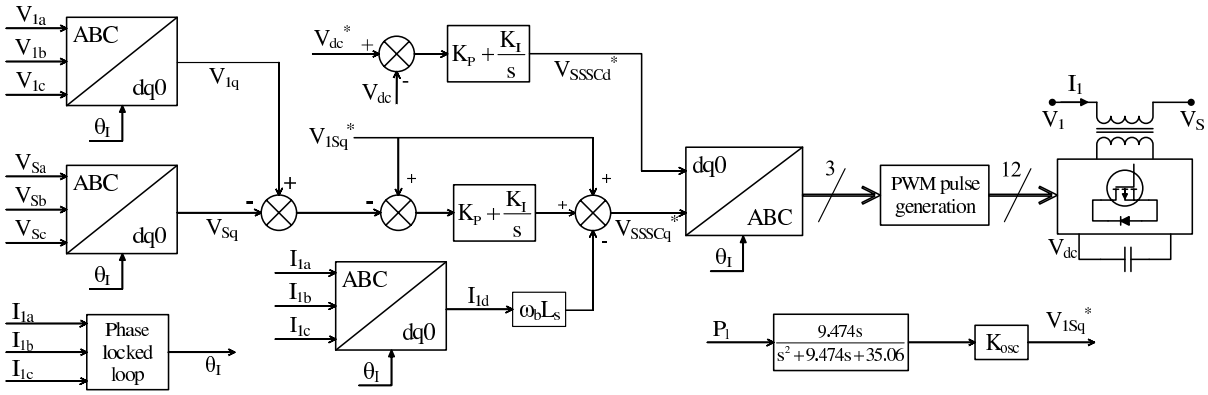

Figure 6.8: Control block diagram for a single SSSC with the damping controller.

The bode plot for equation (6.20) is shown in figure 6.7.

6.3.4 Implementation and Results

The output of the notch filter as designed in the previous subsection is then given to multiple distributed series FACTS controllers. i.e. SSSCs. For the purpose of this paper, five SSSCs are connected in series with the Marcy - Coopers Corner transmission line at regular intervals of 10 mH, starting with a SSSC connected at the Marcy bus. The control system for the five SSSCs are identical to each other, except that the sawtooth wave generators used in sine-

Table 6.4: SSSC parameters

SSSC Parameters	**Value**
Configuration	3 1-ϕ H-bridges
DC bus voltage	8 kV
DC bus capacitor	4700 μF
Switching Frequency	4 kHz
Transformer Parameters	**Value**
Configuration	3 1-ϕ transformers
Transformer rating	1 MVA
VSC side winding rating	4 kV
Line side winding rating	16 kV
Leakage reactance	0.10 p.u.

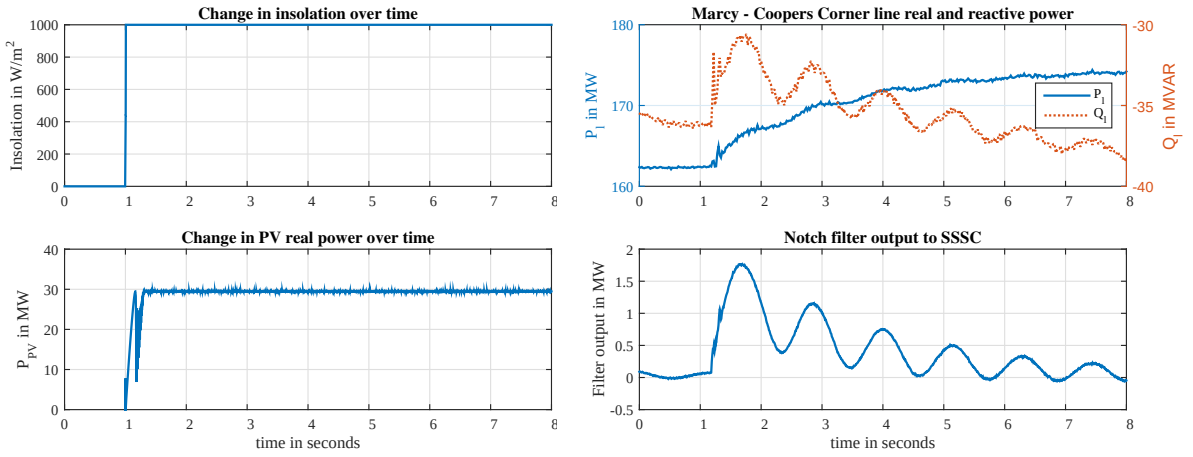

Figure 6.9: Performance of the Power Oscillation Damping controller on the Marcy - Coopers Corner transmission line during a PV power injection of 30 MW at t = 1 s.

triangle PWM are phase-shifted by 36° in adjacent SSSCs. The control system used for the SSSC is described in [88], and the design parameters of each SSSC unit is shown in table 6.4. In summary, $V^*_{SSSC_d}$ is obtained from the DC bus charging PI control loop, whereas $V^*_{SSSC_q}$ is obtained from the series voltage injection control loop. A synchronously-rotating reference frame aligned with the transmission line current I_1 is considered for the $abc - to - dq0$ and the $dq0 - to - abc$ transformations. The control block diagram for a single SSSC is shown in fig. 6.8. The SSSCs are set to control in the voltage-injection mode, and the voltage reference for the SSSCs is derived from the output of the notch filter, which is scaled using a constant K_{osc}. The entire system was simulated in PSCAD.

The SSSCs inject a voltage V_{1Sq} which is nearly in-phase (or out-of-phase) with the transmission line inductive voltage drop, and this controls the transmission line real power along a trajectory connecting the initial power flow and the final power flow with reduced oscillations. Fig. 6.9 shows the performance of the damping controller when the PV system starts injecting power at around t = 1 s. Due to this change, the power flow in the AC system is modified, and the system transitions from the initial power flow to its final value. In fig. 6.3, it can be seen that an uncompensated transmission line will experience under-damped oscillations as its

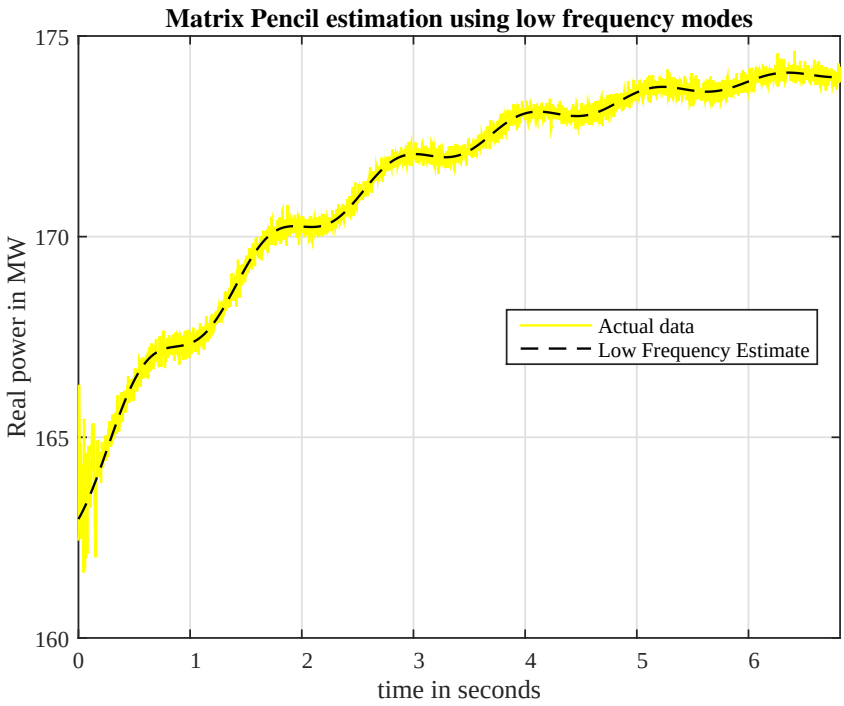

Figure 6.10: Comparison of the damped power signal with the Matrix Pencil estimate using $f_{damped} = 0.8769$ Hz and exponential modes

power flow transitions to its new steady state value. However from fig. 6.9b, it can be seen that the designed POM controller significantly damped the trajectory of the line power flow towards its new steady state.

Fig. 6.9b also shows the control signal generated by the damping controller as an input to each SSSC. The signal commands the SSSCs to inject a variable voltage V_{1Sq}, which alters the effective line voltage drop to obtain the damped trajectory for line power flow. In doing so, the SSSCs exchange a variable amount of reactive power with the transmission line, and this is reflected in the transmission line reactive power Q_l as measured at the Marcy bus.

Finally, the resultant Marcy - Coopers Corner transmission line power flow from fig. 6.9 was analyzed using the Matrix Pencil method for its modal content. The results of this analysis can be seen in table 6.5 and fig. 6.10, and it can be concluded that $f_{damped} = 0.8769$ Hz is the same dominant oscillatory mode from the previous modal analysis performed in section IV. The

Table 6.5: Modal content of the damped power flow

Frequency (Hz)	Damping coefficient (s^{-1})	Residue (MW)	Phase (rad)
0	0.4593	10.9876	-3.1416
0	0.0000578	174.6294	0
2.5648	19.6762	1.1713	-1.9239
0.8769	0.2691	0.3413	3.0468
7.9718	5.5908	0.1847	0.5467

addition of the POM controller caused a slight drift in the frequency and damping coefficient of the dominant mode. However, the addition of the POM controller substantially reduced the residue of the dominant mode. The reduction in residue implies a net reduction in the energy content of the oscillatory mode, and thus the POM controller achieved its design objective.

6.3.5 Conclusion and Future Work

In this section, the problem of power oscillations in AC transmission systems was discussed, and the impact large-scale penetration of renewable energy has on worsening this issue is shown with the NYPA 3-bus AC system. In order to damp the power oscillations, the modal content in the line power is estimated using Matrix Pencil method, and is used to design a POM controller using distributed SSSCs. After analysis of the results, it is concluded that the POM controller was effective in damping the oscillations by reducing the residue of the primary oscillatory mode. Future work can be directed towards real-time implementation of the controller, and using adaptive control techniques to make the control more robust to system changes.

6.4 POM with CHB-based SSSC

In this section, a POM controller will be developed using the CHB-based SSSC for the IEEE 14 bus system.

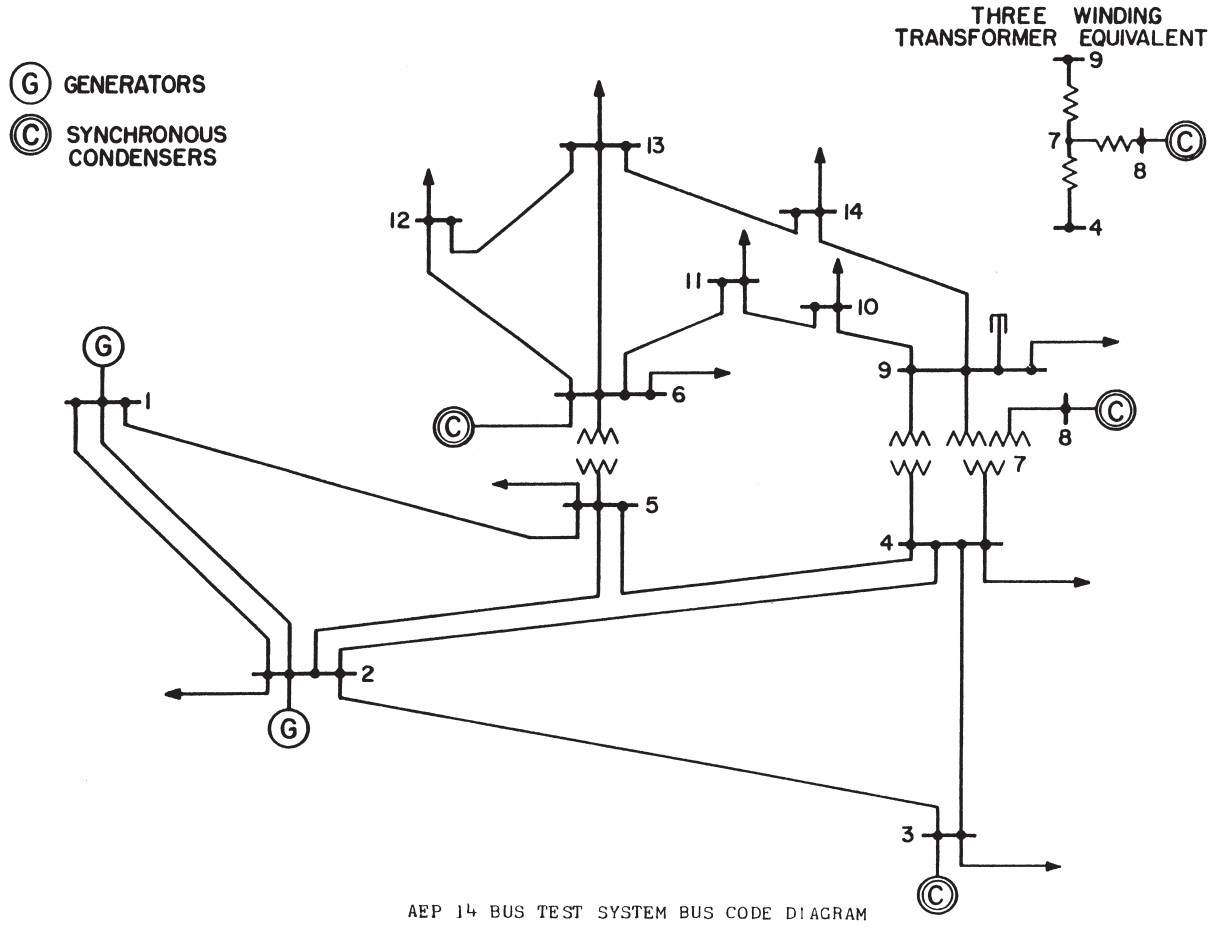

Figure 6.11: One-line diagram for the IEEE 14 bus system [1]

6.4.1 Equipment Description

The IEEE 14 bus test case was used for developing the POM controller using the CHB-based SSSC. The AC system has a base rating of 138 kV and 100 MVA. The one-line diagram of the IEEE 14 bus system can be seen in figure 6.11. The transmission line and initial power flow data can be found at the University of Washington Power System test-case archive [1] in the common data format.

The case was slightly modified to include a 60 MW photovoltaic plant connected at bus 3 and a CHB-based SSSC which was connected near bus 3 in series with the transmission line between bus 2 and bus 3, henceforth referred to as line 2-3. A 160 MVAR reactive load was

Table 6.6: Generator Parameters

Parameter	Unit	**G1**	**G2**	**SC3**	**SC6, SC8**
Apparent power	MVA	250	75	40	25
Rated line voltage	kV	18	13.8	13.8	13.8
X''_d	p.u.	0.155	0.13	0.231	0.2035
X'_d	p.u.	0.195	0.185	0.343	0.304
X_d	p.u.	0.995	1.05	2.373	1.769
X''_q	p.u.	0.143	0.13	0.13	0.199
X'_q	p.u.	n.a.	0.36	n.a.	0.5795
X_q	p.u.	0.568	0.98	1.172	0.855
X_p	p.u.	0.160	0.07	0.132	0.1045
T'_{d0}	s	9.2	6.1	11.6	8.0
T''_{d0}	s	0.039	0.038	0.058	0.0525
T'_{q0}	s	n.a.	0.3	n.a.	0.3
T''_{q0}	s	0.51	0.099	0.201	0.0151
R_a	p.u.	0.0014	0.0031	0.001	0.0025
Inertia Constant	s	6.412	6.1867	1.52	1.2
Damping	p.u.	0.01	0.01	0.01	0.01
Air Gap Factor	n.a.	0.96	1.0	1.0	1.0

added to offset the reactive power created by the filter capacitance connected at bus 3 to keep the harmonics generated by the SSSC and the PV plant in check. The voltage sources in the base case were replaced with synchronous machines. The parameters for the synchronous machines used are listed in table 6.6 and are taken from [85].

The photovoltaic plant is rated for 60 MW at peak insolation levels. The design of the PV plant is identical to the one given in table 6.2 and section 6.3.1, except for the 'number of module strings in parallel per array' which were doubled to 2000 in order to double the PV plant output. The PV-to-grid interface transformer rating was also changed to 17.32 kV / 138 kV, 60 MVA with the leakage reactance of the transformer is set to 0.15 $p.u. \equiv 0.1262\ H$. An L-C-L filter was designed on the grid side with the transformer leakage reactance being considered as L_2. Grid-side inductance L_1 was selected as $0.5 \times L_2 = 0.063145\ H$ while the shunt filter capacitance was set to 26.7432 μF, giving a filter resonant frequency of 150 Hz.

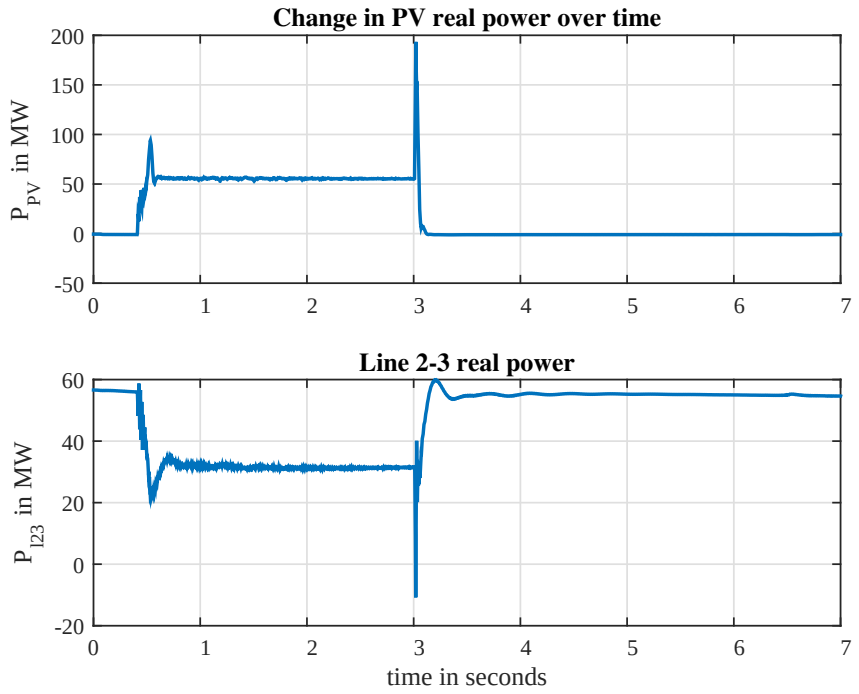

Figure 6.12: Effect of losing 60 MW PV plant output at bus 3 on line 2-3 real power

6.4.2 Power Oscillations and Modal Analysis

In this case, it was assumed that the PV plant was already operating for some time at full power output of 60 MW. This had the effect of reducing the line power flow from bus 2 to bus 3 to about 30 MW from 60 MW. At t = x seconds, the power output of the PV plant reduces to zero due a loss of insolation, or a fault. Figure 6.12 shows the transmission line power curve during and after the loss of PV plant output. It can be seen that the event triggers some oscillations within the transmission line, however it is observed that the oscillatory modes are heavily damped naturally by the AC system. This can be attributed to several factors like load, line resistance, voltage levels, etc. However, there is a little scope for improvement if the first real power swing can be reduced or eliminated.

In order to do so, a Matrix Pencil estimate of the real power curve was calculated, and the results for the same can be seen in table 6.7. The table lists five dominant modes, one of which is a real exponential mode that serves the purpose of establishing the DC bias for the reference

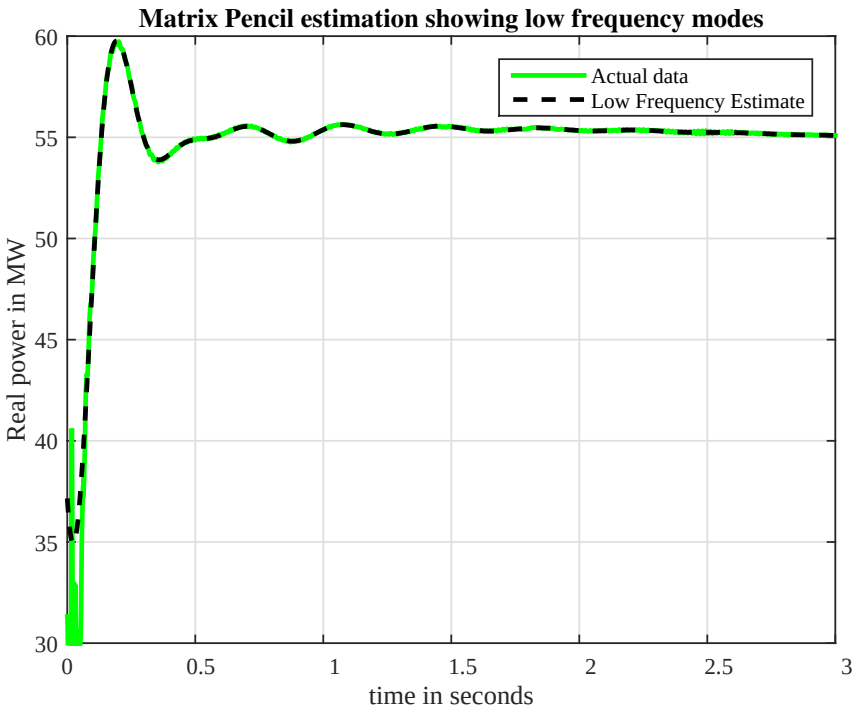

Figure 6.13: Comparison of the actual signal with the Matrix Pencil estimate

power signal. The other four modes are complex, and thus result in oscillations within the network. The number of relevant modes seen for the IEEE 14 bus system is higher than the previous NYPA system as it has five synchronous generators which swing non-coherently with respect to each other. Figure 6.13 compares the actual real power curve with the low frequency estimate obtained using the Matrix Pencil method. Since the signal is already highly damped, it makes sense to select the primary frequency based on the residues in this case. From table

Table 6.7: Modal content of line 2-3's real power flow

Frequency (Hz)	Damping coefficient (s^{-1})	Residue (MW)	Phase (rad)
0	0.0069	56.2493	0
0.0838	2.0253	3.2407	1.7877
1.3196	6.4477	1.4518	2.5268
2.5754	1.8935	1.1596	1.4451
3.1474	6.6912	10.2977	2.4317

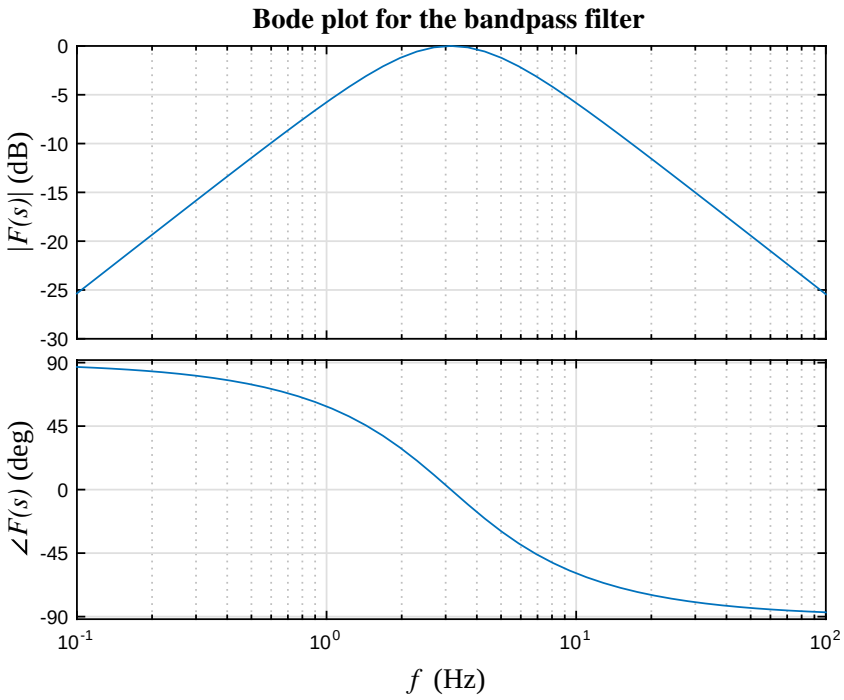

Figure 6.14: Bode plot of the band-pass filter as shown in Eq. (6.21)

6.7, it is clear that $f_{osc} = 3.1474$ Hz is the dominant mode in the transmission line power. The mode at 0.0838 Hz is also significant but it is ignored in the controller design as the mode f_{osc} contributes more to the peak seen in figure 6.13.

Based on this data, a second order band-pass filter is designed centered around $f_{osc} = 3.1474$ Hz with a damping coefficient of 0.85. The resulting transfer function for the filter is

$$F(s) = \frac{33.6187s}{s^2 + 33.6187s + 391.0782} \tag{6.21}$$

Figure 6.14 shows the bode of the band-pass filter given in Eq. (6.21). The output of the filter is given as a q-axis voltage command V^*_{1Sq} to the CHB-based SSSC.

If we take a look at the dominant mode which is being damped, it is actually a complex mode with $\sigma = -6.6912\ s^{-1}$ and $\omega = 2\pi \times f_{osc} = 19.7757$ rad/s. However, if we compare this mode with the denominator polynomial of a standard second-order oscillator as $G(s) = s^2 + 2\zeta\omega_n s + \omega_n^2$,

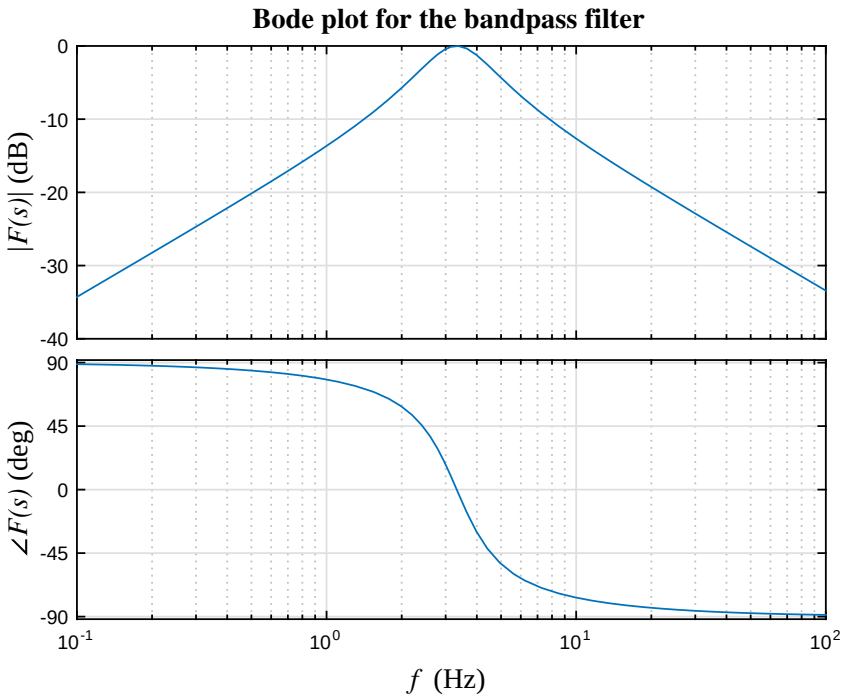

Figure 6.15: Bode plot of the alternate band-pass filter as shown in Eq. (6.22)

the roots of $G(s)$ can be correlated with $\sigma + j\omega$ to obtain ω_n and ζ. Doing so yields the values for $\omega_n = 20.8767$ and $\zeta = 0.3205$, which can be used to create a new band-pass filter with the transfer function of

$$F_2(s) = \frac{13.3824s}{s^2 + 13.3824s + 435.8366} \tag{6.22}$$

The bode plot for Eq. (6.22) is shown in figure 6.15.

6.4.3 Implementation and Results

As mentioned in the previous section, a CHB-based SSSC was connected on the transmission line between buses 2 and 3 on the IEEE 14 bus network. The IEEE 14 bus base case was obtained from the PSCAD repository [89]. The CHB-based SSSC is identical to the one designed in section 5.3.3 and was also implemented in PSCAD. The results of the PSCAD simulation can

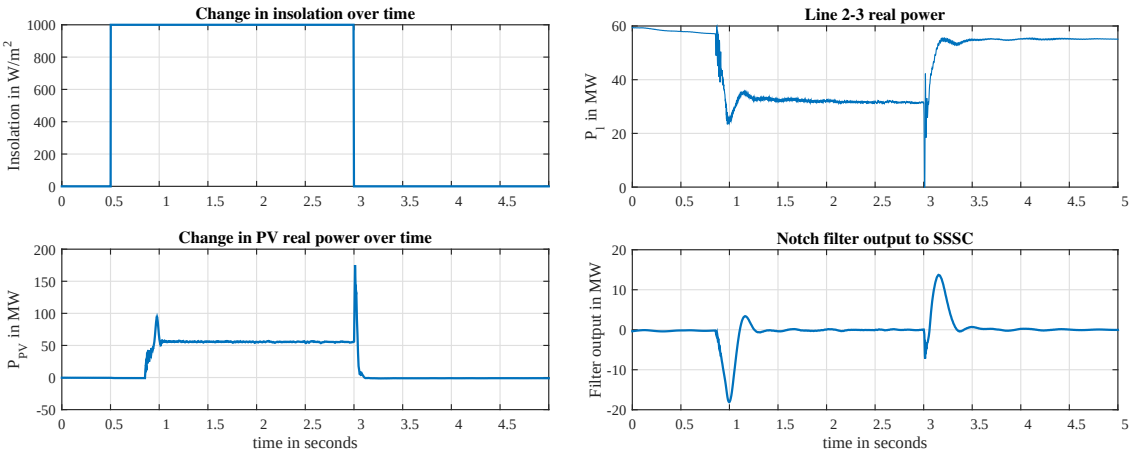

(a) (b)

Figure 6.16: Performance of the POM controller on the transmission line 2-3

be seen in fig. 6.16. At $t = 1$ s, the PV plant starts generating 60 MW which induces oscillations on the line 2-3, while the POM controller is turned off. The POM controller is later turned on at $t = 2$ s. At $t = 3$ s, the PV plant loses its power output due to a drop in insolation. However, the POM controller ensures that the first swing of the oscillation is severely damped as can be seen by comparing figure 6.12 and figure 6.16b.

The performance of the alternate filter is somewhat similar, and the best way to compare its performance with the original filter is to overlay their performance curves on top of each other. Figure 6.17 shows the band-pass filter output and the compensated transmission line real power for the two POM controllers. The test conditions for the two were identical with the PV plant losing its real power output at $t = 0$ seconds. This causes the transmission line power to bounce back to a steady-state value of around 55 MW.

From figure 6.17a, it is clear that the response of the alternate controller is slightly under-damped as compared to the original, which is expected as it has a lower damping coefficient. From figure 6.17b, we can conclude that the alternate controller has a slightly larger overshoot, but it has a shorter settling time as compared to the original controller. Also, it seems that the original controller seems to excite a higher frequency mode within the system, which is

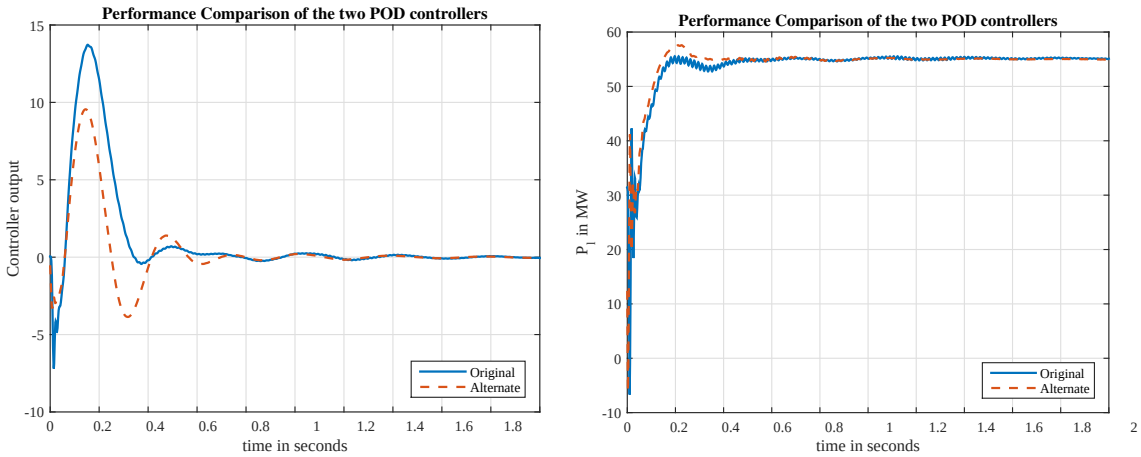

(a) (b)

Figure 6.17: Performance comparison of the two POM controllers on line 2-3

eventually damped, but it could lead to instabilities in other situations. This behavior was found to be absent in the alternate controller as it trades overshoot for a better rejection of frequencies outside the band.

6.4.4 Conclusion

In this section, the performance of the CHB-based SSSC in damping power system oscillations was demonstrated using a POM controller designed using the Matrix Pencil method. The IEEE 14 bus system was used as a base case for the experiment, and it was observed that the 14 bus system inherently has good damping. However, the POM controller was still able to slightly improve the network performance by reducing the overshoot on line 2-3's real power signal. An alternate controller which utilizes data from the Matrix Pencil estimation to calculate the damping coefficient was also developed. Its performance was compared with the original controller and it was noted that though it has a higher overshoot, it had a lower settling time and better rejection of frequencies outside the pass-band.

6.5 Conclusion

In this chapter, the performance of power oscillation damping controllers in reducing power oscillations on transmission lines was demonstrated using SSSCs based on two different topologies: the distributed FACTS devices and the CHB-based SSSC, within NYPA's 3-bus AC system and the IEEE 14 bus system respectively. Power Oscillations are a wide-spread phenomenon on transmission networks and would definitely become more prevalent with the increasing penetration of renewable energy resources in modern power networks. An extreme example of this would be the effect of a total solar eclipse that could cause widespread dips in solar power output temporarily. POM controllers can help the grid transition in and out of such contingencies in a controlled manner.

Chapter 7

Conclusion

This report focused on highlighting some of the problems caused by large-scale penetration of renewable energy resources, and then suggested some applications of FACTS devices like the SSSC in eliminating power system oscillations which is one of the system issues that arise due to high renewable energy penetration.

Chapter 1 provided an introduction to the problems caused by large-scale penetration renewables and includes a brief motivation for research in this area. Chapter 2 described the effect of large scale penetration of renewable energy resources on high voltage transmission systems. It begins with a brief description about conventional energy sources, and contrasts it with the non-deterministic nature of renewable energy resources. Detailed wind and PV system models are given, and the control structures required to interface them to the grid are described in detail.

Chapter 3 discussed the various FACTS devices along with their control strategies. A brief description of phase shifting transformers (PST) is given, which is a competing technology to FACTS devices. SSSC, STATCOM and the UPFC are discussed in detail along with their major control algorithms for achieving various control objectives. Two major types of control are discussed: Angle control, and Vector control.

In Chapter 4, a reduced-order equivalent model of the Western Electricity Coordinating

Council's (WECC) 500 kV system was developed using Phasor Measurement Unit (PMU) data. Various estimation techniques like the Prony method, nonlinear least squares, etc were used to determine the key parameters of the five-machine system like line impedance, thevenin reactance, machine inertia and damping. This model was then used as a base-case onto which the effect of large-scale penetration of renewable energy resources was evaluated and appropriate control actions can be performed. Tests involving loss of inertia, loss of transmission lines, and large scale wind penetration are performed and their effects on power system stability are observed.

Chapter 5 focused on a series-connected FACTS device known as the Static Series Synchronous Compensators (SSSC). The first section discusses the application of SSSCs in mitigating Ferranti effect. In this case, a single SSSC was assumed to be connected near the sending end of a 250 km long open-ended 230 kV transmission line. Ferranti effect caused the receiving end of the transmission line to experience an overvoltage during no-load conditions. The SSSC controls were slightly modified to estimate the overvoltage at the receiving end and correct for it at the sending end, which resulted in the mitigation of Ferranti effect. The next section describes a control algorithm for SSSC based on a Cascaded H-Bridge Converter. In this section, a new control algorithm for the CHB-based SSSC was proposed which included Capacitor Voltage Balancing loops which would control the DC bus voltage close to the average DC bus value. The final section described a centralized control scheme for distributed series-connected FACTS devices which includes DC capacitor voltage balancing capabilities. The new centralized control algorithm allowed the distributed SSSCs to be controlled with the same performance as that of a distributed controller, while maintaining the DC bus voltages of the individual phases close to each other.

Chapter 6 focuses on the mitigation of power system oscillations in transmission networks. The first section discusses the Matrix Pencil algorithm that is used for estimating the oscillatory modes within the raw data. The next section uses this method to develop a power oscillation mitigation (POM) controller for distributed SSSCs connected in NYPA's three-bus AC system.

The Matrix Pencil method estimated the frequencies present in the transmission line power signal, and the dominant frequency in the signal was used to design a second-order band-pass filter which forms the basis of the POM controller, with the damping coefficient ζ being optimized for the lowest settling time. The performance of the controller was observed and it was concluded that the controller reduced the residue of the dominant mode. The final section discusses the design of another POM controller for a CHB-based SSSC connected in the IEEE-14 bus system. It was noted that the IEEE 14 bus system naturally had a lot of damping, and the effectiveness of the POM controller would be limited. However, it was observed that the POM controller was able to reduce the overshoot of the real power on the transmission line. Further, a second POM controller which takes the damping coefficient of the dominant mode into account, and its performance was compared with the first controller.

REFERENCES

[1] "IEEE 14 Bus Power Flow Test Case." University of Washington - Power Systems Text Case Archive. `https://www2.ee.washington.edu/research/pstca/pf14/pg_tca14bus.htm`.

[2] N. G. Hingorani and L. Gyugyi, *Understanding FACTS : Concepts and technology of flexible AC transmission systems*. IEEE Press, 1999.

[3] U. S. EIA, "Annual Energy Outlook 2015 with projections to 2040," tech. rep., U.S. Energy Information Administration, Washington, 2015.

[4] R. M. Mathur and R. K. Varma, *Thyristor-based FACTS Controllers for Electrical Transmission Systems*. Wiley-IEEE Press, 2002.

[5] J. H. Chow, *Power System Coherency and Model Reduction*. Springer Press, 2013.

[6] L. Roberts, G. Kafanas, A. Champneys, M. di Bernardo, and K. Bell, "A parametric investigation on the effects of inertia on the stability of power systems," in *PowerTech, 2015 IEEE Eindhoven*, pp. 1–6, IEEE, 2015.

[7] A. Ulbig, T. S. Borsche, and G. Andersson, "Impact of Low Rotational Inertia on Power System Stability and Operation," in *IFAC World Congress*, vol. 19, pp. 7290–7297, 2014.

[8] R. H. Park, "Definition of an ideal synchronous machine and formula for the armature flux linkages," *General Electric Review*, vol. 31, no. 6, pp. 332–334, 1928.

[9] W. V. Lyon, *Transient Analysis of Alternating-current Machinery: An Application of Method of Symmetrical Components*. Technology Press of Massachusetts Institute of Technology, and Wiley, New York, 1954.

[10] C. Schauder and H. Mehta, "Vector analysis and control of advanced static VAr compensators," *IEE Proceedings-C (Generation, Transmission and Distribution)*, vol. 140, no. 4, pp. 299–306, 1993.

[11] R. A. Rohde, "Solar radiation spectrum." http://www.globalwarmingart.com/wiki/File:Solar_Spectrum_png, 2007. [Online; accessed 24-November-2015].

[12] G. Kopp and J. L. Lean, "A new, lower value of total solar irradiance: Evidence and climate significance," *Geophysical Research Letters*, vol. 38, no. 1, 2011.

[13] NREL, "National Solar Radiation Database, 1991 - 2010 Update." http://rredc.nrel.gov/solar/old_data/nsrdb/1991-2010/hourly/siteonthefly.cgi?id=723060, 2010. [Online; accessed 24-November-2015].

[14] R. L. Cummerow, "Photovoltaic Effect in p - n Junctions," *Physical Review*, vol. 95, no. 1, p. 16, 1954.

[15] G. Abad, J. Lopez, M. Rodríguez, L. Marroyo, and G. Iwanski, *Doubly fed induction machine: modeling and control for wind energy generation*. John Wiley & Sons, 2011.

[16] R. Pena, J. C. Clare, and G. M. Asher, "Doubly fed induction generator using back-to-back PWM converters and its application to variable-speed wind-energy generation," *IEE Proceedings-Electric Power Applications*, vol. 143, no. 3, pp. 231–241, 1996.

[17] B. Hopfensperger, D. J. Atkinson, and R. A. Lakin, "Stator-flux-oriented control of a doubly-fed induction machine with and without position encoder," *IEE Proceedings - Electric Power Applications*, vol. 147, no. 4, pp. 241–250, 2000.

[18] P. C. Krause, O. Wasynczuk, S. D. Sudhoff, and S. Pekarek, *Analysis of electric machinery and drive systems*. Wiley-IEEE Press, 2002.

[19] M. Chinchilla, S. Arnaltes, and J. C. Burgos, "Control of permanent-magnet generators applied to variable-speed wind-energy systems connected to the grid," *Energy Conversion, IEEE Transactions on*, vol. 21, no. 1, pp. 130–135, 2006.

[20] A. D. Hansen and G. Michalke, "Multi-pole permanent magnet synchronous generator wind turbines' grid support capability in uninterrupted operation during grid faults," *IET Renewable Power Generation*, vol. 3, no. 3, pp. 333–348, 2009.

[21] B. Wu, Y. Lang, N. Zargari, and S. Kouro, *Power conversion and control of wind energy systems*. John Wiley & Sons, 2011.

[22] K. K. Sen and M. L. Sen, "Appendix b: Power flow control equations in a lossy transmission line," in *Introduction to Facts Controllers: Theory, Modeling, and Applications*, pp. 413–449, Wiley-IEEE Press, 2009.

[23] L. Gyugyi, C. D. Schauder, and K. K. Sen, "Static synchronous series compensator: a solid-state approach to the series compensation of transmission lines," *IEEE Transactions on Power Delivery*, vol. 12, no. 1, pp. 406–417, 1997.

[24] K. K. Sen, "SSSC - static synchronous series compensator: theory, modeling, and application," *IEEE Transactions on Power Delivery*, vol. 13, no. 1, pp. 241–246, 1998.

[25] K. K. Sen and A. J. F. Keri, "Comparison of field results and digital simulation results of voltage-sourced converter-based FACTS controllers," *IEEE Transactions on Power Delivery*, vol. 18, no. 1, pp. 300–306, 2003.

[26] M. Bongiorno, J. Svensson, and L. Angquist, "On Control of Static Synchronous Series Compensator for SSR Mitigation," *IEEE Transactions on Power Electronics*, vol. 23, no. 2, pp. 735–743, 2008.

[27] M. Bongiorno, L. Angquist, and J. Svensson, "A Novel Control Strategy for Subsynchronous Resonance Mitigation Using SSSC," *IEEE Transactions on Power Delivery*, vol. 23, no. 2, pp. 1033–1041, 2008.

[28] D. Rai, S. O. Faried, G. Ramakrishna, and A. Edris, "Damping Inter-Area Oscillations Using Phase Imbalanced Series Compensation Schemes," *IEEE Transactions on Power Systems*, vol. 26, no. 3, pp. 1753–1761, 2011.

[29] L. Wang and Q.-S. Vo, "Power Flow Control and Stability Improvement of Connecting an Offshore Wind Farm to a One-Machine Infinite-Bus System Using a Static Synchronous Series Compensator," *IEEE Transactions on Sustainable Energy*, vol. 4, no. 2, pp. 358–369, 2013.

[30] A. C. Pradhan and P. W. Lehn, "Frequency-domain analysis of the static synchronous series compensator," *IEEE Transactions on Power Delivery*, vol. 21, no. 1, pp. 440–449, 2006.

[31] L. Gyugyi, "Unified power-flow control concept for flexible AC transmission systems," *IEE Proceedings-C (Generation, Transmission and Distribution)*, vol. 139, no. 4, pp. 323–331, 1992.

[32] L. Gyugyi, C. D. Schauder, S. L. Williams, T. R. Rietman, D. R. Torgerson, and A. Edris, "The unified power flow controller: a new approach to power transmission control," *IEEE Transactions on Power Delivery*, vol. 10, no. 2, pp. 1085–1097, 1995.

[33] C. D. Schauder, L. Gyugyi, M. R. Lund, D. M. Hamai, T. R. Rietman, D. R. Torgerson, and A. Edris, "Operation of the Unified Power Flow Controller (UPFC) under practical constraints," *IEEE Transactions on Power Delivery*, vol. 13, no. 2, pp. 630–639, 1998.

[34] I. Papic, P. Zunko, D. Povh, and M. Weinhold, "Basic control of unified power flow controller," *IEEE Transactions on Power Systems*, vol. 12, no. 4, pp. 1734–1739, 1997.

[35] H. Fujita, Y. Watanabe, and H. Akagi, "Control and analysis of a unified power flow controller," *IEEE Transactions on Power Electronics*, vol. 14, no. 6, pp. 1021–1027, 1999.

[36] S. Babaei, G. Chavan, and S. Bhattacharya, "Control structures for the unified power flow controller," in *IECON 2014 - 40th Annual Conference of the IEEE Industrial Electronics Society*, pp. 4224–4230, 2014.

[37] A. Yazdani and R. Iravani, "A unified dynamic model and control for the voltage-sourced converter under unbalanced grid conditions," *IEEE Transactions on Power Delivery*, vol. 21, no. 3, pp. 1620–1629, 2006.

[38] J. Giri, M. Parashar, J. Trehern, and V. Madani, "The situation room: Control center analytics for enhanced situational awareness," *Power and Energy Magazine, IEEE*, vol. 10, no. 5, pp. 24–39, 2012.

[39] J. H. Chow, *Time-scale modeling of dynamic networks with applications to power systems*. Springer Berlin Heidelberg, 1982.

[40] K. M. Rogers, R. D. Spadoni, and T. J. Overbye, "Identification of power system topology from synchrophasor data," in *2011 IEEE PES Power Systems Conference and Exposition (PSCE)*, pp. 1–8, IEEE, 2011.

[41] J. Ballance, B. Bhargava, and G. D. Rodriguez, "Use of synchronized phasor measurement system for enhancing ac-dc power system transmission reliability and capability," in *Eastern Interconnection Phasor Project (EIPP) Meeting*, 2004.

[42] D. J. Trudnowski, "Estimating electromechanical mode shape from synchrophasor measurements," *IEEE Transactions on Power Systems*, vol. 3, no. 23, pp. 1188–1195, 2008.

[43] G. Liu, J. Ning, Z. Tashman, V. M. Venkatasubramanian, and P. Trachian, "Oscillation monitoring system using synchrophasors," in *2012 IEEE Power and Energy Society General Meeting*, pp. 1–8, IEEE, 2012.

[44] P. W. Sauer and M. A. Pai, *Power system dynamics and stability*. Prentice Hall, 1998.

[45] A. Chakrabortty, J. H. Chow, and A. Salazar, "A measurement-based framework for dynamic equivalencing of large power systems using wide-area phasor measurements," *IEEE Transactions on Smart Grid*, vol. 2, no. 1, pp. 68–81, 2011.

[46] L. Ljung, *System identification*. Springer, 1998.

[47] A. Björck, *Numerical methods for least squares problems*. Siam, 1996.

[48] D. Sullivan, J. Paserba, T. Croasdaile, R. Pape, M. Takeda, S. Yasuda, H. Teramoto, Y. Kono, K. Temma, A. Johnson, , R. Tucker, and T. Tran, "Dynamic voltage support with the rector SVC in California's San Joaquin Valley," in *IEEE/PES Transmission and Distribution Conference and Exposition*, pp. 1–6, 2008.

[49] N. Zhou, J. W. Pierre, and J. F. Hauer, "Initial results in power system identification from injected probing signals using a subspace method," *IEEE Transactions on Power Systems*, vol. 21, pp. 1296–1302, Aug 2006.

[50] W. D. Stevenson Jr., *Elements of power system analysis*. McGraw-Hill New York, 4 ed., 1982.

[51] I. Oumarou, D. Jiang, and C. Yijia, "Optimal Placement of shunt connected Facts device in a series compensated long transmission line," in *Proceedings of the World Congress on Engineering*, vol. 1, 2009.

[52] K. Vechalapu, S. Bhattacharya, E. Van Brunt, S.-H. Ryu, D. Grider, and J. W. Palmour, "Comparative Evaluation of 15-kV SiC MOSFET and 15-kV SiC IGBT for Medium-Voltage Converter Under the Same dv/dt Conditions," *IEEE Journal of Emerging and Selected Topics in Power Electronics*, vol. 5, no. 1, pp. 469–489, 2017.

[53] D. G. Holmes and T. A. Lipo, *Pulse Width Modulation for Power Converters: Principles and Practice*, ch. Modulation of Three-Phase Voltage Source Inverters, pp. 215–258. Wiley-IEEE Press, 2003.

[54] L. Kovalsky, C. Schauder, E. Stacy, M. Weaver, S. MacDonald, *et al.*, "Convertible static compensator (CSC) for New York Power Authority," *EPRI, Palo Alto, CA, Tech. Rep*, vol. 1001809, December 2003. `https://www.epri.com/#/pages/product/1001809/`.

[55] X. Zhou, Z. Xu, A. Q. Huang, and D. Boroyevich, "Comparison of high power IGBT, IGCT and ETO for pulse applications," in *Annual Power Electronics Seminar*, vol. 2, pp. 506–510, 2002.

[56] "StakPak: IGBT press-pack modules." ABB Web Flyer, April 2015. Doc. no. 5SYA 2100-03.

[57] S. Babaei, G. Chavan, and S. Bhattacharya, "Unified power flow controller operational limit improvement," in *Industrial Electronics Society, IECON 2014-40th Annual Conference of the IEEE*, pp. 4416–4422, IEEE, 2014.

[58] M. Glinka and R. Marquardt, "A new AC/AC multilevel converter family," *IEEE Transactions on Industrial Electronics*, vol. 52, no. 3, pp. 662–669, 2005.

[59] H. Akagi, "Classification, Terminology, and Application of the Modular Multilevel Cascade Converter (MMCC)," *IEEE Transactions on Power Electronics*, vol. 26, no. 11, pp. 3119–3130, 2011.

[60] M. Hagiwara, R. Maeda, and H. Akagi, "Negative-Sequence Reactive-Power Control by a PWM STATCOM Based on a Modular Multilevel Cascade Converter (MMCC-SDBC)," *IEEE Transactions on Industry Applications*, vol. 48, no. 2, pp. 720–729, 2012.

[61] C.-T. Lee, B.-S. Wang, S.-W. Chen, S.-F. Chou, J.-L. Huang, P.-T. Cheng, H. Akagi, and P. Barbosa, "Average Power Balancing Control of a STATCOM Based on the Cascaded H-Bridge PWM Converter With Star Configuration," *IEEE Transactions on Industry Applications*, vol. 50, no. 6, pp. 3893–3901, 2014.

[62] H. Akagi, S. Inoue, and T. Yoshii, "Control and Performance of a Transformerless Cascade PWM STATCOM With Star Configuration," *Industry Applications, IEEE Transactions on*, vol. 43, no. 4, pp. 1041–1049, 2007.

[63] L. Harnefors, A. Antonopoulos, S. Norrga, L. Angquist, and H.-P. Nee, "Dynamic analysis of modular multilevel converters," *IEEE Transactions on Industrial Electronics*, vol. 60, no. 7, pp. 2526–2537, 2013.

[64] G. Chavan and S. Bhattacharya, "A novel control algorithm for a static series synchronous compensator using a Cascaded H-bridge converter," in *Industry Applications Society Annual Meeting, 2016 IEEE*, pp. 1–6, IEEE, 2016.

[65] B. Wu, "Cascaded H-Bridge Multilevel Inverters," in *High-Power Converters and AC Drives*, pp. 119–142, Wiley-IEEE Press, 2006.

[66] H. C. Chen, P. H. Wu, C. T. Lee, C. W. Wang, C. H. Yang, and P. T. Cheng, "Zero-Sequence Voltage Injection for DC Capacitor Voltage Balancing Control of the Star-Connected Cascaded H-Bridge PWM Converter Under Unbalanced Grid," *IEEE Transactions on Industry Applications*, vol. 51, no. 6, pp. 4584–4594, 2015.

[67] R. Xu, Y. Yu, R. Yang, G. Wang, D. Xu, B. Li, and S. Sui, "A Novel Control Method for Transformerless H-Bridge Cascaded STATCOM With Star Configuration," *IEEE Transactions on Power Electronics*, vol. 30, no. 3, pp. 1189–1202, 2015.

[68] H. Iman-Eini, J. L. Schanen, S. Farhangi, and J. Roudet, "A Modular Strategy for Control and Voltage Balancing of Cascaded H-Bridge Rectifiers," *IEEE Transactions on Power Electronics*, vol. 23, no. 5, pp. 2428–2442, 2008.

[69] "IEEE Recommended Practice and Requirements for Harmonic Control in Electric Power Systems," *IEEE Std 519-2014 (Revision of IEEE Std 519-1992)*, pp. 1–29, 2014.

[70] X. Xiao, B. Gao, and C. Zhao, "A novel SSR-damping scheme based on a single-phase SSSC," in *Power Electronics, Drives and Energy Systems (PEDES) & 2010 Power India, 2010 Joint International Conference on*, pp. 1–5, IEEE, 2010.

[71] M. Bongiorno, J. Svensson, and L. Angquist, "Single-phase VSC based SSSC for subsynchronous resonance damping," *IEEE Transactions on Power Delivery*, vol. 23, no. 3, pp. 1544–1552, 2008.

[72] G. Chavan, M. Weiss, A. Chakrabortty, S. Bhattacharya, A. Salazar, and F. Habibi-Ashrafi, "Identification and Predictive Analysis of a Multi-Area WECC Power System Model Using Synchrophasors," *IEEE Transactions on Smart Grid*, vol. PP, no. 99, pp. 1–1, 2016.

[73] A. Jain, E. Biyik, and A. Chakrabortty, "A model predictive control design for selective modal damping in power systems," in *2015 American Control Conference (ACC)*, pp. 4314–4319, 2015.

[74] L. Angquist, B. Lundin, and J. Samuelsson, "Power oscillation damping using controlled reactive power compensation-a comparison between series and shunt approaches," *IEEE Transactions on Power Systems*, vol. 8, no. 2, pp. 687–700, 1993.

[75] A. Chakrabortty, "Wide-Area Damping Control of Power Systems Using Dynamic Clustering and TCSC-Based Redesigns," *IEEE Transactions on Smart Grid*, vol. 3, no. 3, pp. 1503–1514, 2012.

[76] M. Weiss, A. Chakrabortty, F. H. Ashrafi, A. Jamehbozorg, and B. N. Abu-Jaradeh, "A wide-area SVC controller design using a dynamic equivalent model of WECC," in *2015 IEEE Power Energy Society General Meeting*, pp. 1–5, 2015.

[77] M. Beza and M. Bongiorno, "An Adaptive Power Oscillation Damping Controller by STATCOM With Energy Storage," *IEEE Transactions on Power Systems*, vol. 30, no. 1, pp. 484–493, 2015.

[78] S. Chandra, D. F. Gayme, and A. Chakrabortty, "Coordinating Wind Farms and Battery Management Systems for Inter-Area Oscillation Damping: A Frequency-Domain Approach," *IEEE Transactions on Power Systems*, vol. 29, no. 3, pp. 1454–1462, 2014.

[79] B. S. Rigby, N. S. Chonco, and R. G. Harley, "Analysis of a power oscillation damping scheme using a voltage-source inverter," *IEEE Transactions on Industry Applications*, vol. 38, no. 4, pp. 1105–1113, 2002.

[80] L. Zeni, R. Eriksson, S. Goumalatsos, M. Altin, P. Srensen, A. Hansen, P. Kjr, and B. Hesselbk, "Power Oscillation Damping From VSC-HVDC Connected Offshore Wind Power Plants," *IEEE Transactions on Power Delivery*, vol. 31, no. 2, pp. 829–838, 2016.

[81] P. M. Anderson and A. A. Fouad, *The Elementary Mathematical Model*, pp. 13–52. Wiley-IEEE Press, 2003.

[82] N. G. Hingorani and L. Gyugyi, *Static Series Compensators: GCSC, TSSC, TCSC and SSSC*, pp. 209–265. Wiley-IEEE Press, 2000.

[83] T. K. Sarkar and O. Pereira, "Using the matrix pencil method to estimate the parameters of a sum of complex exponentials," *IEEE Antennas and Propagation Magazine*, vol. 37, no. 1, pp. 48–55, 1995.

[84] S. Babaei, B. Parkhideh, B. Fardanesh, and S. Bhattacharya, "Convertible Static Compensator (CSC) performance under system fault," in *2012 IEEE Power and Energy Society General Meeting*, pp. 1–8, July 2012.

[85] P. M. Anderson and A. A. Fouad, *Power System Control and Stability*, ch. Appendix D: Typical System Data, pp. 555–581. Wiley-IEEE Press, 2003.

[86] A. Safari and S. Mekhilef, "Simulation and Hardware Implementation of Incremental Conductance MPPT With Direct Control Method Using Cuk Converter," *IEEE Transactions on Industrial Electronics*, vol. 58, no. 4, pp. 1154–1161, 2011.

[87] S. Acharya, S. Bhattacharya, and N. Yousefpoor, "Dynamic performance evaluation of hybrid multi-terminal HVAC/HVDC grid," in *2015 IEEE Energy Conversion Congress and Exposition (ECCE)*, pp. 2287–2293, 2015.

[88] G. Chavan, S. Acharya, S. Bhattacharya, D. Das, and H. Inam, "Application of static synchronous series compensators in mitigating Ferranti effect," in *2016 IEEE Power and Energy Society General Meeting (PESGM)*, pp. 1–5, 2016.

[89] "IEEE 14 bus test system." PSCAD - Knowledge Base. `https://hvdc.ca/knowledge-base/read,article/26/ieee-14-bus-system/v:`.